Characterization of Neutron Fields around an Intense Neutron Generator

By Leslie Kicka

A Thesis Submitted in Partial Fulfillment

Of the Requirements for the Degree of

Master of Applied Science

In

Nuclear Engineering

Faculty of Energy Systems and Nuclear Science

University of Ontario Institute of Technology

December 2016

Abstract

Neutron fields in the vicinity of the University of Ontario Institute of Technology neutron facility have been investigated in a series of simulations and experiments. The neutron fluence at several locations around the neutron generator facility has been simulated using MCNPX 2.7E Monte Carlo particle transport program. The P-385 neutron generator is configured to function with a deuterium-deuterium fusion reaction using accelerated charged deuterons colliding with a metal deuteride target. This fusion reaction is characterized by an anisotropic angular and energy distribution in the centre-of-mass and laboratory frames of reference. Three neutron sources were modelled in the simulation with distributions corresponding to different incident deuteron energies of 130 keV, 110 keV, and 90 keV. An idealized isotropic source was likewise simulated for purposes of comparison and determination of the applicability of such an approximation.

Along with the performed simulations and to validate the calculation, a series of experiments have been carried out to determine the dose rate measurement at locations adjacent to the generator. The collected data were used to calculate the neutron intensity of the P-385 neutron generator. The measurements were taken using bubble detectors with different sensitivities. Also, the total dose rates corresponding to applied acceleration potentials were estimated at various locations, utilizing a thin target approximation.

Acknowledgements

I thank my mother and father for their endless support throughout my time as a graduate student.

I would like to express my appreciation to Dr. Orchard for operating the equipment necessary to acquire experimental data.

Finally, I owe a large debt of gratitude to my thesis supervisor, Dr. Machrafi, for providing invaluable guidance during the course of my work and research.

Table of Contents

List of Figures

List of Tables

Nomenclature

$E^l(X) = kinetic\ energy\ of\ particle\ X\ in\ LAB$

$E^{cm}(X) = kinetic\ energy\ particle\ X\ in\ CM$

$E^* = excitation\ energy\ in\ nucleus$

$h = Planck\ constant$

$I(X) = intensity\ of\ particle\ X$

$J(\pi) = particle\ spin\ (parity)$

$M(X) = atomic\ mass\ of\ particle\ X$

$p = particle\ momentum$

$Q = reaction\ energy\ value$

$u = 1\ amu = 1.66 \times 10^{-27}\ kg$

$\theta^l = polar\ angle\ in\ LAB$

$\theta^{cm} = polar\ angle\ in\ CM$

$\lambda_r = \frac{h}{2\pi p} = \frac{h}{2\pi m_n v} = reduced\ wavelength$

$\sigma_s = total\ scattering\ cross\ section$

$\sigma_{el} = elastic\ scattering\ cross\ section$

$\sigma_{in} = inelastic\ scattering\ cross\ section$

$\sigma_a = absorption\ cross\ section$

$\Phi(\mathrm{X}) = flux\ of\ particle\ X$

$SP = source\ particle$

$LAB = laboratory\ system\ reference\ frame$

$CM = centre - of - mass\ system\ reference\ frame$

Introduction

The neutron generation facility located in the basement of the Energy Research Centre at the University of Ontario Institute of Technology was designed to host different intense radiation sources. Currently the facility contains a Thermo-Scientific P-385 generator, which in its current configuration generates neutrons from a deuterium-deuterium fusion reaction with an average energy of ~2.5 MeV. The hosting laboratory in which the neutron generator is placed was specifically designed with a maze-like wall arrangement to decrease the possible dose at the entrance. The walls themselves are constructed from heavy concrete with sufficient thickness to provide adequate shielding for operators and personnel in adjacent research and technical facilities. To operate the facility, it is pertinent to have a knowledge of the neutron fluence rates, and corresponding dose rates, at these locations surrounding the room housing the neutron generator.

The calculation of the neutron dose rates at these locations is problematic to accomplish using analytical methods. This is a consequence of the complex physical geometry of the generator room, the detailed composition of the construction materials, and the variation of neutron interaction probabilities with different isotopes at different incident energies. Therefore it is advantageous to utilize a computer-based particle transport simulator to calculate the required parameters. Modern neutron shielding calculations are predominantly performed using Monte Carlo techniques, the popularity of which may be credited to ever-increasing capabilities and processing power offered by modern computers. Users of such programs have also benefited from extensive nuclear data libraries that hold requisite particle interaction data for most isotopes of interest.

The development of shielding to attenuate neutrons was for practical purposes initiated by the Manhattan Project [1]. The shielding designed for reactor facilities was hindered by the lack of detailed data relevant to particle interaction probabilities of the constituent materials. This should not, however, be interpreted that the nature of the particle interactions were not understood to a large extent. It was well known prior to the Second World War that hydrogenous

media was quite adept at slowing-down neutrons through elastic scattering, and that hydrogen scatters neutrons nearly isotropically across a broad range of incident energies. As a result, the shielding at most facilities were adequate from a neutron dosimetry perspective. The early reactors were predominantly shielded with concrete as well as additional materials such as paraffin and iron.

The lack of detailed cross-section data for shielding materials was apparent, and the post-war environment provided the opportunity to remedy this limitation. Concurrent with these efforts was the development of several methodologies for calculating neutron attenuation through shielding, and more generally, solutions to the Boltzmann transport equation. These methods were deterministic in principle and used extensively prior to widespread implementation of stochastic Monte Carlo methods, although the latter was developed and used to a limited extent in the same time period.

Prior to advancements in computational power there were inherent limitations in the way real-life shielding problems could be modeled. Early methodologies were limited in the number of physical dimensions that could be modelled and the angular distribution of the collided portion of neutrons in deep-penetration scenarios [1]. It is important to note that these techniques were likewise developed to calculate reactor core reactivity, where a consideration of high levels of anisotropy in neutron scattering is typically not necessary to achieve acceptable results from calculations. Therefore some modifications were necessary to apply these techniques to shielding problems. The primary techniques were: the method of moments, the spherical harmonics method, and the discrete ordinates method [2].

The method of moments was the first method to be applied to generate solutions to the Boltzmann equation for shielding problems. The moments in this context do not have a definite meaning but are utilized only as a transform. The calculation is completed in the transform space then subsequently inverted to arrive at a solution. Initially, the angular flux density variable is expanded as a Legendre polynomial series then substituted into the Boltzmann equation and integrated over all angles. The spatial variable is removed by applying the moments of the Legendre coefficients of the angular flux density. Because the latter variable is subsequently

integrated over all space, the method of moments is limited in its applicability to problems approximating an infinite medium. Ultimately three groupings of moments are required: for the un-scattered flux density; for the scattered flux density; for the total flux density. The calculation procedure may be visually represented as a diagonal grid [2] [3]. This is because the zeroth moment can typically be calculated directly for any given Legendre order, while the converse is not true. The coefficients are calculated using a numerical integration scheme of the transformed transport equation. Thereafter it is possible to reconstruct the flux densities using typically, for neutron transport problems, the method of undetermined parameters.

Another technique implemented early on to solve the Boltzmann transport equation was the spherical harmonics method; its concepts are evident in other methodologies. It is applied to the transport equation by expanding the angular flux density, the source, and differential scattering terms as Legendre polynomial series. The expansions are substituted into the general Boltzmann equation, all terms are multiplied by the Legendre Polynomial, and finally integrated over all solid angle. The ultimate result is a set of differential equations. It is inherent that a larger expansion order results in a more precise solution, but also in a greater number of terms in the equation. A first order expansion gives an essentially linear distribution of the flux density. Higher orders of expansion likewise improve the accuracy of the differential scattering cross-sections in anisotropic scattering media and/or deep penetration problems.

The discrete ordinates method solves the transport equation numerically as a system of finite-difference equations, which require dividing space into a finite number of cells and relating the flux density from a central cell to adjacent cells. This is accomplished by integrating the conservative form of the Boltzmann equation over a finite-difference cell; replacing the integral-differential form of the equation with a system of difference equations. The differential scattering cross-section is expanded as Legendre polynomials, as is done with the spherical harmonics and moments methods. The system of difference equations can be solved through an iterative scheme. The diamond difference technique was developed to permit the solution of problems involving geometries of greater complexity. This enabled the Boltzmann equation to be integrated over an angular increment, yielding a two-point difference equation involving the angular flux density evaluated at the increment end points. This is necessary since the derived

discrete-ordinates equation has flux density variables applicable to spatial and energy group centers and end-points. This would otherwise result in a greater number of unknowns than there are terms required to arrive at a solution [3].

The Monte Carlo method of calculating spatially-dependent angular flux density has historically been difficult to implement in practice, particularly at a time when computational resources had not yet been developed to exploit the capabilities of such an approach. Its inherent advantage has always been the capability to model geometries in three dimensions. It has in the past been utilized in combination with the discrete-ordinates method when two-dimensional portions of a problem could be solved accurately with the latter. A Monte Carlo solution is strictly speaking not a method of solving the Boltzmann equation, but rather a method to calculate a solution based on the principles from which the transport equation was derived. The technique involves generating particles from a source and following the history as it travels through different sub-geometries and their constituent materials. The travel will include interaction events with individual isotopes, such as elastic scattering, inelastic scattering, and absorption. The direction of initial flight, interactions, and scattering angles, are determined by generated random numbers, between 0 and 1, in conjunction with the probability distribution of that particular event.

Since 2003, as a relatively new university, the University of Ontario Institute of Technology (UOIT) has been striving to meet its mandate in providing high-quality research and education within its nuclear engineering and radiation science programs. The construction of the Energy Research Center concluded in early 2011. This building presents the main space infrastructure for the Faculty of Energy Systems and Nuclear Science. In the basement of the building, the Applied Radiation Laboratory has been designed with a specific shielding to host different radiation sources, mainly a 10 Ci gamma irradiator, and a class II nuclear facility (neutron generator). Within this context, there has not been data published of fluence-rates and dose rates within the shielded room and in adjacent rooms incurred from neutrons emitted from a bare neutron generator operating with a deuterium-deuterium configuration.

The objective of this thesis is to ascertain the degree to which neutron flux and ambient dose rates incurred at key locations proximate to the facility are dependent on the neutron emission distribution when operating with different applied acceleration potentials. The values per source-particle are calculated by conducting a series of Monte Carlo simulations of neutron transport using MCNPX 2.7E through two approaches. Three anisotropic sources were simulated with energy and angular distributions corresponding to a specific charged deuteron energy. Additionally, an isotropic source approximation was modelled for comparative purposes. The total dose and fluxes were evaluated from simulation data in combination with experimental data gathered to determine the source intensity. Finally the calculated intensity and simulated data will be used to determine the total flux and dose rates.

Beyond the introduction, this thesis consists of three chapters, a conclusion, list of references, and appendices. The first chapter covers a general background on neutron interaction with matter as they pertain to attenuation through shielding and details the variation of interaction cross-sections with neutron energy and target isotope. Chapter 1 also discusses the various types of neutron sources commonly utilized and the principles under which they function, as well as, the designs and operational principles of common fusion-based neutron generators utilized in laboratory environment.

The second chapter provides a general description of the UOIT neutron generation facility. This includes dimensions, material compositions, and locations of detectors. A detailed description of the experimental setup and Monte Carlo simulation is likewise presented; including variance reduction techniques implemented and source specifications. Chapter three presents and discusses the results acquired from the experimental measurements and Monte Carlo simulations along with their comparison.

The conclusion summarizes the data and presents the key findings.

Chapter 1: Background on Neutron Interactions

1.1 Interactions in Neutron Attenuation

The primary purpose of this thesis as stated is to ascertain the energy-dependent neutron fluence rates at various locations originating from a well-defined source in a facility featuring heavy concrete wall construction. This subsection will review the neutron interaction mechanisms most commonly associated to particle transport through shielding and intermediate media. The interactions associated with neutron attenuation are, in broad terms: elastic scattering, inelastic scattering, and absorption.

Neutrons interact with the nucleus or nuclear potential field of an atom. The neutron particle possesses a nominally neutral electric charge and, as such, is incapable of purely electric interactions with electron orbitals [4]. Thus it travels along a path unaffected until it is in proximity of a nuclear force, at which point interaction is possible. The properties of neutron interaction, although highly variable along the entire energy spectrum, can be fairly consistent when observed over defined energy groups. These groups are commonly described, with some variation depending on the reference, as: thermal, 0 to 0.4 eV; epithermal, 0.4 eV to 1 keV; intermediate, 1 keV to 500 keV; and fast, above 0.5 MeV [3] [5].

Scattering interactions occur when a neutron traveling along a path effectively collides with a nucleus. For the scattering event to be characterized as elastic the momentum and kinetic energy in the collisional system must be conserved. The change in kinetic energy of the neutron after scattering is equal to the kinetic energy acquired by the recoiling nucleus; the internal energy of the nucleus remains unaltered. The energy difference between the incident neutron and the outgoing neutron is directly related to the scattering angle in the centre of mass system CM [6].

Elastic scattering interaction can broadly be defined in terms of two distinct mechanisms [7]. The first is compound elastic scattering and occurs when a neutron is absorbed by the atomic nucleus causing its mass number to increase by one unit. The nucleus gains an excitation energy equal to the sum of the total kinetic energy of the neutron and nuclide in the CM and the neutron binding

energy. In this excited state, the nucleus may decay by neutron emission with a kinetic energy equal to the incident particle. It is not possible to determine whether this was the same neutron that originally collided with the nucleus [7]. The probability of the formation of a compound nucleus increases if there is a resonance near the excitation energy.

The second mechanism of elastic scattering is potential scattering, which does not result in the formation of a compound nucleus. It occurs as a result of forces acting on the neutron when it approaches near the potential well of a nucleus; it is thus dependent on the size and shape of the nucleus. The probability of potential scattering is much greater than compound scattering at higher incident energies [4].

Inelastic scattering differs from elastic scattering in that a portion of the incident neutron energy appears as excitation energy of the target nucleus; kinetic energy is not conserved. The nucleus subsequently decays by photon emission. The probability of inelastic scattering increases with incident energy to where it becomes the predominant scattering mechanism with fast neutrons. However, it is a threshold reaction and requires a minimum kinetic energy of the incident particle, typically slightly above the first excitation level of the nucleus. If the kinetic energy is high enough then, further levels may become excited. The nucleus releases the excitation energy by emission of photons, either to the ground state or through intermediate levels. The probability of inelastic scattering also increases with nuclide mass, since the threshold excitation energy is lower with heavy nuclides.

A visual representation of the kinematics of neutron scattering is shown in Figure 1 and Figure 2.

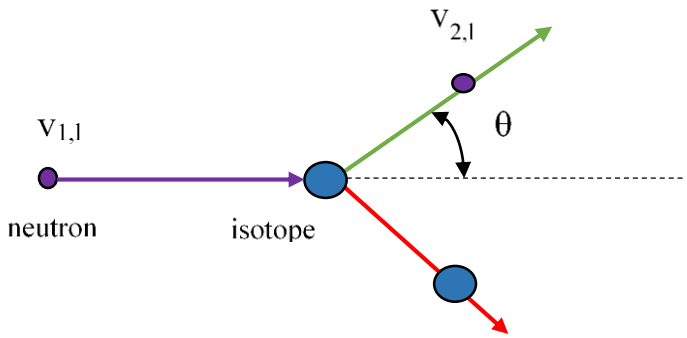

Figure 1: Neutron Scattering in Laboratory System

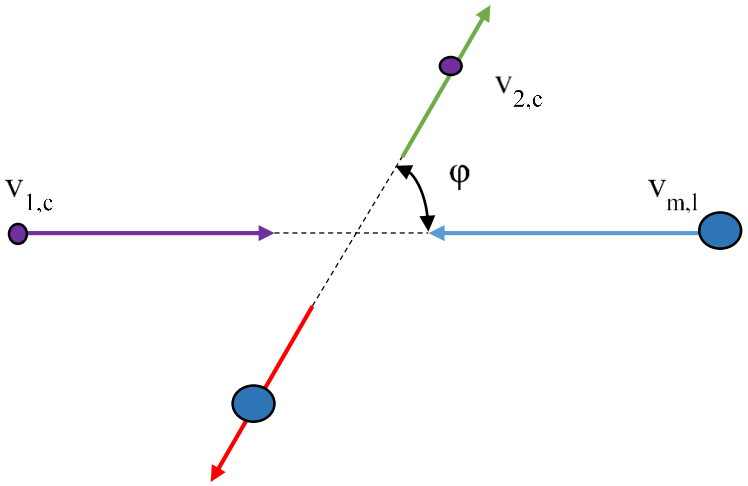

Figure 2: Neutron Scattering in Center of Mass System

The vectors in Figure 2 can be rearranged to the form shown in Figure 3, thus giving a visual representation of the final neutron energy in the LAB system.

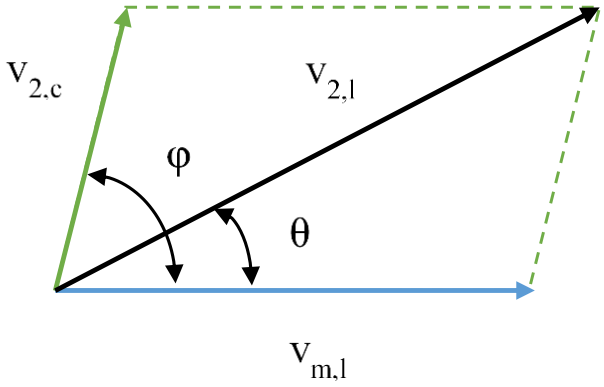

Figure 3: Final Neutron Energy in CM and LAB

In elastic scattering the final neutron energy can be related to the incident neutron energy and scattering angle in the CM by the following equation:

$$E_2^l = E_1^l \cdot \frac{M(n)^2 + M(^A_Z X)^2 + 2 \cdot M(n) \cdot M(^A_Z X) \cdot cos\,\theta^{cm}}{[M(n) + M(^A_Z X)]^2} \quad (1)$$

The equivalent relation in terms of scattering angle in the LAB is given by [8] [9] [4]:

$$E(n)_2^l = E(n)_1^l \cdot \left[\frac{M(n)}{M(n) + M(^A_Z X)} \cdot cos\,\theta^l + \left[\frac{M(^A_Z X) - M(n)}{M(^A_Z X) + M(n)} + \left[\frac{M(n)}{M(n) + M(^A_Z X)} \right]^2 \cdot cos^2\,\theta^l \right]^{\frac{1}{2}} \right]^2 \quad (2)$$

The equation for inelastic scattering is simply a generalization of elastic scattering [8], and reduces appropriately if the excitation energy is set to zero.

$$E(n)_2^l = E(n)_1^l \cdot \left[\frac{M(n)}{M(n) + M(^A_Z X)} \cdot \cos\theta^l + \left[\frac{M(^A_Z X) - M(n)}{M(^A_Z X) + M(n)} + \left[\frac{M(n)}{M(n) + M(^A_Z X)} \right]^2 \cdot \cos^2\theta^l - \frac{M(^A_Z X)}{M(n) + M(^A_Z X)} \cdot \frac{E^*}{E(n)_1^l} \right]^{\frac{1}{2}} \right]^2 \quad (3)$$

Occasionally the equation may be presented in terms of the Q-value rather than the excitation energy.

Elastic scattering occurs with all nuclides, but shielding material composed of light nuclides is advantageous for several reasons. Although the internal energy of the nuclide is unchanged, its mass has a significant effect on the amount of kinetic energy the neutron can lose in a single collision: the lighter the nuclide the more energy that can be transferred. Lighter nuclides also tend to scatter neutrons isotropically, while heavier nuclides may cause a distribution that is forward peaked. This does not, however, restrict shielding materials to only hydrogenous media.

Inelastic scattering by heavier nuclides is likewise an efficient mechanism of slowing down fast neutrons [1].

The most common explanation of anisotropy in scattering is with the optical model of the nucleus. The nucleus is assumed to be a diffuse absorbing sphere and the neutron, a plane wave. While mathematical solutions are rigorous, a simplified explanation is still helpful in explaining anisotropy in the angular distribution of scattered particles.

A plane wave of neutrons may be interpreted as a superposition of an infinite number of partial waves with different quantum angular momentum numbers, *l*. The impact parameter is the distance of approach, but its exact value is impossible to know. The distance of closest approach for a particular partial wave is the product of the quantum angular momentum number and the reduced wavelength [4] [8]. This distance must be less than or equal to the nuclear radius for the partial waves to interact with the nucleus.

$$x = \lambda_r \cdot l \leq R \qquad R = nuclear\ radius \tag{4}$$

Since the quantum angular momentum number can only take on integer values for solutions of the Schrödinger equation [8], the partial waves are represented as concentric cylinders surrounding the direction vector, assumed to be the Z-axis. The annular zones are defined between $\lambda_r l$ and $\lambda_r(l+1)$ and contain the *l*-zone. Within each *l*-zone lies the impact parameter. The cross sectional area of the annular zones increase proportionally with *l* as 2*l*+1. A graphical representation of this model is shown in Figure 4. The area is given by:

$$S_l = \pi \cdot [2l+1] \cdot {\lambda_r}^2 \tag{5}$$

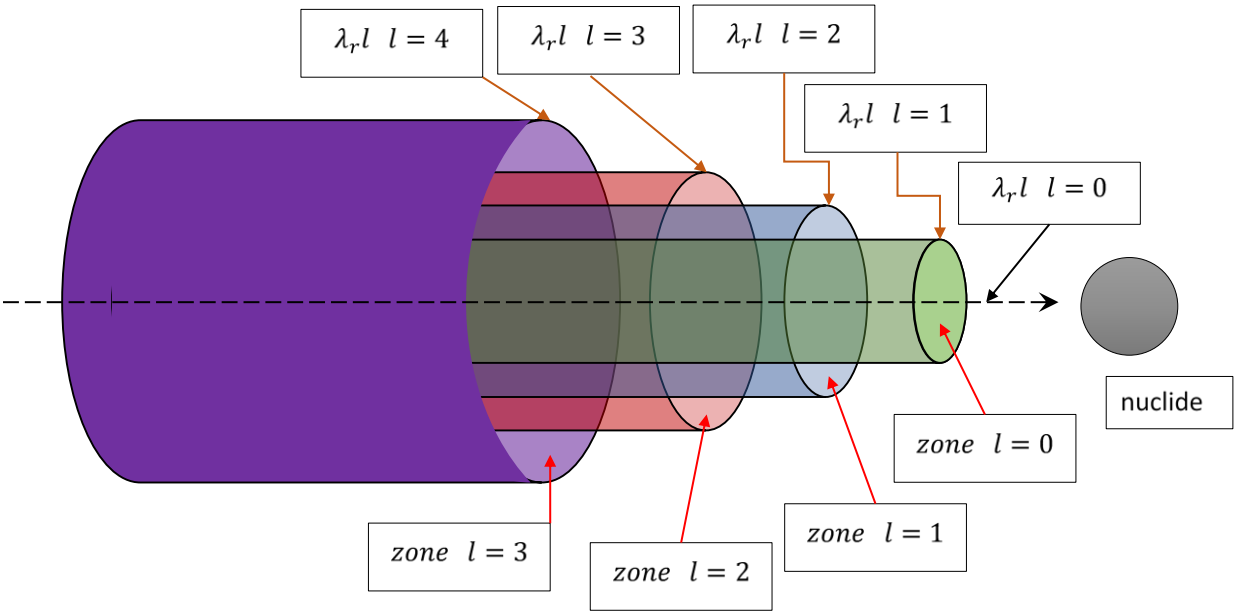

Figure 4: Partial Wave Model of Neutron

If the reduced wavelength is larger than the radius of the nucleus then only s-wave interactions can occur.

$$if \quad \lambda_r > R, \quad \frac{R}{\lambda_r} = l = 0$$

Similar relations can be made for other partial waves.

$$if \quad \frac{1}{2}R < \lambda_r \leq R, \quad \frac{R}{\lambda_r} = l = 1$$

$$if \quad \frac{1}{3}R < \lambda_r \leq \frac{1}{2}R, \quad \frac{R}{\lambda_r} = l = 2$$

$$if \quad \frac{1}{4}R < \lambda_r \leq \frac{1}{3}R, \quad \frac{R}{\lambda_r} = l = 3$$

S-wave scattering has been confirmed theoretically and experimentally to be isotropic in the CM system [7]. This is understandable since this partial wave lacks angular momentum and is scattered spherically irrespective of angle. Partial waves in higher *l*-zones have an increasing quantum angular momentum. The angular momentum of the partial wave with respect to the centre of the target nucleus is given by:

$$J = m_n v x = \frac{\lambda_r l h}{2\pi\lambda_r} = \frac{hl}{2\pi} \tag{6}$$

Where *x* is equal to the impact parameter for the closest approach. Because the reduced wavelength is inversely proportional to the square root of the kinetic energy, anisotropic scattering is evident in light nuclides only for high energies due to small nuclear radii. Conversely since heavier nuclei have larger radii, they cause a more anisotropic angular distribution for the same incident energy.

Radiative capture is the final interaction in the attenuation process, and involves the absorption of the incident neutron and formation of a compound nucleus [3]. This leaves the nucleus in an excited state, which subsequently decays by emission of photons.

$$ {}^{A}_{Z}X + n \rightarrow {}^{A+1}_{Z}X^{*} \rightarrow {}^{A+1}_{Z}X + \gamma + Q$$

$$Q = [M({}^{A}_{Z}X) + M(n) - M({}^{A+1}_{Z}X)] \cdot c^2 \tag{7}$$

The latter relation is in fact just the neutron separation energy for the compound nucleus.

$$Q = S_n({}^{A+1}_{Z}X)$$

The above equation indicates that the reaction energy value is positive, exoergic since the separation energy is positive for nuclides at the ground state. Radiative capture reactions therefore do not have a minimum energy threshold, which is of significant importance in shielding applications because, particularly for neutrons at thermal energies, they constitute the only energetically possible absorptive reaction [9].

After neutron capture, the compound nucleus is at an excitation level equal to the sum of the energy in the CM system, and the neutron separation energy of the compound nucleus.

$$E^{*} = S_n({}^{A+1}_{Z}X) + E^{cm} \tag{8}$$

$$where:\ E^{cm} = \frac{A}{A+1} \cdot E^{L}(n)$$

The compound nucleus decays by the emission of one or more photons, the total energy of which is typically equated to the excitation energy.

$$E^{*} = \sum_{i} E(\gamma)_{i} \tag{9}$$

However, an emitted photon possesses a non-zero linear momentum, which causes the nucleus to gain recoil energy [9]:

$$E^{l}_{recoil}({}^{A+1}_{Z}X) = \frac{E(\gamma)^{2}}{2 \cdot M({}^{A+1}_{Z}X) \cdot c^{2}} \tag{10}$$

The energy states of the compound nuclei can be characterized by the photon emission spectra. Light and medium isotopes have distinct energy levels with narrow widths, resulting in photon spectral peaks that are well defined; corresponding to the energy level transitions. Heavy isotopes, in contrast, emit a large range of possible gamma energies that are due to a high density of levels and poor separation. This effectively makes the photon energy a continuous statistical distribution. The ground state or low-lying isomeric state of the compound nucleus formed by radiative capture is often unstable with regards to radioactive decay [9]. This poses some issues with respect to neutron attenuation in that the materials utilized in shielding may become activated.

The probability of radiative capture in the lower energy ranges is roughly comparable to that of elastic scattering. In this region, the capture cross-section varies approximately in inverse proportion to the neutron velocity, 1/v. As the energy increases the cross-section function is no longer smooth and individual peaks with a Breit-Wigner characterization are evident, corresponding to resonances. The incident neutron energies at which individual resonance peaks typically are observed is inversely proportional to the nuclide mass. At higher energies, the resonances overlap and discrimination becomes more difficult, with the capture cross-section decreasing to a minute value.

1.2 Common Non-Accelerator Neutron Sources

Neutron sources commonly seen in laboratory environments rely on one of three principal mechanisms for the production of neutrons. The first is neutron-producing interactions of radiation emissions from radioactive substances, including photo-neutron and alpha-neutron sources. The second type is spontaneous fission of nuclides yielding neutrons. Finally neutrons can be produced using fusion reactions of accelerated charged particles. The first two will be reviewed presently, while neutron generators will be covered in the subsequent section.

Photo-neutron sources function on the principles of the (γ, n) reaction. A photon of sufficient energy is required to overcome the neutron separation energy of the target nucleus to eject a neutron. The energy of the neutron is approximately proportional to the incident photon energy. For large nuclides the emission energy is largely independent of the angle of the incident photon unless the latter possesses an energy near to the threshold value [2].

The source is manufactured within the confines of two distinct designs. The first involves mixing the converter, usually beryllium or deuterium, with the emitter: isotopes that emits high energy gammas. The second design separates the two compounds and uses an encapsulated gamma emitter with a shell constructed from a converter material [2].

Neutrons generated from a (γ, n) reaction are nominally monoenergetic. This is not entirely true for physical sources since the photons are subjected to scattering interactions in the material. This reduces the energy of the photon and alters the energy of the emitted neutron, provided the former remains above the threshold value. A listing of common sources of photo-neutron sources with average energy and yield is given in Table 1.

Table 1: Common Photo-Neutron Sources [2] [10]

Source	Average Neutron Energies (MeV)	Neutron Yield per 10^6 Bq
^{24}Na + Be	0.967	3.5
^{24}Na + D_2O	0.262	7.3
^{56}Mn + Be	0.128, 0.397, 0.761	0.78
^{56}Mn + D_2O	0.146, 0.214	0.08

^{72}Ga + Be	0.173, 0.476, 0.733, 0.748	1.4
^{72}Ga + D_2O	0.131, 0.139	1.6
^{76}As + Be	0.108, 0.382	1.9
^{88}Y + Be	0.151, 0.949	2.7
^{88}Y + D_2O	0.252	0.08
^{116m}In + Be	0.396	0.22
^{124}Sb + Be	0.022, 0.378	5.1
^{140}La + Be	0.761	0.08
^{140}La + D_2O	0.146	0.2
^{226}Ra + Be	0.68 maximum	0.8
^{226}Ra + D_2O	0.11 maximum	0.03
^{228}Ra + Be	0.848, 0.119	0.95
^{228}Ra + D_2O	0.195	2.6

Alpha-neutron sources have been traditionally used as neutron sources for several reasons:

- They are generally cheaper to operate than accelerator-based generators
- Their intensity varies predictably with time in accordance to the decay laws from the parent nuclide and progeny
- The physical size of the source is small due to a small neutron emission region
- The angular distribution is isotropic

The selection of emitter, which releases the alpha particle, and the converter, which undergoes the (α, n) reaction, is determined by the penetrability of the Coulomb potential barrier. Many nuclei would theoretically be capable undergoing this reaction with an alpha particle of sufficient energy, but since it possesses a positive charge, it is limited to interactions with light nuclei [4]. Converter isotopes are preferred on the basis of whether the reaction has a threshold incident particle energy and whether the Q-value indicates an exoergic reaction. Beryllium tends to generate neutrons of higher energies when compared to other converter materials due to a larger Q-value.

The neutron yield of an alpha-neutron source is dependent on alpha particle energy, and concentration and distribution of the emitter and converter elements. The estimated average yield is usually calculated by accounting for stopping powers of the alpha particles within the converter as well as the emitter. Maximum yields are calculated by assuming a thick target of converter material and no further alpha particle interaction with the emitter [2].

As with most reactions neutrons of maximum energy are emitted in the coincident direction of the alpha particle, but given the nature of the source, the angular distribution of the neutrons will be isotropic. A source of particular configuration generates a specific neutron energy spectrum for each individual monoenergetic alpha. There are however factors which prevent an ideal spectra from being detected. The alpha particles undergo charged particle interactions in the medium, between creation and absorption, and lose kinetic energy. This results in emitted neutrons of varying energy and a smoothed spectra. The neutrons themselves may also interact with the source through scattering, absorption, or fission with the emitter.

Overall the alpha-neutron sources have the following disadvantages:

- The source intensity is less than what would be produced in an accelerator
- The neutrons produced are not monoenergetic
- The neutrons are emitted along with gamma radiation
- The source may develop leaks

The average neutron energy and yield for alpha-neutron reactions is shown in Table 2.

Table 2: Common Alpha-Neutron Sources [2]

Source	**Average neutron energy**	**Neutron yield per 10^6 alphas**
^{210}Po + Li	0.48	1.3
^{239}Pu + Be	4.6	60
^{210}Po + Be	4.5	70
^{238}Pu + Be	4.5	80
^{241}Am + Be	4.4	75
^{244}Cm + Be	4.3	100
^{242}Cm + Be	4.1	110
^{241}Am + B	3	13
^{210}Po + C		0.10
^{241}Am + F	1.5	4.1
^{210}Po + F		5
^{210}Po + Na		1

Spontaneous fission is the final neutron emission mechanism to be discussed. Fission is the process where a heavy nucleus splits into two fragments while emitting neutrons and significant quantities of energy. Usually this is explained in terms of the liquid-drop model of the nucleus.

The binding energy per nucleon is well known to increase with atomic mass until peaking at Iron-56, where a decreasing trend begins. It is for this reason that fission is possible; the product nuclei are more stable. The fission process usually requires a neutron interaction to surpass the critical reaction energy value. This value is defined as the difference between the Coulomb energy and the Q-value, which in fission is stated as the average of a distribution [7]. In most fission processes, this critical energy is surpassed when the binding energy of the incident neutron is added to the nucleus.

The critical energy is not, however, a firm threshold for fission to occur. Spontaneous fission occurs in Uranium-238 which requires a calculated critical energy of approximately 5.85 MeV. This mechanism is theoretically possible for all heavy nuclei. The discrepancy between the critical energy and the reaction threshold is explained by a quantum mechanical leakage mechanism through the Coulomb barrier [7].

The actual rate of neutron generation is quite low for most nuclides. It occurs mainly in very heavy nuclides, where alpha particle emission is the primary decay mechanism. The most common spontaneous fission source is Californium-252. A listing of neutron yields for different nuclides is given in Table 3.

Table 3: Common Spontaneous Fission Nuclides [2]

Nuclide	**Neutrons/g/s**	**Nuclide**	**Neutrons/g/s**	**Nuclide**	**Neutrons/g/s**
U-233	8.6E-04	**Pu-242**	1.8E+03	**Cf-246**	7.5E+10
U-235	3.0E-04	**Pu-244**	1.9E+03	**Cf-248**	5.1E+09
U-238	1.36E-02	**Am-241**	1.18	**Cf-249**	2.5E+03
Np-237	1.1E-04	**Cm-242**	2.3E+07	**Cf-250**	1.1E+10
Pu-236	3.6E+04	**Cm-244**	1.1E+07	**Cf-252**	2.3E+12
Pu-238	2.7E+03	**Cm-246**	8.5E+06	**Cf-254**	1.2E+15
Pu-239	2.2E-02	**Cm-248**	4.1E+12	**Es-253**	3.0E+08
Pu-240	920	**Cm-250**	1.6E+10	**Fm-254**	3.0E+14
Pu-241	5.0E-02	**Bk-249**	1.1E+05		

1.3 Fusion-Based Neutron Generators

The aforementioned neutron sources have notable limitations including low intensity and inherent radioactivity. Traditional alternatives to reactor sources to generate neutrons include cyclotrons, linear accelerators, and Van de Graaff accelerators. These devices are capable of producing greater intensities than the radioactive sources but are expensive and operationally complex, limiting their construction to large facilities.

During the previous several decades deuterium-deuterium and deuterium-tritium neutron generators have gained popularity, nominally producing 2.5 MeV and 14.2 MeV neutrons respectively. These devices function as a small linear accelerator, forcing charged particles through a voltage potential towards a titanium-plated target [11] causing a fusion reaction. The titanium is bombarded during production by either deuterons or tritons, according the reaction specified for operational use, to form titanium hydrides. Titanium is selected due to its affinity to capture hydrogen and its isotopes, as well as its low stopping power [8]. These compact neutron generators are capable of being operated in continuous or pulsed modes.

The D-D generator functions by bombarding ionized gas-source deuterons into the deuterium-impregnated titanium target. This results in two equally probable sets of reaction products: helium-3 and a neutron, or, tritium and hydrogen. Any charged deuterons that do not react with the target deuterium will become trapped in the titanium matrix and serve to replenish the target resulting in a near constant intensity. Although, ultimately, the source of deuterium gas is exhausted and requires replacement.

The neutron angular distribution from the D-D fusion reaction cannot be described as isotropic even in the centre-of-mass frame of reference, as is depicted in Figure 5. Increasing charged deuteron kinetic energy results in an increased neutron intensity at 0° and 180°, and decreased intensity at 90° and 270°. In the laboratory frame of reference, the distribution tends to shift towards the forward emission cone, coincident with the direction of the charged particle, with increasing accelerator potential.

This anisotropic distribution, particularly at lower energies, is believed to be the result of unique properties of the deuterium nucleus. The deuteron has a low binding energy, 2.226 MeV, and large distance between proton and neutron [12] [13]. This results in a relatively large displacement between centre-of-mass and centre-of-charge. It was hypothesized that deuterons have a strong spin-orbit coupling and undergo P-wave interaction [13], which would account for this anisotropy. It was discovered subsequently that these last two factors are necessary conditions in the production of polarized particles, which is observed with neutrons created from D-D reactions [13].

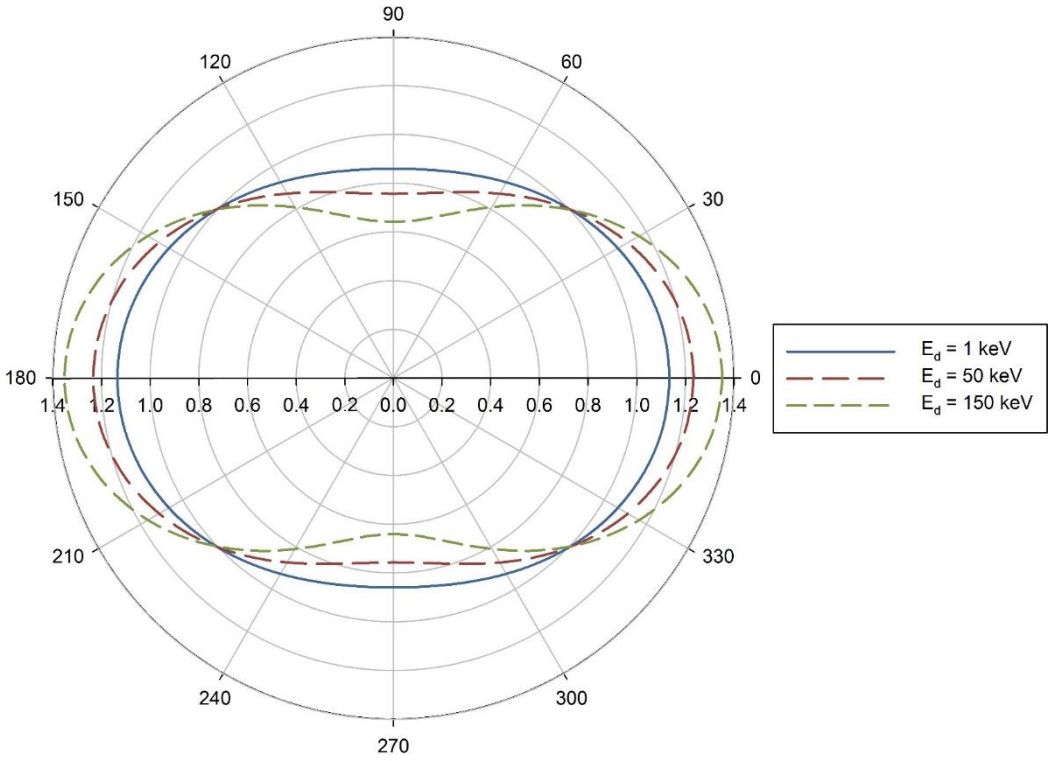

Figure 5: Normalized Distribution of D-D neutrons in CM

D-T generators typically function by colliding ionized deuterons into the tritium-impregnated titanium target [11]. The D-T reaction is much more probable to occur than the D-D reaction at the common accelerator potentials because of cross sections that are approximately two orders of magnitude greater. In contrast to the D-D generator, the D-T generator must be appropriately

shielded to prevent exposure to the tritium gas source. An inherent limitation with this concept is that the tritium will become depleted resulting in a gradually decreasing neutron intensity over the total time of operation. There are several designs available or under investigation that attempt to negate this last disadvantage. There is increasing development effort being directed towards gas-based targets, notably by NSD Fusion, which continually replenish the tritium target. Another alternative is to accelerate both gas-source deuterons and tritons into the mixed target, introducing tritium-tritium fusion reactions. T-T reactions do not produce a neutron energy spectrum that can be defined as monoenergetic [14]; the energy is not within a narrow range for a particular differential solid angle.

In contrast to D-D reactions, neutrons produced from D-T reactions are essentially isotropic in the CM. The effect of deuteron kinetic energy does not appear to alter the angular distribution with consistent effect, as is observable in Figure 6.

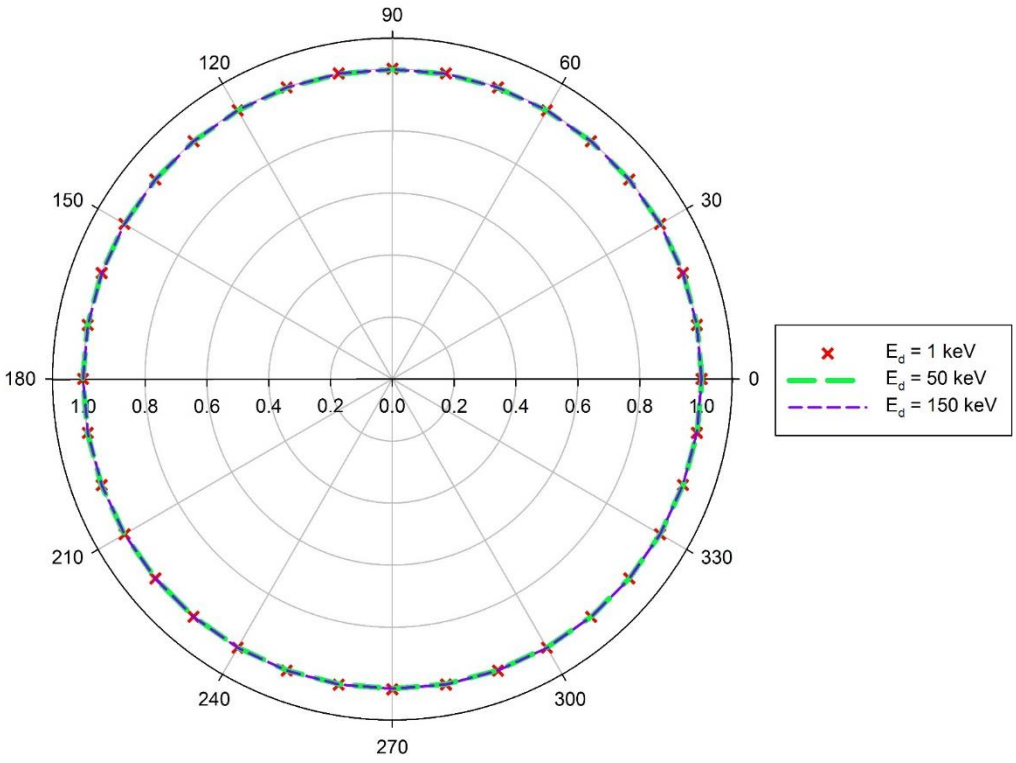

Figure 6: Normalized Distribution of D-T Neutrons in CM

The most common neutron generators use a gas source within a sealed accelerator assembly. The deuterium or tritium gas is ionized by a Penning ion source, which consists of a hollow

cylindrical anode at 1 kV to 2 kV potential with grounded cathode plates at each end of the anode [8] [11]. An external magnet surrounds the ion source and generates a coaxial field of several hundred Gauss [11]. As the gas is injected at approximately 0.1 Pa, the electric field causes it to become ionized, forming a plasma. The orientation of the electric field and magnetic field causes the electrons to oscillate in helical trajectories between the cathodes, though some strike the anode [15]. The confinement of the electrons aids in sustaining the plasma. The ions are in contrast not confined and can escape through an orifice at the centre of one of the cathodes into the accelerator section. The titanium target at the end of the accelerator section is biased to a negative voltage, while the plasma is at ground potential [8]; causing the positively charged ions to become attracted and collide with the target. There may also be intermediate electrodes, sometimes described as a focusing lens, to focus the ion beam onto the target [14].

The D-D fusion reaction at the energies of interest, as it is utilized in the P-385 neutron generator and being simulated as part of this thesis, may be described by the following qualitative relation:

$$D^+ + {}^2_1H \rightarrow {}^4_2He^* \rightarrow {}^3_2He + n$$

$$M({}^4_2He) = 4.00260325415\ amu \quad M({}^3_2He) = 3.0160293191\ amu$$

$$M({}^2_1H) = 2.0141017778\ amu \quad M(n) = 1.0086649157\ amu$$

The charged deuteron collides with stationary deuterium forming a compound Helium-4 nucleus, excited to a virtual energy level near the resonance at 24250 keV [16]. The mass defect from the formation of a compound nucleus being 23847 keV. It is described as a virtual level because it is greater than the neutron separation energy of Helium-4.

$$S_n = [M({}^3_2He) + M(n) - M({}^4_2He)] \cdot c^2 = 20578\ keV$$

The Q value of the reaction can be deduced from a mass-energy balance of the products and reactants.

$$Q = \left[2 \cdot M({}^2_1H) - [M({}^3_2He) + M(n)]\right] \cdot c^2 = 3269\ keV$$

The threshold deuteron energy can be derived using two-body kinematic calculations for an outgoing neutron with an angle of θ degrees relative to the incident deuteron [8].

$$E^l(D^+) = -Q \cdot \frac{M(^3_2He) + M(n)}{M(^3_2He) + M(n) - M(^2_1H) - \frac{M(n) \cdot M(^2_1H)}{M(^3_2He)} \cdot [\sin\theta]^2} \quad (11)$$

For minimum transfer of kinetic energy from the charged deuteron to the compound nucleus, the neutron direction must be the same as the accelerated particle [8].

$$E^l(D^+) = -Q \cdot \frac{M(^3_2He) + M(n)}{M(^3_2He) + M(n) - M(^2_1H)}$$

$$E^l(D^+) \cong -2Q$$

Since Q is equal to 3.269 MeV the above relation indicates that the D-D reaction is exoergic and does not have a minimum threshold deuteron kinetic energy. Although the reaction cross section is not independent of deuteron energy as seen in Figure 7.

The D-T reaction is characterized as follows:

$$D^+ + {}^3_1H \rightarrow {}^5_2He^* \rightarrow {}^4_2He + n$$

$$M(^3_1H) = 3.0160492777\ amu$$

The Q value of the reaction is again determined from a mass-energy balance of the products and reactants.

$$Q = \left[[M(^2_1H) + M(^3_1H)] - [M(^4_2He) + M(n)]\right]c^2 = 17589\ keV$$

The Q value for the D-T reaction is 17.589 MeV, and is similarly exoergic. The mass defect from the creation of a helium-5 nucleus is 16792 keV. This corresponds to the calculated virtual energy level at 16.84 MeV [17]. The neutron separation energy for the compound Helium-5 nucleus is a negative value, typically cited as -735 keV [18].

The D-T reaction has a neutron production cross-section on average about two orders of magnitude greater than the D-D reaction and T-T reaction, Figure 7.

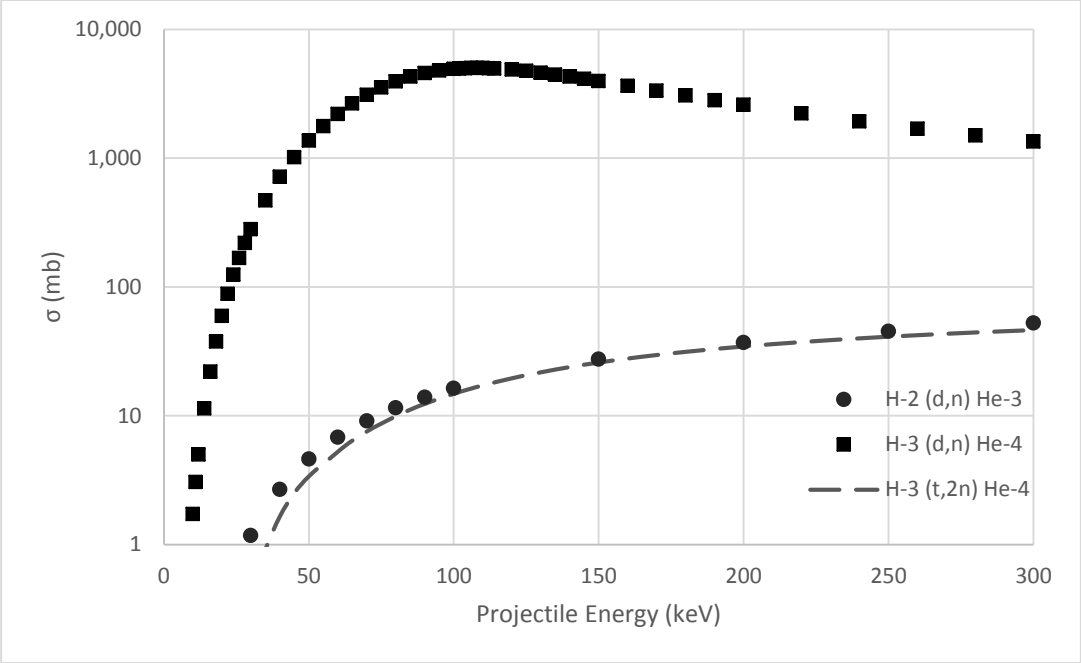

Figure 7: Cross Section of Fusion Reactions

The derivation of the relationship for the neutron energy is applicable to D-D and D-T reactions at non-relativistic energies. It is important that consideration be made of the recoil energy imparted to the residual nucleus to obtain an accurate value. The following two-body kinematical equation was taken from [14] and was consistent with values calculated using DROSG-2000 accelerator code.

$$E^l(n) = \left[a \pm \sqrt{a^2 + b}\right]^2 \tag{12}$$

$$where: \quad a = \frac{\cos\theta^l \cdot \sqrt{M(^2_1H) \cdot M(n) \cdot E^l(D^+)}}{M(n) + M(^3_2He)}$$

$$b = \frac{M(^3_2He) \cdot Q + E^l(D^+) \cdot [M(^3_2He) - M(^2_1H)]}{M(n) + M(^3_2He)}$$

The effect of emission angle on neutron energy is shown in Figure 8 and Figure 9 for D-D and D-T reactions respectively. Being that they are both two-body reactions the graphs are very similar, as anticipated.

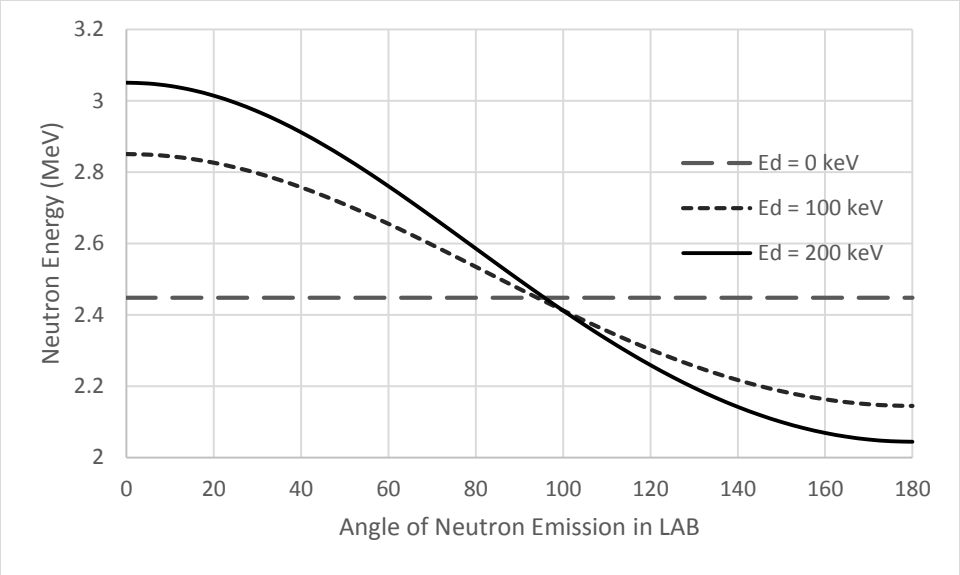

Figure 8: D-D Neutron Energy

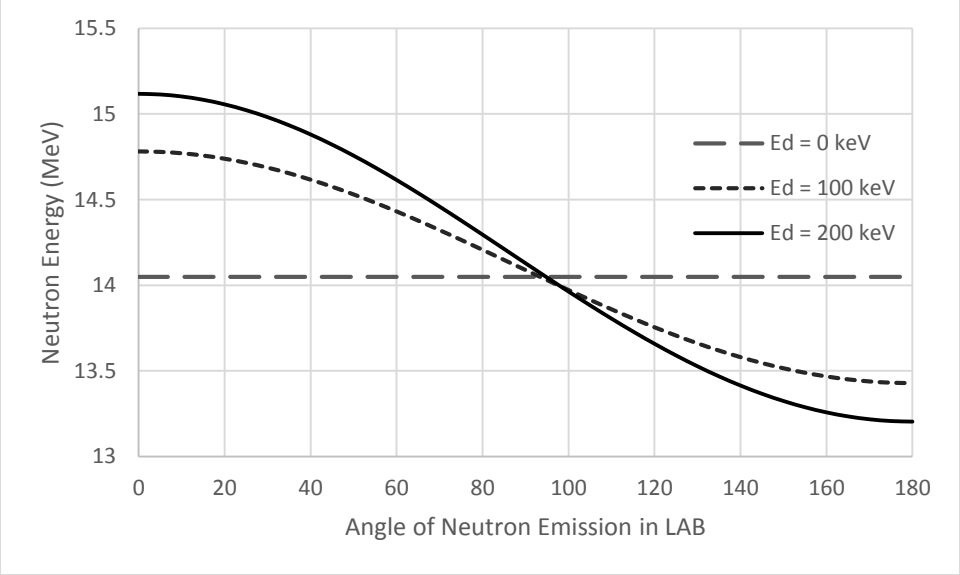

Figure 9: D-T Neutron Energy

The yield of a neutron generator is affected by many factors beyond applied accelerator potential. The probability of the reaction, generally, increases with greater incident projectile energy, but it is impossible for the entire charged particle flux to interact with the first monolayer of embedded deuterium or tritium. A portion of the ion beam will slow-down to lower energies in the target before interaction, resulting in slightly different energy and angular distribution of the emitted neutrons. A higher number of embedded target atoms per titanium atom, denoted

as r in the equation below, near the surface of the target matrix does increase the likelihood that higher energy charged particles will interact. The total intensity of the source may be estimated by calculating the stopping power over suitably small increments of energy and target thickness [8].

$$I_j = \left(\frac{dE}{dX} \cdot \Phi_D \cdot \rho \cdot \Delta E \cdot \Delta X \cdot r \cdot \rho_{Ti}\right)_j \tag{13}$$

The above equation usually is not particularly accurate even if the requisite parameters are known. In the context of this thesis and the neutron generator modeled it will not be utilized to estimate neutron yield. This is partly due to the following data not being available: the exact geometry and thickness of the layer of titanium deuteride in the target; the amount of accumulated Helium-3 and hydrogen in the target matrix; the propensity of the ion source to generate diatomic deuterium ions rather than monatomic deuterons.

The thickness of the target determines the energy loss of the deuterons prior to interaction. If the target is thick, this will result in broader peaks in the neutron energy spectrum. Neutron generators are typically intended to be a monoenergetic neutron source and the use of an excessively thick target would compromise this desired property. A thin target would cause only a portion of the deuterons to interact, but within a narrower energy range; energy and angular distributions of the neutrons would be more consistent.

The range calculation, using for example SRIM, requires knowledge of the relative atomic densities in the target. Since Helium-3 does not decay, and hydrogen is generated with roughly equal probability as neutrons in a D-D reaction, the concentration of the former two products is proportional to the operational parameters of the device: time, accelerator potential, and beam current. This data are not realistically obtainable. The effect of deuterium concentration in the target on the stopping power can be seen in Figure 10, where *r* is again the number of deuterium atoms per titanium atom.

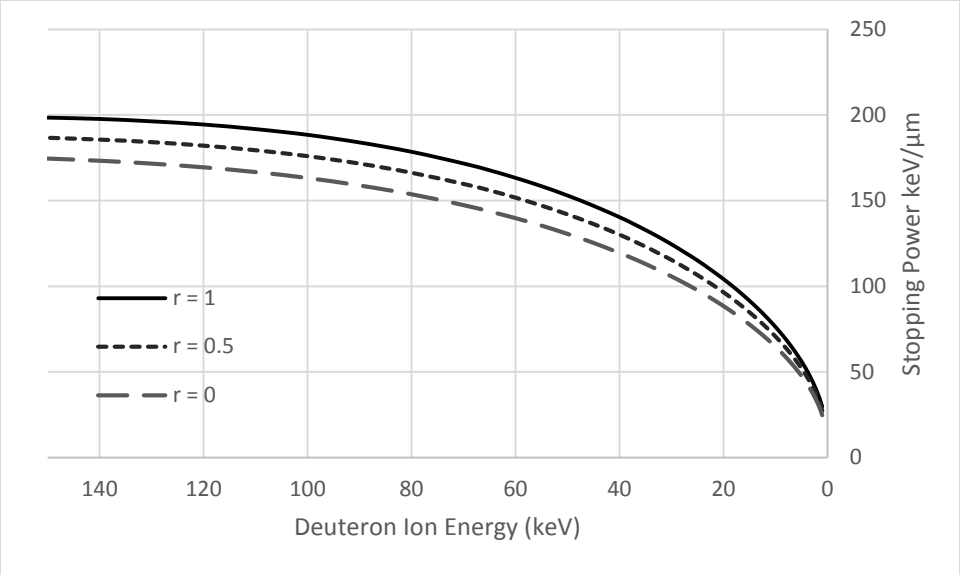

Figure 10: Stopping Power in Titanium for Various Deuterium Concentrations

The difficulty with using the above equation to estimate neutron intensity is a tendency for Penning-ion source neutron generators to produce diatomic and/or triatomic deuterium ions which break-up when finally hitting the target [19]. This has the effect of halving the kinetic energy per nucleon colliding with the target and significantly reducing the probability of undergoing a neutron generating reaction. In contrast, RF ion-source generators do not suffer from this effect to as nearly a significant a degree [11] [19].

The D-D reaction ceases to produce a neutron field that can be described as monoenergetic once the incident deuteron energy exceeds the break-up value. The break-up reaction occurs when the deuteron separated into an individual proton and neutron. The threshold value is given as 4.45 MeV for the $^{2}H(d,np)^{2}H$ reaction and 8.9 MeV for the $^{2}H(d,2n)2^{1}H$ reaction [19]. The cross-section increases rapidly relative to the primary $^{2}H(d,n)^{3}He$ reaction once the threshold is exceeded. The break-up neutrons are concentrated in a narrow forward emission cone, are of lower energy than those generated from the primary reaction, and form a broad energy continuum. Similarly, the D-T reaction has a threshold for the formation of break-up neutrons at incident deuteron energies of 3.71 MeV and 4.92 MeV for the $^{3}H(d,np)^{3}H$ and $^{3}H(d,2n)^{3}He$ reactions, respectively [19]. Commercially available sealed neutron generators are not capable

of accelerating deuterons to sufficient energies to produce breakup reactions and produce neutrons that are nominally monoenergetic.

The final fusion reaction used in neutron generators, albeit less commonly, involves bombarding ionized tritons onto a tritium target. It shares in common with the D-D and D-T sources in that it is an exoergic reaction enabling low acceleration potentials to be used, but differs in that it produces a broad spectrum of neutrons from 0 MeV to approximately 9 MeV. This may be found in T-T based generators or alternatively in mixed beam accelerators. The angular distribution can be considered as isotropic in the CM and becomes somewhat forward peaked in the LAB with increasing incident triton energy. A Helium-4 nuclide is formed along with the two neutrons with the Q-value calculation shown below:

$$Q = \left[[M(^3_1H) + M(^3_1H)] - [M(^4_2He) + 2 \cdot M(n)]\right] \cdot c^2 = 11333\ keV$$

A complexity in calculating the neutron energies produced from the T-T reaction lies in the fact that it is a three-body problem, in contrast to the D-D and D-T reactions which are two-body problems. This precludes the possibility of determining unique energies for each of the emerging particles using solely conservation of energy and momentum. It is however possible to calculate the range of neutron energies by fixing one neutron energy and solving for the other. The following non-relativistic equation for three-body kinematics was taken from [20].

$$E^l(n_2) = \left\{ \frac{\left[-B \pm [B^2 - 4 \cdot A \cdot C]^{\frac{1}{2}}\right]}{2 \cdot A} \right\}^2 \tag{14}$$

$$Where,$$

$$A = M(n) + M(^4_2He)$$

$$B = 2 \cdot [\cos\theta_1^l \cdot \cos\theta_2^l + \sin\theta_1^l \cdot \sin\theta_2^l \cdot \cos\theta_1^l] \cdot [M(n) \cdot M(n) \cdot E^l(n_1)]^{\frac{1}{2}} - 2 \cdot \cos\theta_1^l \cdot [M(n) \cdot M(^3_1H) \cdot E^l(T^+)]^{\frac{1}{2}}$$

$$C = [M(n) + M(^4_2He)] \cdot E^l(n_1) - 2 \cdot \cos\theta_1^l \cdot [M(^3_1H) \cdot M(n) \cdot E^l(T^+) \cdot E^l(n_1)]^{\frac{1}{2}} + [M(^3_1H) - M(^4_2He)] \cdot E^l(T^+) - M(^4_2He) \cdot Q$$

Using this equation, it was possible to generate a locus plot, in Figure 11, of the possible neutron energies for three different incident triton energies, although it should be noted that this does not indicate the probability of a particular neutron being generated. It is apparent that increasing the triton bombarding energy increases the range of possible energy combinations.

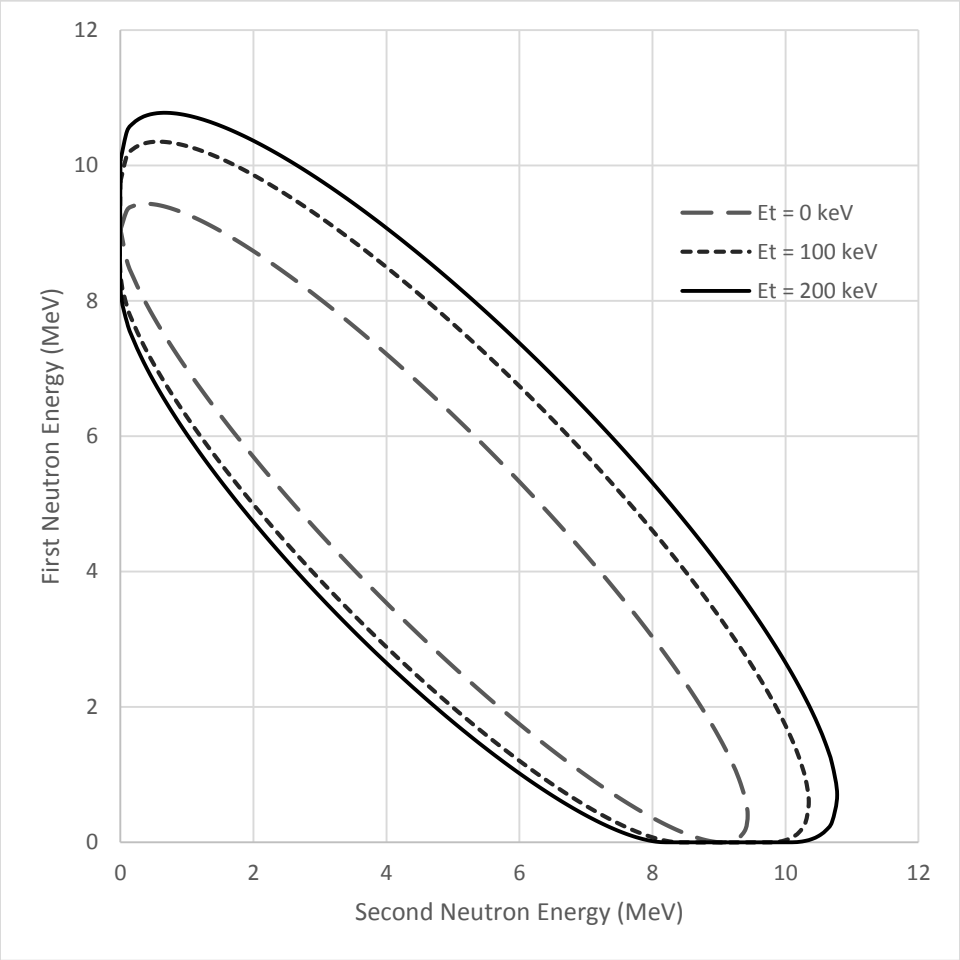

Figure 11: T-T Neutron Energies

1.4. Bubble Detectors

The operational principle of the bubble detector is predominantly energy deposition by recoiling nuclei created through elastic scattering of incident neutrons on halocarbon isotopes [21]. As these nuclei travel, they deposit energy in the active material and enable phase transition to occur. Inelastic scattering may occur if the kinetic energy of the system is greater than the first excitation level of the nuclei.

The bubble detector can be physically described as a transparent sealed tube containing a suspension of small droplets of halocarbon fluid dispersed in a matrix of polymerized gel [21]. The total volume of emulsion is typically a 10 ml containing ten thousand to a hundred thousand droplets of diameter typically between 5 μm to 100 μm [22]. The desired emulsion is created by adding specific amounts heavy salt to an aqueous solution to attain the same density as the droplets, thus preventing downward migration. The solution is then polymerized to prevent upward travel of the subsequently generated vapour bubbles [23]. Most methods of making an emulsion with uniform droplet sizes are proprietary.

For effective use the droplets themselves must remain transparent when not exposed to interacting particles. Prior to the exposure to a neutron fluence the pressure and temperature conditions within the emulsion should correspond to a metastable superheated state of the fluid and be conducive to achieving nucleation in the droplets to form vapour bubbles [22] [24]. A superheated liquid is defined as a liquid at temperatures and pressures that correspond to the vapour region in the phase diagram. Spontaneous liquid-to-vapour phase transition is not possible through superheated conditions exclusively, but is triggered by a local thermal spike caused when a critical amount of energy is deposited by a particle within the droplet [23]. The energy that is used to overcome a potential barrier is not, however, all the energy that is required. This is because the droplets will likely not be superheated sufficiently to undergo homogeneous nucleation, and will require additional irreversible work to undergo heterogeneous nucleation. This is attributable to viscous forces, latent vaporization heat, and kinetic energy transfer to the bubble wall [23]:

$$E_c = \frac{16\pi}{3(p_i - p_0)^2}\left[\frac{\sigma_b(T_c - T)}{T_c - T_b}\right]^3\left[1 + \frac{2\Delta H}{p_i - p_0} - 3\frac{T(T_c - T_b)}{\sigma_0(T_c - T)}\frac{d}{dT}\left(\frac{\sigma_b(T_c - T)}{T_c - T_0}\right)\right] \quad (15)$$

The interface surface tension is defined in terms of: the surface tension at reference boiling temperature, σ_b at T_b; the critical temperature of the fluid, T_c. The critical temperature is the value above which the liquid phase transitions to gas, and cannot be recompressed to the former state.

Bubble formation will occur when energy, E_c, is deposited within a distance l_c; defined as linear function of the critical radius, R_c [23].

$$R_c = \frac{l_c}{a} = \frac{2}{p_i - p_0}\frac{\sigma_0(T_c - T)}{T_c - T_b} \quad (16)$$

Assuming that a particle transfers energy linearly as it travels, the deposited energy is the product of the critical length and the displacement rate of energy transfer. It is important to note that not all the energy deposited will contribute to vapour bubble formation, only the portion of the total that is converted to heat. When the energy deposited is sufficient to create a vapour bubble of critical size the entire droplet will vaporize and produce a macroscopic bubble up to a millimetre in diameter. When the energy is insufficient the subcritical bubbles created will collapse back into the liquid phase. The vapour bubble will remain in the same location within the matrix as the liquid droplet. Due to a minimum required energy to generate vapour bubbles the bubble dosimeter is essentially a threshold detector [22].

The response of bubble detectors with different compositions can be compared through a parameter called the reduced superheat, which is the normalized operating point of an emulsion within the temperature range corresponding to the metastable superheated state [22].

$$s = \frac{T - T_b}{T_c - T_b} \quad (17)$$

For a bubble detector with known droplet composition it is possible to determine the threshold energy by exposing it to a fluence of mono-energetic neutrons and measuring the response, as a

function of temperature at discrete pressures. Once the process is repeated for different neutron energies, it is possible to combine the data and generate constant-pressure curves of neutron energy versus temperature. The threshold nuclei recoil energy, $E_{R,th}$, can be expressed as a function of energy at the boiling temperature, E_b [24].

$$E_{R,th} = E_b e^{-K(T-T_b)} \tag{18}$$

Because there is a minimum energy requirement to achieve critical bubble size, there must be a corresponding minimum energy the recoiling particle must possess. Fast neutrons can produce recoil nuclei with energies greater than the minimum through elastic scattering inside the halocarbon droplets. The maximum nuclei recoil energy occurs at a scattering angle of 180°, and the minimum recoil energy at 0°. The recoil energy is also dependent on target nuclide mass; a neutron can transfer more kinetic energy to a lighter nuclide at the same scattering angle than a heavier nuclide. The probability that a recoil nuclei will generate a vapour bubble of critical size is given in [23] as:

$$P\left(E_R^i, E_{R,th}^i(T)\right) = 1 - e^{-\alpha\left(\frac{E_R^i - E_{R,th}^i(T)}{E_{R,th}^i(T)}\right)} \tag{19}$$

The general equation for the efficiency that a recoil nuclei triggers a critical phase transition in the droplet is the ratio of the integrated recoil energy spectrum with the threshold energy lower bound to an equivalent with a zero energy lower bound; again given in [23]as:

$$\epsilon^i(E_n, T) = \frac{\int_{E_{R,min}^i}^{E_{R,max}^i} \left[\frac{dn_i}{dE_R^i} P\left(E_R^i, E_{R,th}^i(T)\right)\right] dE_R^i}{\int_0^{E_{R,max}^i} \left[\frac{dn_i}{dE_R^i}\right] dE_R^i} \tag{20}$$

The above equation is not readily solvable for the energies of interest because of the prevalence of anisotropic angular distributions of scattered particles.

The response of the detector can be estimated from the following relation:

$$R(E_n, T) = \Phi(E_n)\mathbb{V} \sum_{i=1}^{k} N^i \epsilon^i(E_n, T) \sum_{j=1}^{q} \sigma_j^i(E_n) \tag{21}$$

With greater superheat the sensitivity increases because of the additional contribution of recoil protons from the surrounding matrix. Gamma photons interacting with the electron orbitals have negligible effect on this type of dosimeter since light charged particles, electrons, have insufficient energy to cause the microscopic vapour bubbles to reach the critical vaporization size [21]. Likewise, bubble detectors are immune to the effects of background radiation.

Thermal and intermediate energy neutrons can be detected with these bubble detectors if the latter is modified to increase sensitivity by adding an isotope to the fluid that produces heavy charged particles when interacting with the former [21]. Halocarbons containing chlorine are more sensitive to neutrons colliding in this energy range. This is partly due to the Cl-35(n, p)S-35 reaction, which will generate sulfur recoils and a proton. Inelastic scattering is also more probable with chlorine-35 than with fluorine-19.

When the measurement is concluded, the number of bubbles can be counted manually or with an optical scanner. The amount of overlap of the bubbles limits the duration of the measurement as counting becomes increasingly difficult. As a bubble detector is exposed to neutrons the number of available droplet sites decreases as they vaporize. This results in an exponentially decreasing sensitivity over time. The detector can be reused by applying pressure to re-condense the bubbles and subsequently releasing the added pressure to return the droplets to a metastable superheated state.

The sensitivity of Bubble detectors have a strong dependence on ambient temperature as a result of the dependence of the triggering mechanism on the degree of superheat. A method to reduce this temperature dependence is to incorporate a volatile liquid in the free space within the tube above the emulsion surface [22]. As the temperature rises the vapour pressure of this liquid does likewise, increasing the pressure on the emulsion and reducing the change in superheat. Alternatively a temperature transducer can be utilised in conjunction with heating elements to maintain a constant temperature slightly above ambient.

Chapter 2: Methodology Description

2.1 Facility Description

The neutron generation facility was developed and constructed with sufficient shielding and distance to provide protection for research staff, students, and support personnel, from acquiring radiation doses greater than stipulated limits. This is particularly important since the facility is surrounded on the same floor by control rooms, other laboratories, and rooms housing auxiliary support equipment. It is also beneath occupied rooms on the main floor that are not access restricted. A three dimensional view of the facility is shown in Figure 12.

The facility is located in the basement of the Energy Research Center entirely below ground level. The generator is placed roughly in the center of the 775 cm by 775 cm square area. Three of the four walls surrounding the generator are composed of heavy concrete of density 3.8 g/cm^3. All the heavy concrete walls are 100 cm thick. One side has a wall constructed from ordinary concrete of density 2.35 g/cm^3, and backed with ground soil.

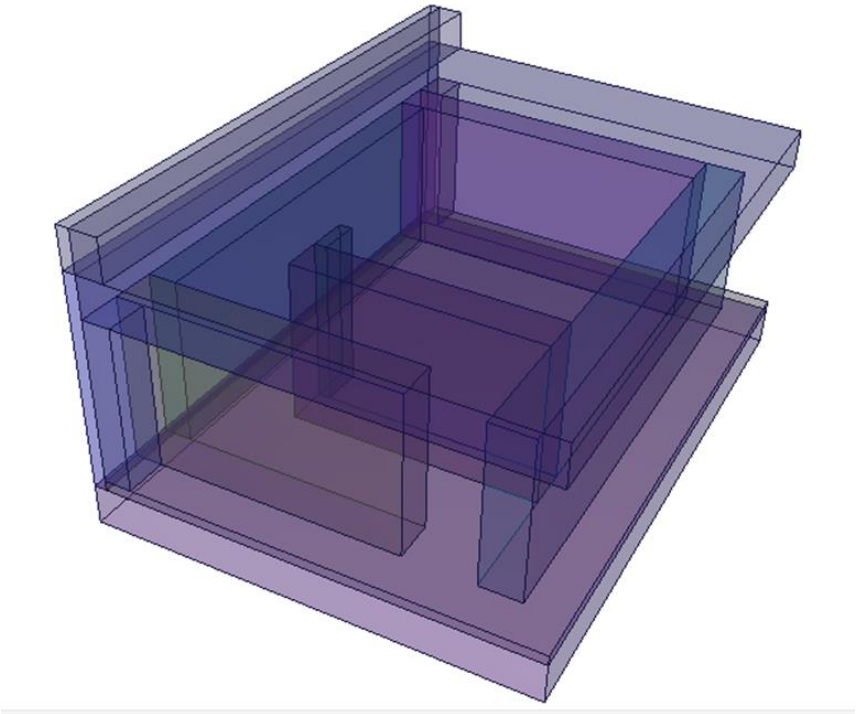

Figure 12: 3-D Representation of Facility

A functionally efficient neutron shield subjected to a fast neutron fluence requires a combination of light and heavy nuclei, in a specific range of ratios, to permit elastic and inelastic scattering to occur concurrently [10] [25]. As was reviewed previously, the slowing-down of fast neutrons to intermediate energies is accomplished primarily through inelastic scattering with heavy nuclei. From the intermediate energy, neutrons are slowed mainly by elastic scattering with light nuclei. Finally, neutrons at or near thermal energy levels are absorbed. Heavy nuclei are also instrumental in attenuating the photons generated as a result of radiative capture. In these respects concrete is a desirable material, and is modifiable by the addition of various aggregates, ores, or iron shot, to decrease the transmitted fluence [25].

Figure 13 shows a top-down view of the geometry simulated in MCNPX 2.7. The red numerals correspond to materials within each cell. The simulated atomic fractions of each material is listed in Table 4. All dimensions are presented in cm units.

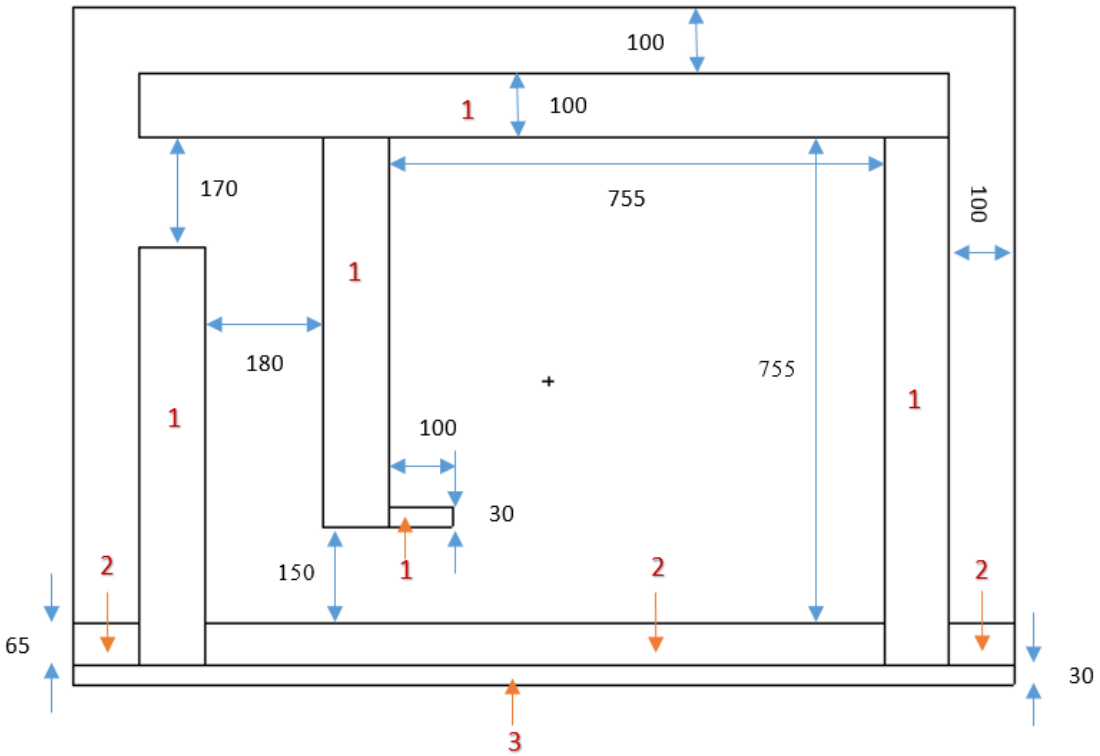

Figure 13: Neutron Generation Facility, YX-Plane

Table 4: Material Atomic Fractions [25]

ID	Material	Density [g/cm³]	Element	Fraction	Element	Fraction	Element	Fraction
1	**Heavy Concrete**	3.8	H Mg Ca	8.39E-02 1.59E-02 2.05E-02	C Al Ti	1.13E-02 2.02E-02 7.80E-02	O Si Fe	5.57E-01 3.17E-02 1.82E-01
2	**Regular Concrete**	2.35	H Mg K	8.48E-02 3.00E-03 6.86E-03	O Al Ca	6.04E-01 2.48E-02 2.05E-02	Na Si Fe	9.47E-03 2.42E-01 4.65E-03
3	**Soil**	1.7	H Si	1.59E-01 1.90E-01	O	5.71E-01	Al	8.01E-02
4	**Air**	0.00121	C Ar	1.25E-04 1.17E-02	N	6.87E-01	O	3.01E-01

The side view of the facility, looking along the X-axis as modeled in MCNP, is shown in Figure 14. The distance from the floor to the ceiling is 400 cm. The ceiling itself is constructed from heavy concrete of 100 cm thickness. The basement floor is simulated as being constructed of 25 cm thick regular concrete, beneath which is a 100 cm layer of soil. An assumption was made with respect to the intersection of the walls and floor; the heavy concrete walls do not extend beneath the surface of the floor.

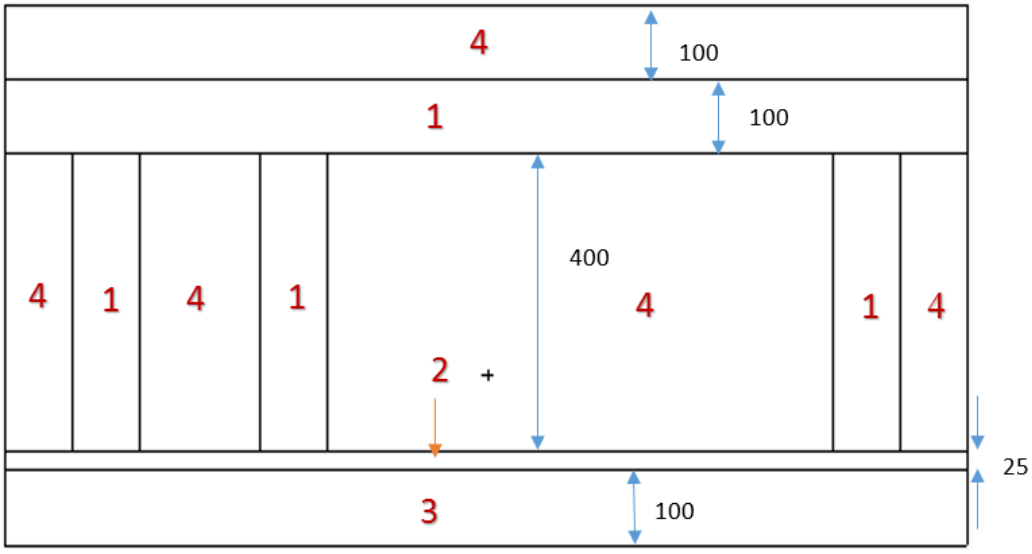

Figure 14: Neutron Generation Facility, YZ-Plane

Figure 15 shows the side view along the Y-axis and details the geometry of the regular concrete wall. The heavy concrete ceiling is simulated as extending to the soil. Several assumptions were made as to the design of the portion of the main floor that was modeled, in particular, that air is present directly above the soil located outside the facility.

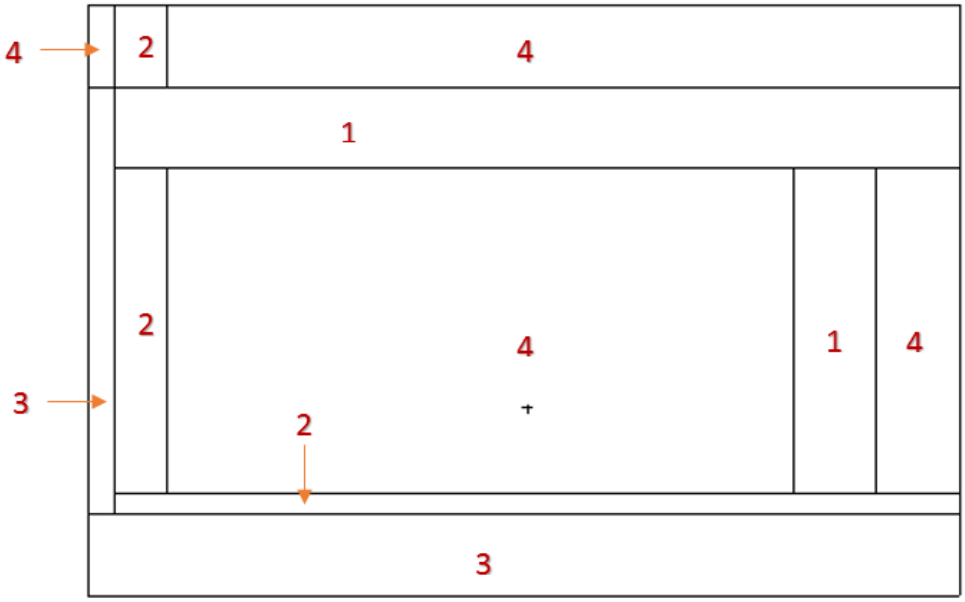

Figure 15: Neutron Generation Facility, XZ-Plane

The space outside the geometry modeled, displayed in Figure 13 through Figure 15, does not contain any material. Further modeling of more distant spaces was not undertaken, as it was not expected to appreciably affect the fluence and dose simulated at the tally locations. To elaborate, it is likely that any particles escaping through the ceiling would, in high probability, have the insufficient kinetic energy to penetrate back into the basement. At lower energies, neutrons tend to scatter elastically and with less propensity for forward-peaked scattering angles. This results in greater energy loss per collision and a greater chance of absorption.

2.2 Monte Carlo Simulation

The location of the tallies about the neutron generation facility is shown in Figure 16, with displacement from the indicated origin given in Table 5. The tally locations A and C were chosen because the MCNP-calculated dose and fluence rates would give an indication as to the magnitude of scattering in the maze, as well as, the relative fraction of neutron particles that penetrate the wall directly between the source and the tallies. When the neutron generator is operating no personnel should be present at these locations. Tally locations B, D, and E, were selected because they are not isolated from personnel entering or being present during operation of the neutron generator. These are the closest spaces on three sides of the sealed room that an individual could dwell for a period of time.

In the design of the simulated geometry there is a 100 cm thick layer of air between the heavy concrete walls and the void, the latter of which was given zero importance in neutron interaction. The dose and fluence at locations D and E was expected to be primarily caused by neutron particles that penetrate the walls. It is unlikely that many neutrons would exit the maze and scatter in air around corners to contribute scores at the distant tallies. This assumption was not made for location B, since it is plausible that neutrons could scatter from the wall adjacent to location A.

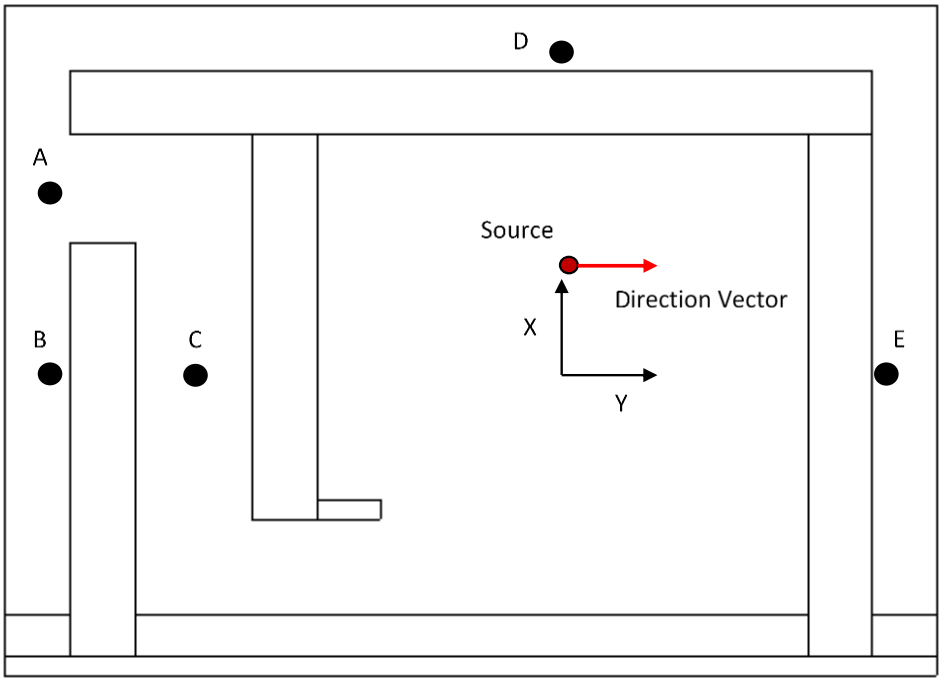

Figure 16: Detector Tally Locations

Table 5: Detector Tally Locations

Tally	X - position	Y - position	Z - position (from floor)
A	302.5	-762.5	120
B	0.0	-762.5	120
C	0.0	-567.5	120
D	492.5	0.0	120
E	0.0	482.5	120

It was discovered early in the simulations that tallies B, D, and E, were not going to reach convergence without a variance reduction technique. The large and complex geometry of the facility requires the generation of many particles before a tally reaches a statistically acceptable mean value. Additionally these tally locations are heavily shielded, resulting in many particles failing to reach the detector tallies. This causes an increase in the minimum number of histories required to attain a reliable result. In contrast, tallies A and C required much fewer histories due to large score contributions from scattered particles.

To remedy this problem it was decided to implement the weight-window generator function. The weight-window generator estimates the importances of space-energy regions. The space-energy weight window parameters are then calculated inversely proportional to the importances [26]. The cell–based generator estimates the average importance of a cell. If the cells are too large the importance variation inside the cell will be large and the average importance will not represent the cell. Inadequate geometry specification also occurs with large importance differences between adjacent cells. The WWG card causes the optimum importance function and parameters for tally X to be generated.

The format of the weight-window parameter card, WWP, is stipulated in the MCNP manual as follows [26]:

WWP:n WUPN WSURVN MXSPLN MWHERE SWITCHN MTIME WNORM ETSPLT

The WWP card generated for tallies B, D, and E, was:

wwp:n 5 3 5 0 0

The interpretation of this is:

- the weight windows are for neutrons
- If a particle weight goes above 5 times the lower weight bound, the particle will be split
- If a particle survived the Russian roulette game, its weight becomes the minimum of either 3 times the lower weight bound, or, 5 times the particle weight
- No particle will be split more than 5 for 1 or be rouletted more than 1 in 5
- The particles weight is checked at surfaces and collisions
- The lower weight bounds are taken from the wwn card

The format of the cell-based weight-window bounds card, WWN, is stipulated in the MCNP manual as follows:

WWNi:n wi1 wi2 ... wij ... wiJ

The card specifies the lower weight bound of the space and energy dependent weight-windows in cells. While space-dependent windows were generated in all cases only a single energy

interval, i, was established corresponding to the energy limits of the simulation. If the bound for a cell, wj, in the wwn card is less than zero, then any particle entering is killed. If the bound is greater, then the particles are dealt with according to parameters on the wwp card. If the bound is zero the weight-window game is turned off and the weight cut-off game is turned on with a 1-for-2 roulette limit [26].

In a simulation to calculate the fluence and dose at a distant tally, the cell representing the wall between the tally location and the source would be split into ten equal portions roughly perpendicular to the shortest particle trajectory. For example, a weight-window run for tally D would involve splitting the adjacent wall along the X-direction; the X coordinate being vertical in these scenarios. Tally B was an exception in that it required two wall cells to be split between it and the source for convergence to occur. Once the window weights and cut-offs were generated, they were pasted into the input file in place of the cell importance's card. The number of histories required to generate accurate weight windows, for tallies D and E, was observed to be approximately 1.5E+08. For tally B, the number of histories required was on the order of 5.0E+08. A short generation time would cause the tally not to sample unlikely events, resulting in sudden increases in relative error and variance-of-variance values throughout the simulation.

The type of tally used at all locations was the F5 point detector. A point detector is a deterministic estimate of the flux at a point in space, from the perspective of the current event [26]. Contributions to the point detector tally are made at source and collision events throughout the random walk of a particle. The score of the tally is given by:

$$F5 = \frac{W \cdot p(\Omega_p) e^{-\lambda}}{R^2} \tag{22}$$

Where:

W = particle weight

R = distance to detector from a source or collision event along Ω_p

λ = total number of mean free paths from particle location to detector

$p(\Omega_p)$ = probability density function for scattering or starting in the direction Ω_p towards the point detector

If assuming azimuthal symmetry, as is done in MCNP, then the previous equation simplifies to:

$$F5 = W\frac{p(\mu)}{2\pi R^2}e^{-\lambda} = W\frac{p(\mu)}{2\pi R^2}e^{-\int_0^R -\Sigma_t(s)ds} \tag{23}$$

Where:

$p(\mu)$ = probability density function for scattering or starting about the cosine of the polar angle, μ, towards the detector

$\Sigma_t(s)$ = total macroscopic cross section at a distance, s, from the source or collision point along Ω_p

A point detector tally is known as a next-event estimator because it is a tally of the flux at a point as if the next event resulted in a particle trajectory directly to the detector point without further interaction. A contribution to the point detector is made at every source or collision event. The $e^{-\lambda}$ term accounts for attenuation between the current event and the detector. The $1/2\pi R^2$ term accounts for the solid angle. The $p(\mu)$ term accounts for the probability of scattering toward the detector instead of the direction selected in the random walk. Each contribution to the detector can be thought of as the transport of a pseudo-particle to the detector [26].

If the R^2 term in the denominator of the above equation approaches zero, if a source or collision event occurs near the detector point, the detected flux approaches infinity. The result is still valid, but convergence is reached more slowly [26]. If the detector is not in a source or scattering medium then this is not likely to cause an issue. If there are many scattering events near the detector an average flux region should be specified. This region is defined by a fictitious sphere of radius R_0 surrounding the point detector. If R is specified in centimeters and if $R < R_0$, the point detector estimation inside R is interpreted as the average flux density.

$$\Phi(R < R_0) = W\frac{p(\mu)}{\frac{2}{3}\pi R_0^3}[1 - e^{-\Sigma_t R_0}] \tag{24}$$

A value of R_0 of 1.0 cm was chosen since neutron particles are unlikely to be scattered in air into the detector at close distances.

For each simulation two tallies per location were utilized: one for flux and the other for dose rate. Both are normalized by MCNP to be per source-particle per second. The ICRP-74 ambient dose was calculated using the dose function card with international units. The energy interpolation was completed using a logarithmic scale; the dose is always interpolated linearly.

The location of the source relative to the tallies is shown in Figure 16. Modeling the source with decent accuracy was necessary to achieve the objectives stated in this thesis: determining the fluence and dose rates for three acceleration potentials during operation of the generator. It was stated previously that neutrons resulting from the H^2(d, n)He^3 reaction have an anisotropic angular distribution in the CM, dependent on incident charged deuteron energy. The energy distribution of the neutrons is likewise not uniform. It was decided that the three potentials needed to be within a narrow range near the maximum operating limit to acquire physically meaningful results since neutron yield falls rapidly at lower voltages due to a decreasing cross-section, but not so close that the simulation data would not be discriminable.

The three anisotropic distributions, selected to be simulated, correspond to accelerator potentials of 130 kV, 110 kV, and 90 kV, and were modeled by assuming a thin target of pure isotopic deuterium. This results in a directionally dependent monoenergetic source of neutrons. The differential cross-section and neutron energy data, in the LAB, was generated by the particle interaction code DROSG-2000. The differential cross-sections were generated in increments of 5° and subsequently normalized to unity. The angular distribution is shown graphically in Figure 17, only with the values displayed normalized to the mean. The neutron energies were also generated in 5° increments, shown in Figure 18. A sample of the input code for the sources is given in the appendices. An isotropic source approximation was likewise simulated for comparison.

It was decided that the three anisotropic sources would be geometrically modeled as a point source. This is partly because the dimensions of the target are minuscule in comparison to that of the tally distances and because the ion beam does not bombard the target uniformly. On the other hand, the isotropic source was modeled as a thin cylinder to represent the idealized scenario. The source location and orientation will be identical for all runs, as given in Table 6.

The Monte Carlo model does not account for the accelerator housing and electrical components in which the target is located. In reality this would contribute to a measure of inelastic scattering of the fast source neutrons, which in this case is not represented.

Table 6: Source Location and Dimensions

Source	X, Y, Z - position	Direction Vector	Radius	Extent
Isotropic Disc	164.14, 11.5, 76.9	+Y	5.0 cm	-0.15 cm to 0.15 cm
Anisotropic Point E(D) = 130 keV	164.14, 11.5, 76.9	+Y		
Anisotropic Point E(D) = 110 keV	164.14, 11.5, 76.9	+Y		
Anisotropic Point E(d) = 90 keV	164.14, 11.5, 76.9	+Y		

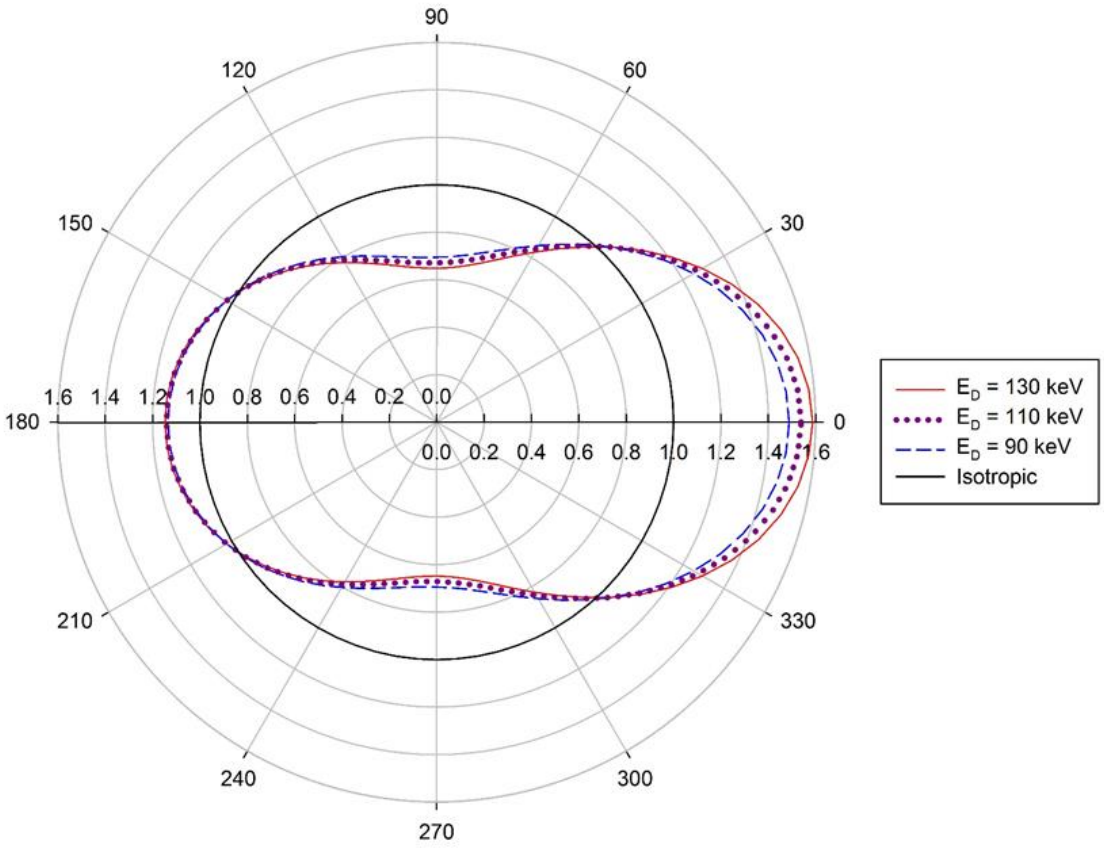

Figure 17: Angular Distribution of Neutrons from ^{2}H (d, n) ^{3}He Reaction in LAB

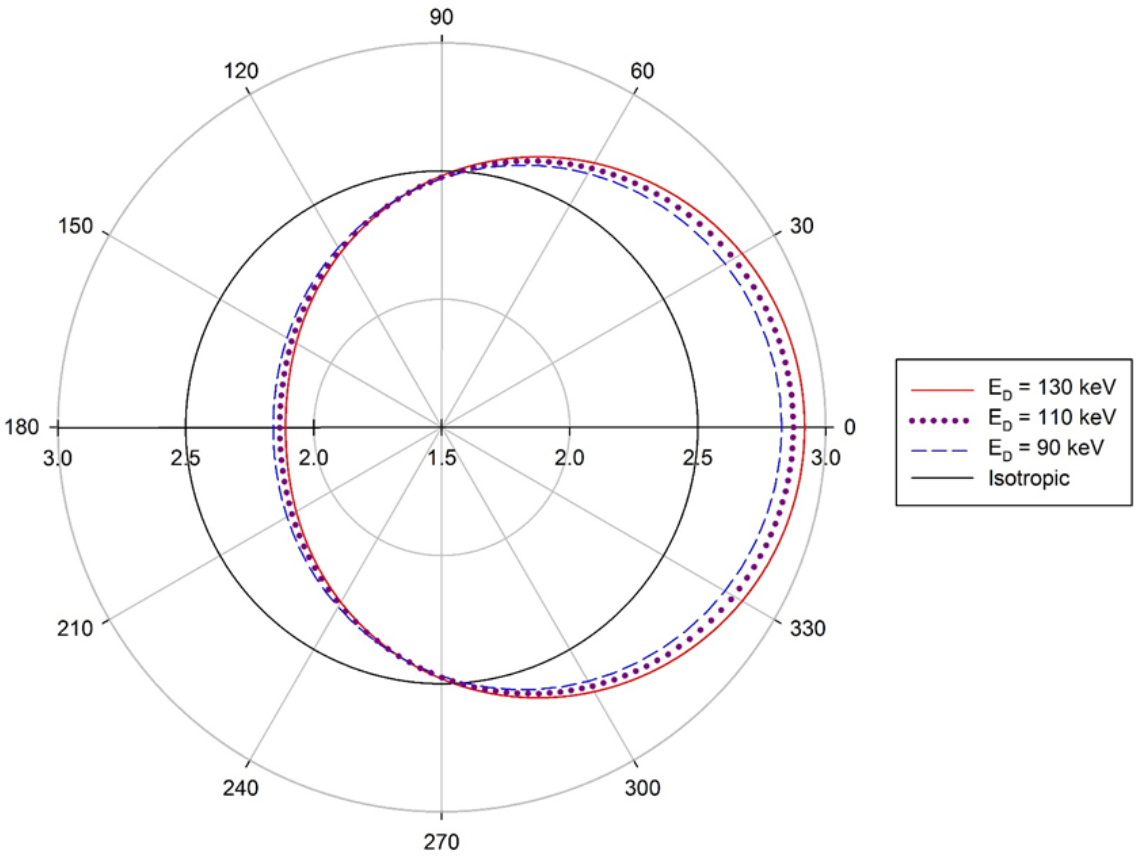

Figure 18: Energy Distribution of Neutrons from ^{2}H (d, n) ^{3}He Reaction in LAB

2.3 Experimental Investigation

The purpose of the experimental portion of this thesis was to ascertain the intensity of the P-385 neutron generator. This was accomplished by operating the generator with an accelerator potential of 130 kV, congruent with the angular and energy distributions of the simulated source.

2.3.1. Neutron Generator Description

The neutron generator installed in the facility is a Thermo-Scientific P-385 model. Operating specifications are shown in Table 7 and dimensions in Table 8.

Table 7: P-385 Operational Parameters [27]

Parameter	Value
Input Voltage	24 VDC +/- 10% @ 5 A 100 VAC - 240 VAC 50 Hz - 60 Hz
Power	Less than 75 W
Neutron Yield, nominal	3.0E+08 neutrons/second, D-T mode
Neutron Yield, maximum	5.0E+08 neutrons/second, D-T mode
Neutron Energy	14.1 MeV D-T 2.5 MeV D-D
Max. Accelerator Voltage	130 kV
Frequency	250 Hz – 20 kHz
Duty Cycle	5% - 100%,
Minimum Pulse Width	5 microseconds
Pulse Rise/Fall Time	<1.5 / 0.5 microseconds
Lifetime	1500 hours at nominal output

Table 8: P-385 Dimensions [27]

Dimension	Value
Mass	12 kg
Accelerator Head Diameter	10.2 cm
Accelerator Head Length	68.6 cm
Target Plane to End Cap Distance	11.4 cm

The above yield data is valid only for D-T reactions and does not apply if the target was preloaded with deuterium for D-D operation. It is possible to estimate the yield by comparing the average

cross-sections. The neutron producing D-T reaction has a yield about two orders of magnitude greater than the equivalent D-D reaction. As will be shown later in the results section, when the experimental doses read from the bubble detectors are normalized to the simulated dose-per-source-particle tally values, this is a reasonably valid approximation.

The outgoing neutron energy values published can be interpreted as an average over all solid angle. In the laboratory reference frame the neutron energy will depend on the accelerated deuteron energy. This is simply the acceleration potential, V, multiplied by the charge of the particle. Since a deuteron will have a magnitude of 1 elementary charge, e, it will gain kinetic energy equal to eV. At 130 kV accelerator potential, the emitted neutrons will have an energy of approximately 2.9 MeV at 0°, 2.5 MeV at 90°, and 2.1 MeV at 180°.

2.3.2. Experimental Setup

The detector utilized in the experiment is a medium sensitivity BD-PND bubble dosimeter. This detector was required to quantify dose predominantly caused by an essentially mono-energetic source of fast neutrons. Although dose incurred by the scattered component was invariably also a factor in this experimental setup. Through a private communication, it was revealed that these dosimeters are calibrated by BTI using an Am-Be source of 1.13E+07 neutrons per second intensity. This is accomplished by using an average dose per unit fluence, calculated by convoluting the source spectrum to the NCRP-38 dose equivalent curve, in conjunction with the source strength. This yields known equivalent dose rates at set distances that is used to calibrate the detectors.

The principle application of bubble detectors is in the measurement of fast neutron dose equivalent. Ideally the detector would produce one bubble per unit neutron dose, independent of incident energy [28]. The number of bubbles would then be a measure of the total dose without knowledge of the neutron spectrum. This type of behavior requires that the detection efficiency as a function of neutron energy match the curve of dose delivered by neutrons as a function of energy.

Dose rate data for three proximate locations surrounding the neutron generator were gathered using BD-PND bubble dosimeters referred to as G,F and H. Figure 19 shows the dosimeter placement with respect to the generator, while Figure 20 shows the position of the generator in the room. Their vertical placement coincided with the horizontal plane of the central axis of the target at a distance of 103 cm from the floor.

The operating parameters of the generator when the readings were taken were: accelerator potential, 130 kV; beam current, 70 µA. These are the upper operational limits for this unit. As stated previously one of the particle transport simulations corresponds to neutrons generated from deuterons accelerated to 130 keV.

Figure 19: Locations of Bubble Detectors, YX-Plane

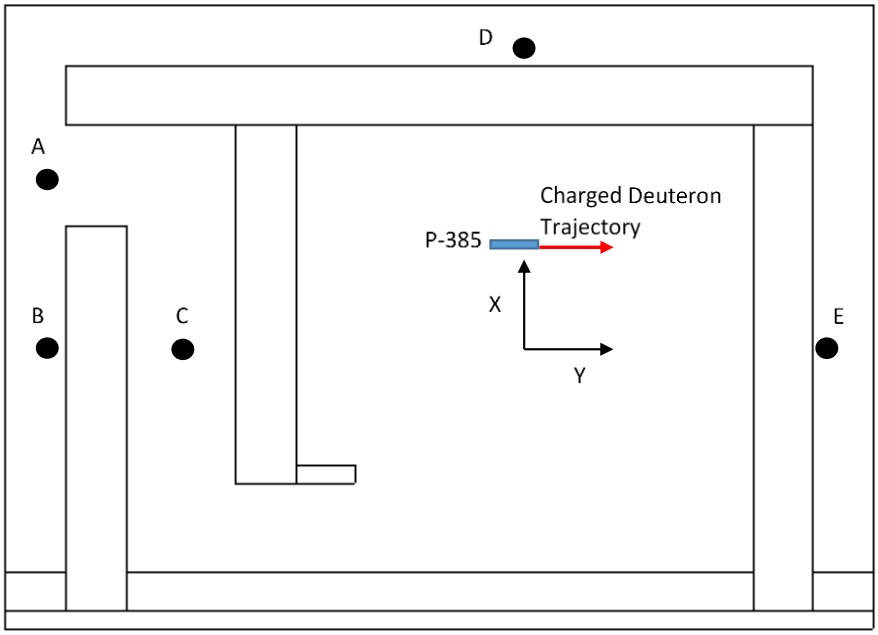

Figure 20: Position of P-385 Generator in Facility

Photos of the neutron generator and experimental setup in the ERC basement are shown in Figure 21 through Figure 23.

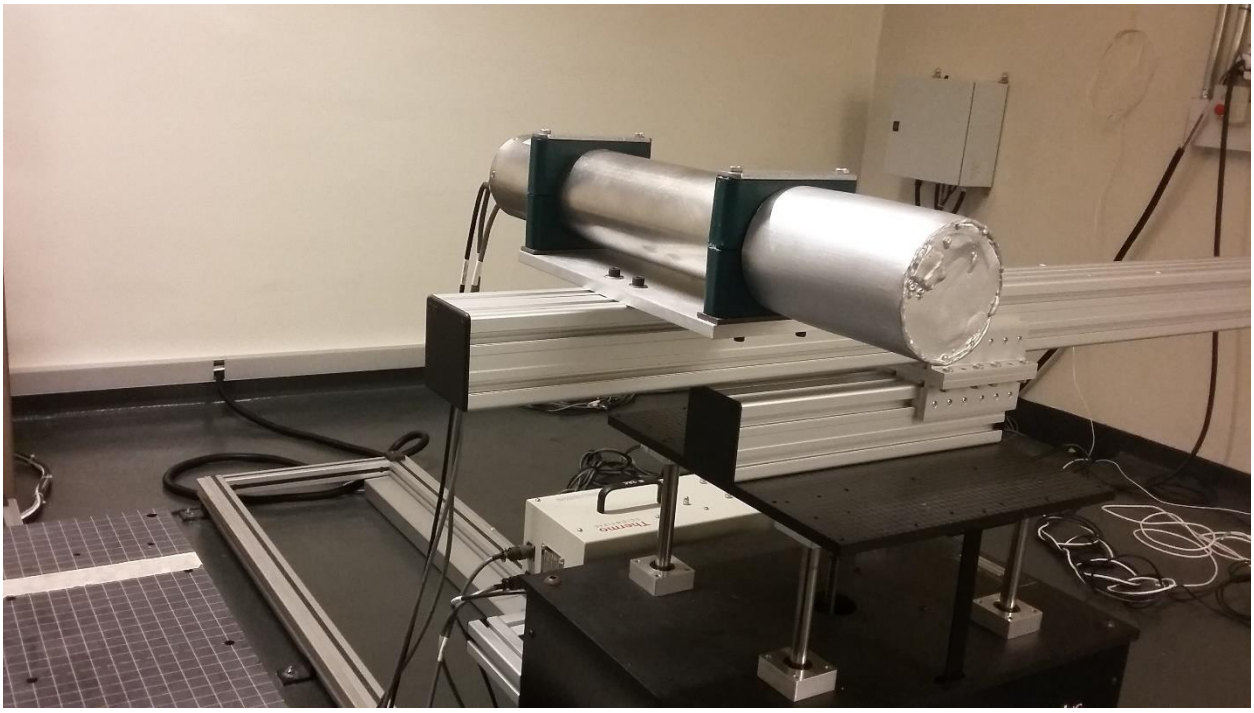

Figure 21: P-385 Neutron Generator

Figure 22: Experimental Setup 1

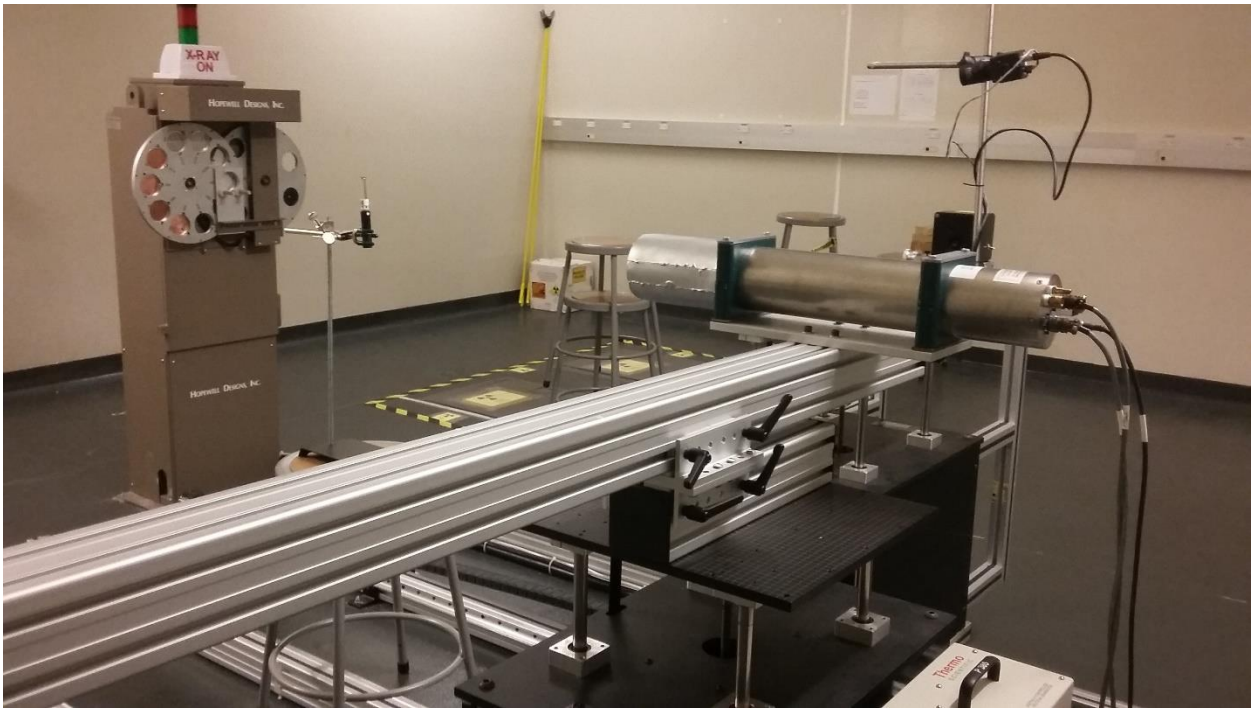

Figure 23: Experimental Setup 2

2.4. Source Intensity and Total Dose rate

Experimental dose rate data of neutron dosimeters in the neutron generating facility was required to determine the neutron intensity emitted from the P-385 generator. Since the nominal intensity of the generator operating in the deuterium-deuterium configuration is not published by the manufacturer explicitly, it was necessary to replicate the scenario in MCNP and simulate the dose recorded by the dosimeters at the equivalent locations. By calculating the quotient of the experimental dose rate with the simulated dose rate per source-particle, it is possible to approximately estimate of the intensity of the neutron generator.

$$I(n) = \frac{[Sv \cdot hr^{-1}]_{exp}}{\left[Sv \cdot hr^{-1} / SP \cdot s^{-1}\right]_{sim}} = SP \cdot s^{-1} \tag{25}$$

The MCNP simulation that was run to calculate source intensity used detector-type tallies modified using the dose-function card to collect dose rate data, as was done with the tally points in surrounding locations. Unlike the surrounding locations which used the ICRP-74 option in the DF card, the tallies corresponding to experimental location used the NCRP-38 function to reflect the actual calibration of the dosimeters. The lower energy bin limit of the detector tallies were setup to collect dose rate data for incident neutrons corresponding to the detection threshold of the BD-PND dosimeter; stated as 200 keV [29]. The upper bin was set to a maximum of 3.0 MeV, corresponding approximately with the maximum energy of the source.

If the simulated geometry and materials are accurate with respect to the actual facility, and barring abnormalities, then it was expected that calculations for all three data points would yield similar source intensities. Once the intensity is calculated the total ambient dose rate at the tally locations can be calculated.

To determine whether the variations in the per-source-particle values calculated by MCNP have a substantial effect on total values, it is necessary, to somehow, scale the source intensity to different charged deuteron energies when operating with acceleration potentials of 110 kV and 90 kV. The P-385 operations manual states that the yield is proportional to the voltage to the 3/2

power. Figure 24 displays the ENDF.VII.1 integrated (d, n) cross sections as a function of deuteron energy, which roughly follows this trend. The intensity was expected to be approximately proportional to the reaction cross section.

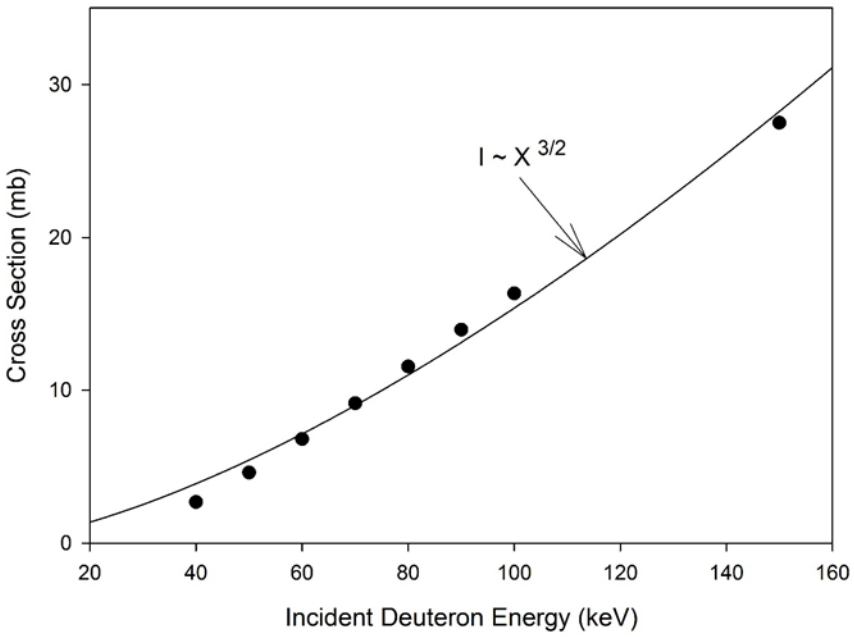

Figure 24: ^{2}H (d, n) ^{3}He Reaction Cross Section

For the purpose of this thesis, the dose rate will be calculated in a linear fashion as follows:

$$\dot{D} = I_{E(d)=130\ keV} \cdot \frac{\sigma_{E(d)=i}}{\sigma_{E(d)=130\ keV}} \cdot \dot{d} \tag{26}$$

$$where: \quad I_{E(d)=130\ keV} = intensity\ of\ the\ generator\ at\ experimental\ conditions$$

$$\dot{d} = simulated\ dose\ rate\ per\ source\ particle = \frac{Sv.hr^{-1}}{SP.s^{-1}}$$

The above method implies several assumptions regarding the neutron generator:

- The intensity is proportional to the cross-section of the neutron-producing reaction
- The accelerated deuteron ions are monatomic and interact with a thin target of deuterium
- The neutron yield is mono-energetic for a specific finite solid angle

Chapter 3: Results and Discussion

3.1. Monte Carlo Simulation Results

The data calculated from the Monte Carlo simulations include flux per source-particle, and the ICRP-74 ambient dose rate per source-particle, for the aforementioned main tally locations: A, B, C, D, and E. The mean values of the two parameters summed over all incident neutron energy groups will be given for the isotropic source and the three anisotropically modelled sources. The latter three sources are referenced to by the potential applied to the charged deuteron to generate the particular neutron distribution: 130 kV, 110 kV, and 90 kV. The results will be presented in graphical format, with bars representing the calculated statistical error for each simulation.

The neutron spectra and dose rate distribution will be plotted for the isotropic and 130 kV sources. The selection of only one anisotropic source is due to similar spectra, which would make discrimination difficult. The values on the abscissa of the spectra are the upper limits of the energy bins generated by MCNP, of which there are 25. The lowest being 1.0E-10 MeV and the highest 3.0 MeV, with intermediate values established through logarithmic interpolation. The neutron energy spectra is formatted with a linearly scaled ordinate, while the dose rate distribution has a logarithmically scaled ordinate. This was chosen to accommodate the behaviour of the flux-to-dose conversion function. One could convert the flux spectra into dose rates with the appropriate function, but it was decided that both would be included to efficiently present the data. The results presented are, in general, self-explanatory. The discussion will be focused on deviations of the simulated values from expectations.

3.1.1 Simulation Results: Location A

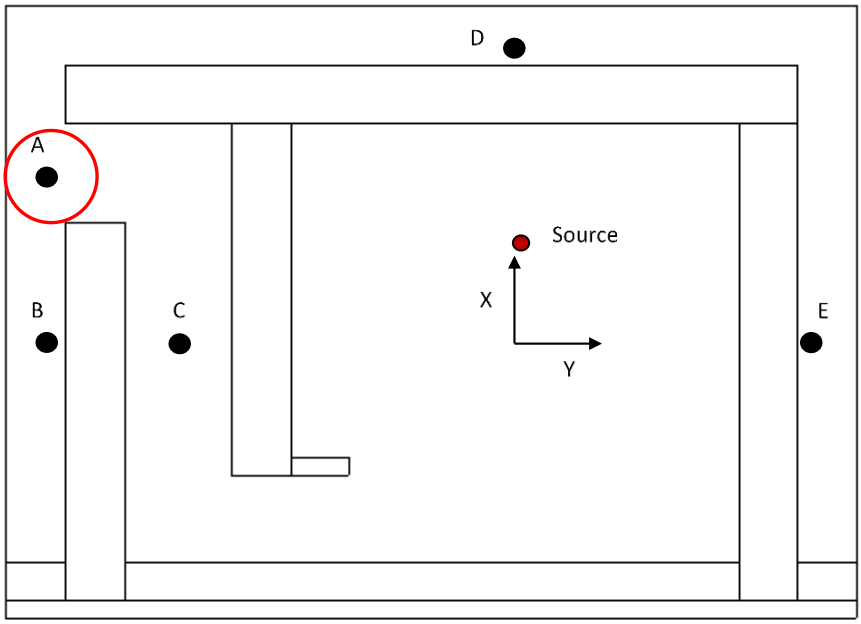

Figure 25: Tally A Location

The simulated flux per source-particle at location A, Figure 26, was roughly equal for the three anisotropic sources and greater for the isotropic source. Hypothesizing what the flux value would be using only the source-neutron angular and energy distribution for reference would likely lead one to conclude that the 130 kV source would cause the lowest fluence rate at location A, followed by the 110 kV, 90 kV, and isotropic sources. The mean values calculated by MCNP do not explicitly support this conjecture. It was observable that the 110 kV source did indeed deliver a lesser flux than 90 kV source, which would support the previous supposition. However, both are lower than the 130 kV source. The range of values that the tallies could ultimately converge to, when accounting for statistical error, conceivably indicates that they could take on any order.

The simulated flux with the isotropic disc approximation was greater than the other source models since every initial flight direction is equally probable. The other three sources have an angular distribution that is not favourable for producing neutrons near angles of 90° and 270° relative to the charged deuteron trajectory.

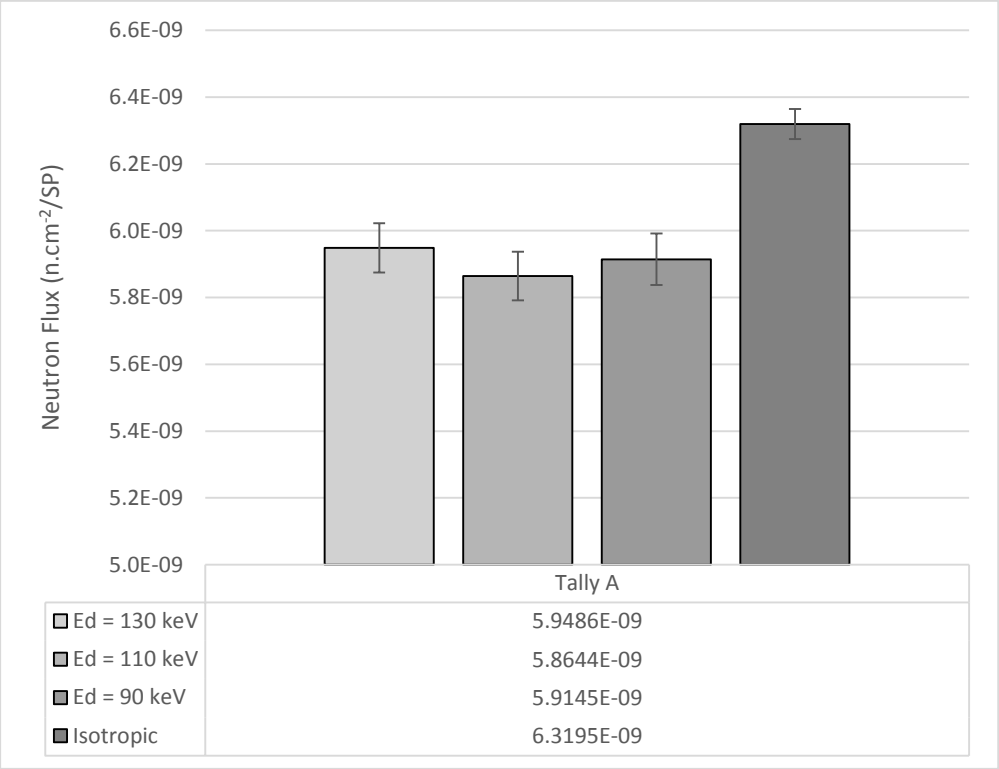

Figure 26: Tally A: Neutron Flux

The spectrum comparing the flux per energy group is shown in Figure 27. As was stated previously, only the 130 kV and isotropically modelled sources will be compared. The greatest neutron flux with both sources was present at incident energies between 0.0416 eV and 0.114 eV. This indicates that the neutrons had to undergo many scattering events to slow down from 2.5-3.0 MeV. There is an observable trend in this spectrum where at higher energies relative to this peak, incident neutron flux appears to be inversely proportional to the incident neutron energy. A noticeable feature of the spectra is the relative flux of the highest energy group. This is likely attributable to the equal distribution of neutrons for the isotropic source, while the 130 kV source produces neutrons most intensely at emission angles nearest the trajectory of the accelerated ion beam in the generator.

The sharp decrease in flux for lower energy groups below the peak is attributable to the propensity for neutron absorptions at low energies; the predominant interaction of neutrons with matter transitions from elastic scattering to absorption.

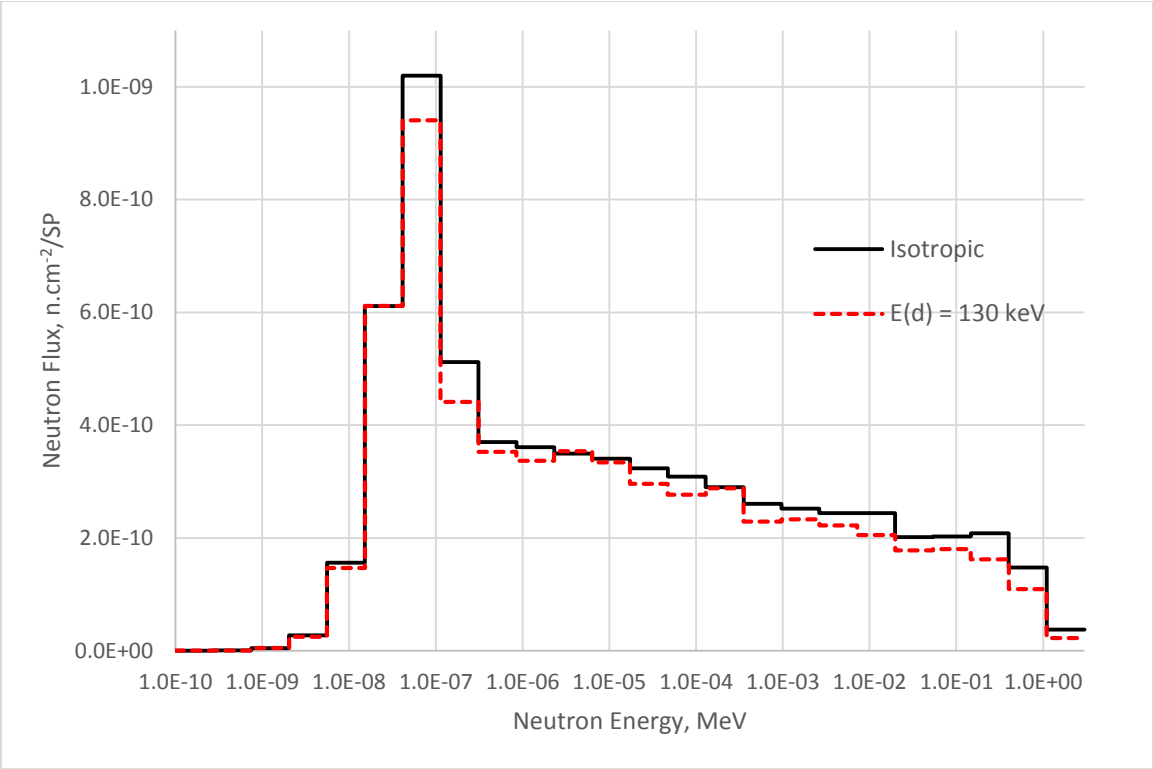

Figure 27: Tally A, Neutron Spectra

The dose rate, Figure 28, follows a similar trend as seen with the flux in Figure 26. The anisotropic sources incur a lower dose rate at location A than the isotropic source; the former three share roughly similar magnitudes. The mean value simulated with the 90 kV source is shown to be slightly higher than with the 130 kV and 110 kV sources, which is in contrast to the flux calculations. The actual comparability is limited, however, due to the overlap of statistical error.

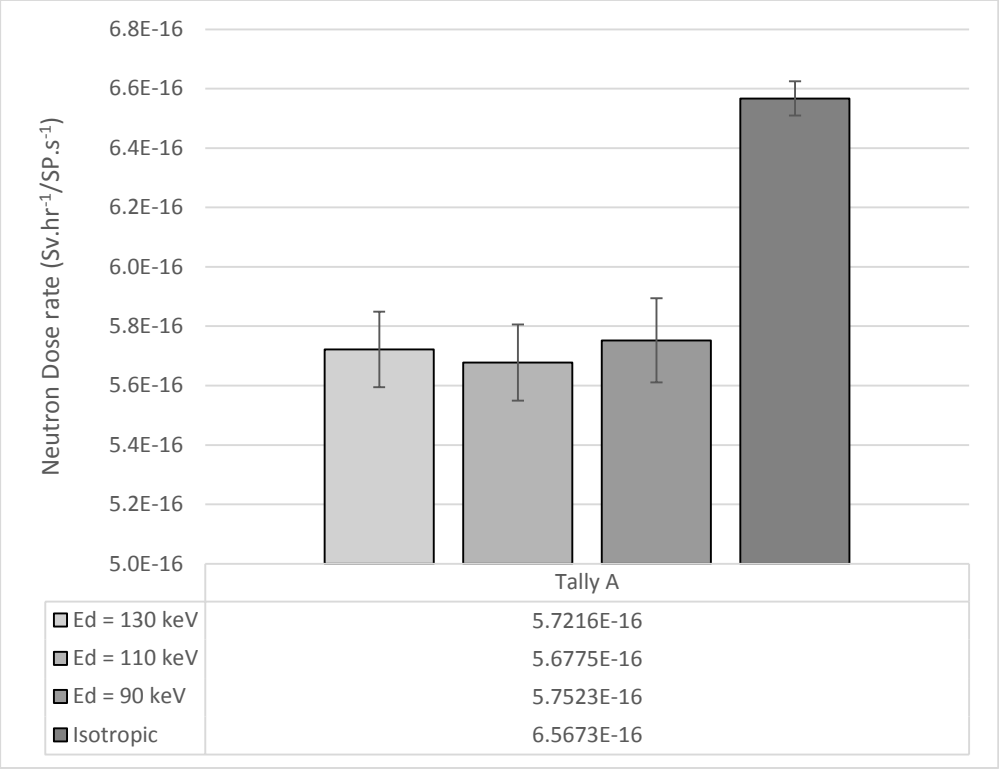

Figure 28: Tally A, ICRP-74 Ambient Neutron Dose Rate

Figure 29 displays the dose rate attributed to particular incident neutron energies. The peak between 0.0416 and 0.114 eV is still discernible, as is the decreasing contribution of neutrons below this energy bin. The dose rate incurred by the higher energy groups is very high when compared to their flux contribution. This is of course a consequence of the neutron energy-dose conversion, where at higher energies neutrons deliver a greater dose relative to their energy than slower neutrons. The main difference in ambient dose rate incurred by the anisotropic and isotropic sources is due to neutrons in the higher-energy groups, above 147 keV.

As the isotropic source simulation overestimated the fluence and corresponding dose at this location, there is minimal consequence in using this approximation for operational purposes. Although the above statement is true only if the neutron generator maintains its current position and orientation.

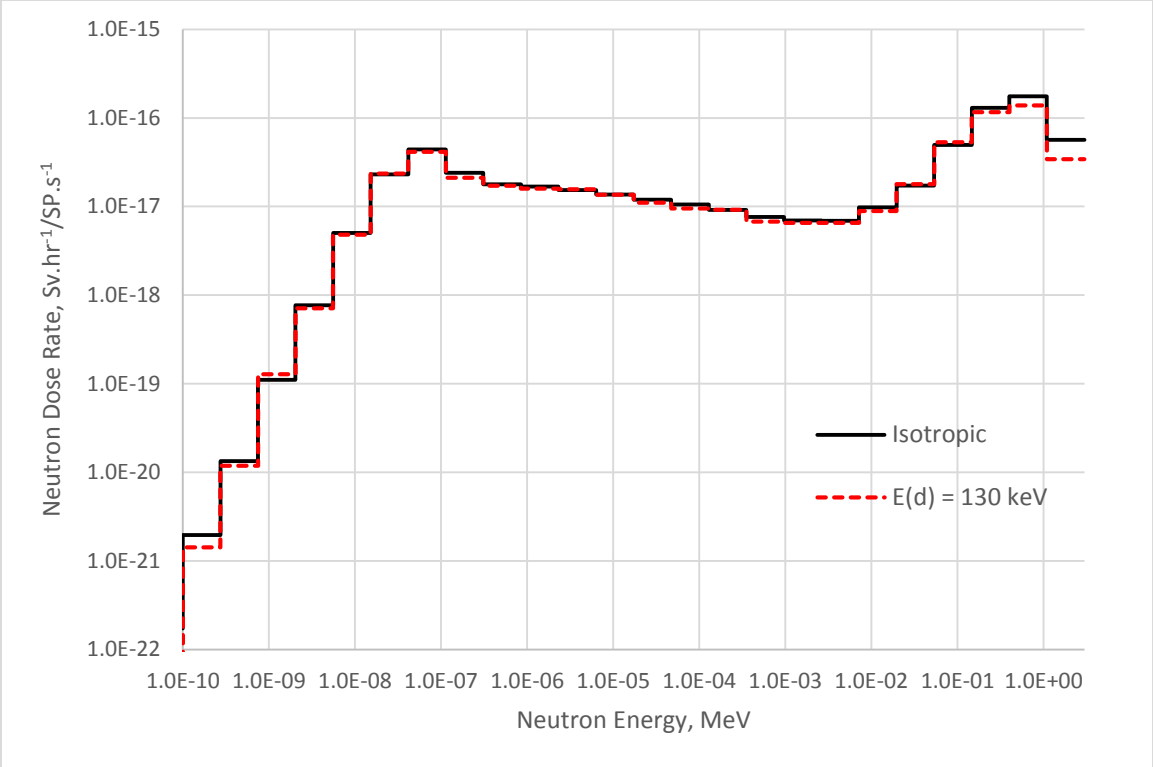

Figure 29: Tally A Neutron Dose Rate Distribution

3.1.2 Simulation Results: Location B

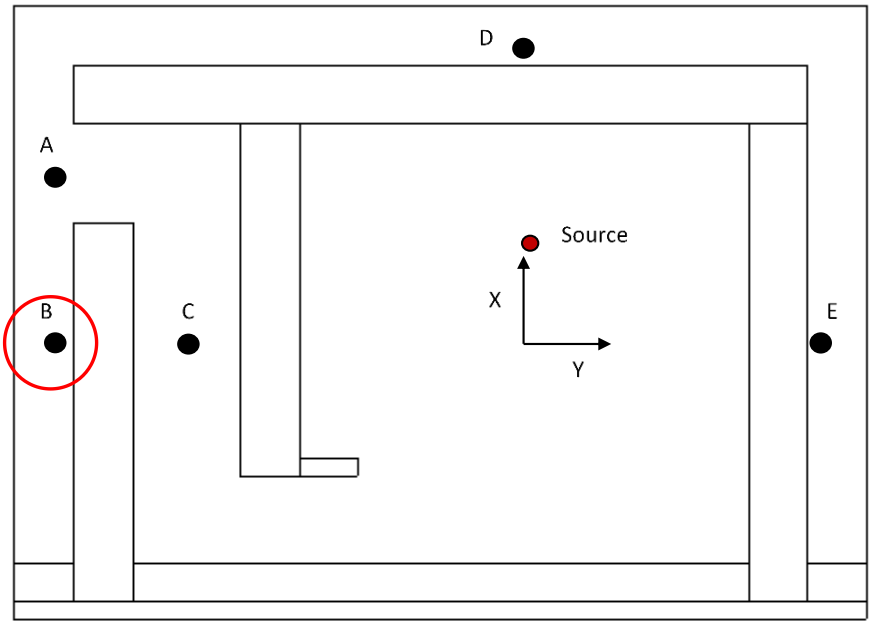

Figure 30: Tally B Location

The Monte Carlo simulation for location B was the most difficult in terms of maintaining a low relative error and an acceptable variance-of-variance. For this reason, the spectra for this location have energy bins with a somewhat greater error than the other tallies.

The flux at location B is shown in Figure 31 for the four source simulations. This location was unique in the facility in that source neutrons must scatter in the generator room from the source and subsequently penetrate through the wall adjacent to the tally. As such, it was expected and confirmed that the flux would be the lowest of all the locations sampled.

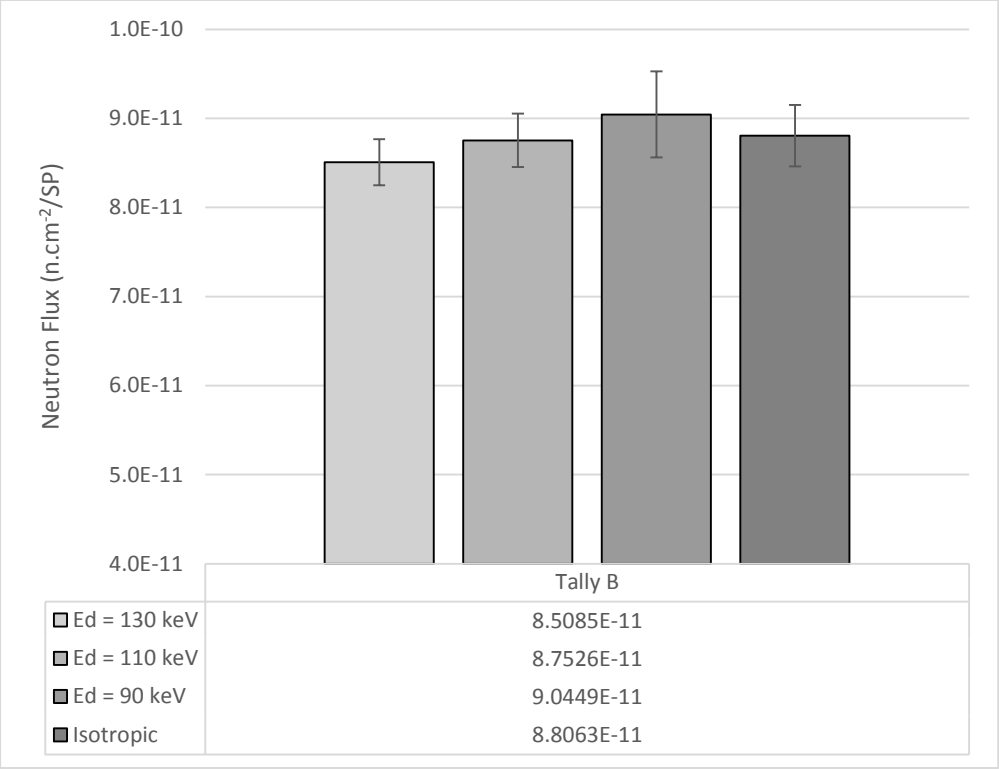

Figure 31: Tally B, Neutron Flux

The flux transmitted from the anisotropic sources were very close to the isotropic source. Noticeably the range of possible values, when taking error into account, overlap. There is an evident trend where flux decreases with increasing deuteron energy. This is likely attributable to the slightly decreasing forward peak in the angular distribution of source neutrons for higher deuteron energies.

Figure 32 compares the neutron energy spectra at location B. The relative intensity in each energy bin is rather similar to that of location A, only with a more pronounced thermal peak between 0.0416 eV and 0.114 eV (low energy neutrons). The 130 kV source appears to cause a larger fluence between 0.0416 eV and 0.311 eV. At higher energies, the isotropic source delivers a greater fluence, particularly in the four highest energy bins, which would indicate that a larger portion of neutrons do not undergo slowing-down processes.

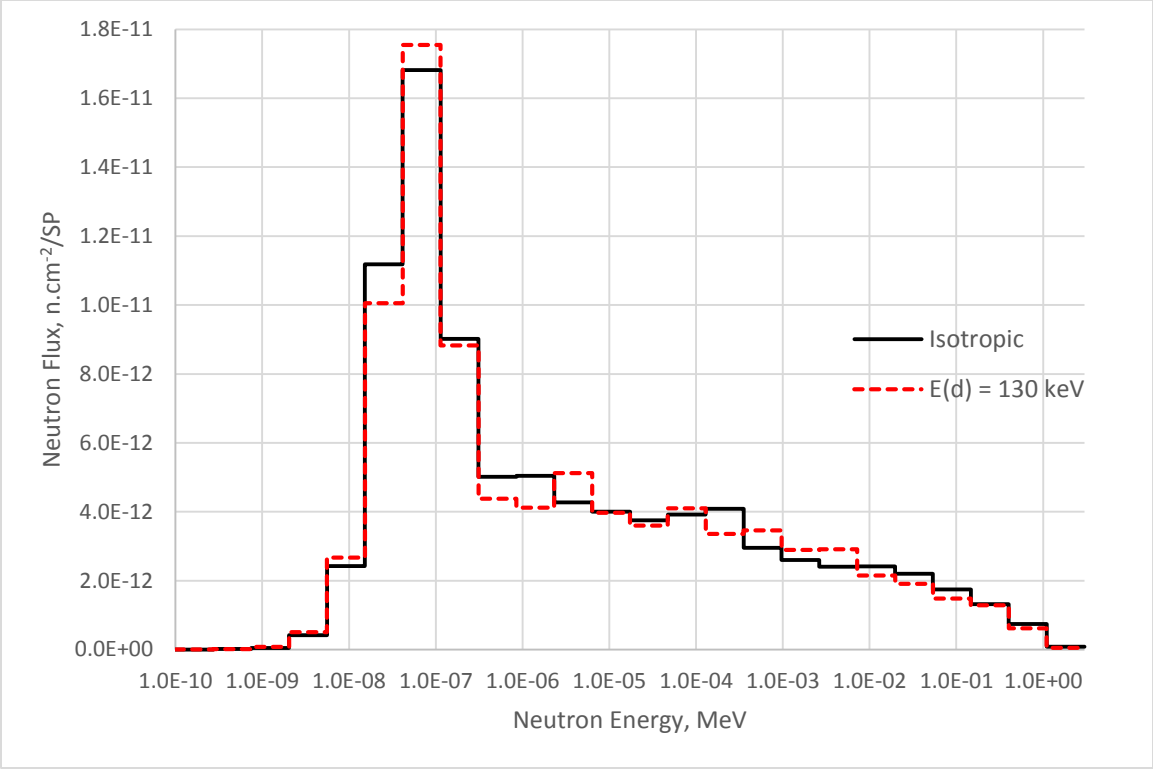

Figure 32: Tally B, Neutron Spectra

The dose rates calculated by MCNP, Figure 33, indicate a correlation with deuteron energy. This was hypothesized since the closest location on the opposite side of the wall, tally C, has a greater proportion of higher energy neutrons, while transmitting only a slightly greater flux. It was reasonable to assume that this would hold true for tally B.

The lowest recorded dose rate was sustained when simulating the 130 kV source. Although the tally point is likely too distant from the source to make any accurate speculations, it is conceivable that the lower energy of source neutrons at 180° caused it to impart a lower dose rate to the detector.

The dose rate is somewhat overestimated when running a simulation using an isotropic source.

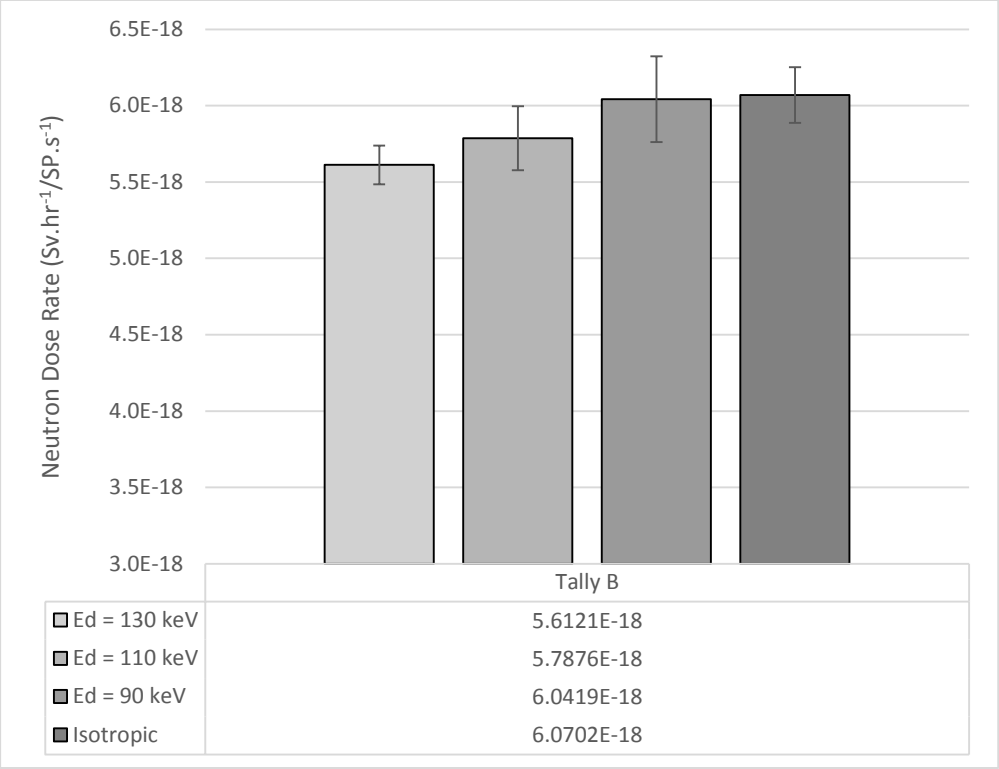

Figure 33: Tally B, ICRP-74 Ambient Neutron Dose Rate

The graph of the dose rate distribution, Figure 34, indicates that despite a dominating thermal peak the energy bins with the largest contribution to ambient dose are between 147 keV and 1.1 MeV. The isotropic source imparts a larger dose rate than the 130 kV source most apparently at energies above 53.8 keV, although this is true for most of the energy bins. The latter source imparts a greater dose rate between 0.0416 eV and 0.311 eV, as is evident in the energy spectrum above.

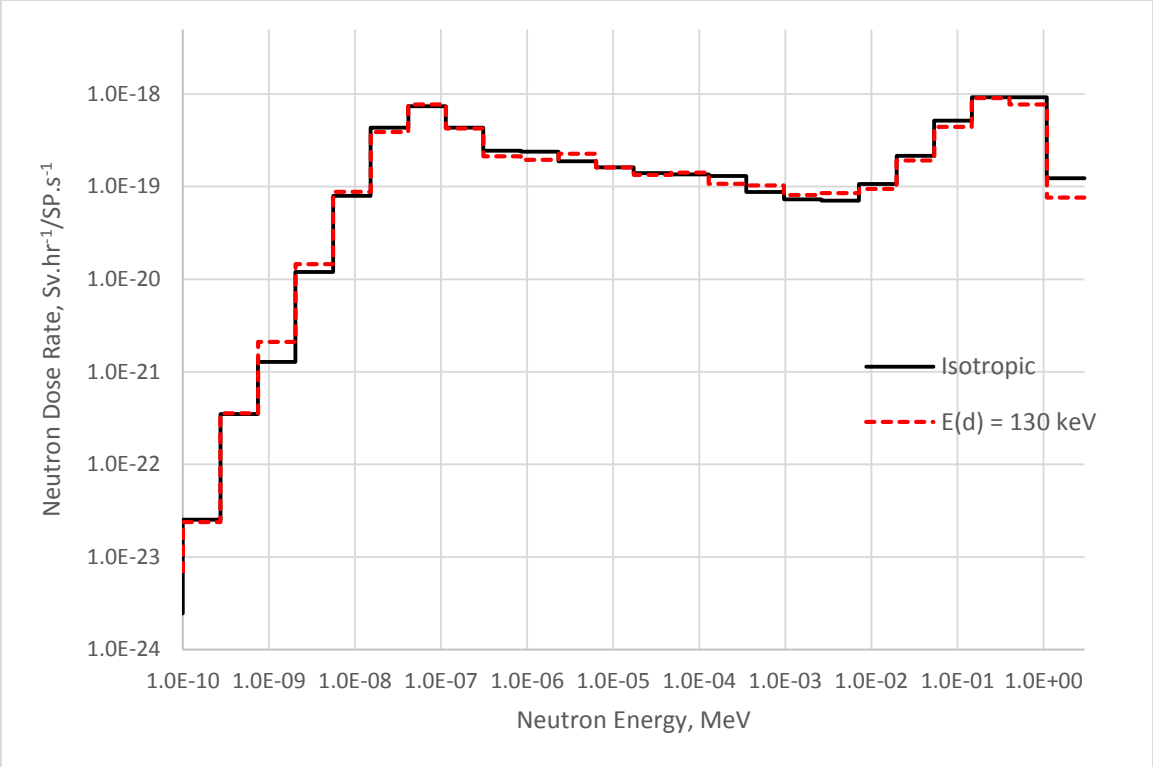

Figure 34: Tally B Neutron Dose Rate Distribution

3.1.3 Simulation Results: Location C

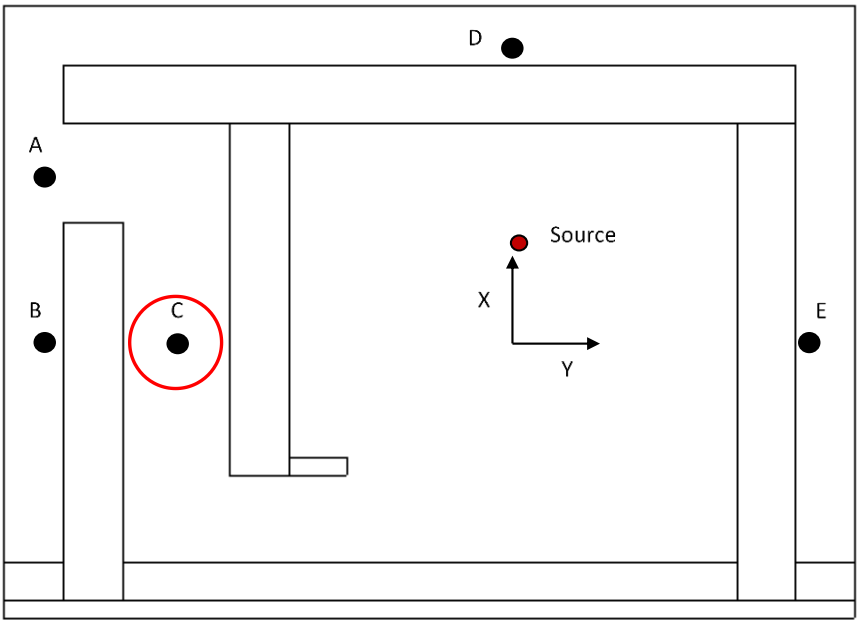

Figure 35: Tally C Location

The flux calculated at location C is summarized in Figure 36. The 130 kV, 110 kV and 90 kV, sources have very similar values. The statistical error is less than with tally A and enables a more accurate comparison, though their does not appear to be a readily identifiable correlation between calculated flux and applied acceleration potential. The simulation involving the isotropic source had a larger flux in comparison, permitting its use as a conservative estimate.

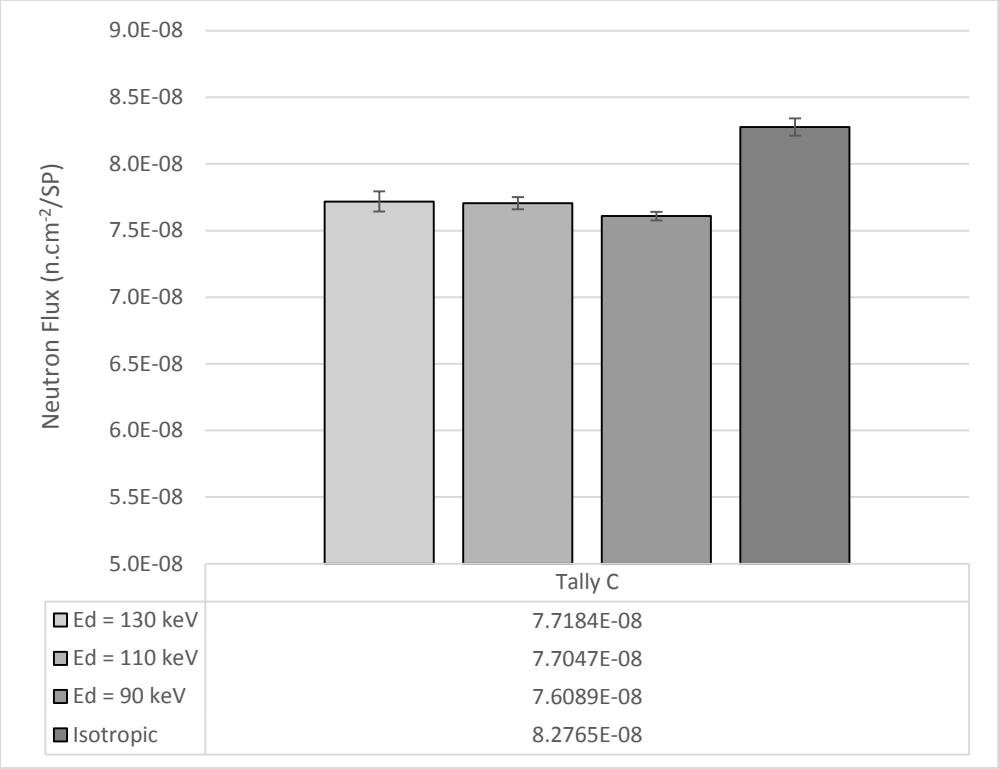

Figure 36: Tally C, Neutron Flux

The energy spectra at location C, Figure 37, is similar to the spectra at location A. Both show a peak between 0.0416 eV and 0.114 eV and an abrupt decrease in contribution by neutrons of lower energies. The primary difference is a greater proportion of higher energy neutrons in the incident flux. This is expected since the tally point is closer to the source than location A, and fewer scattering events are required for particles to reach it from the source.

The difference in fluence between the anisotropically modelled source and the isotropic source, again, is greatest in the higher-energy groups.

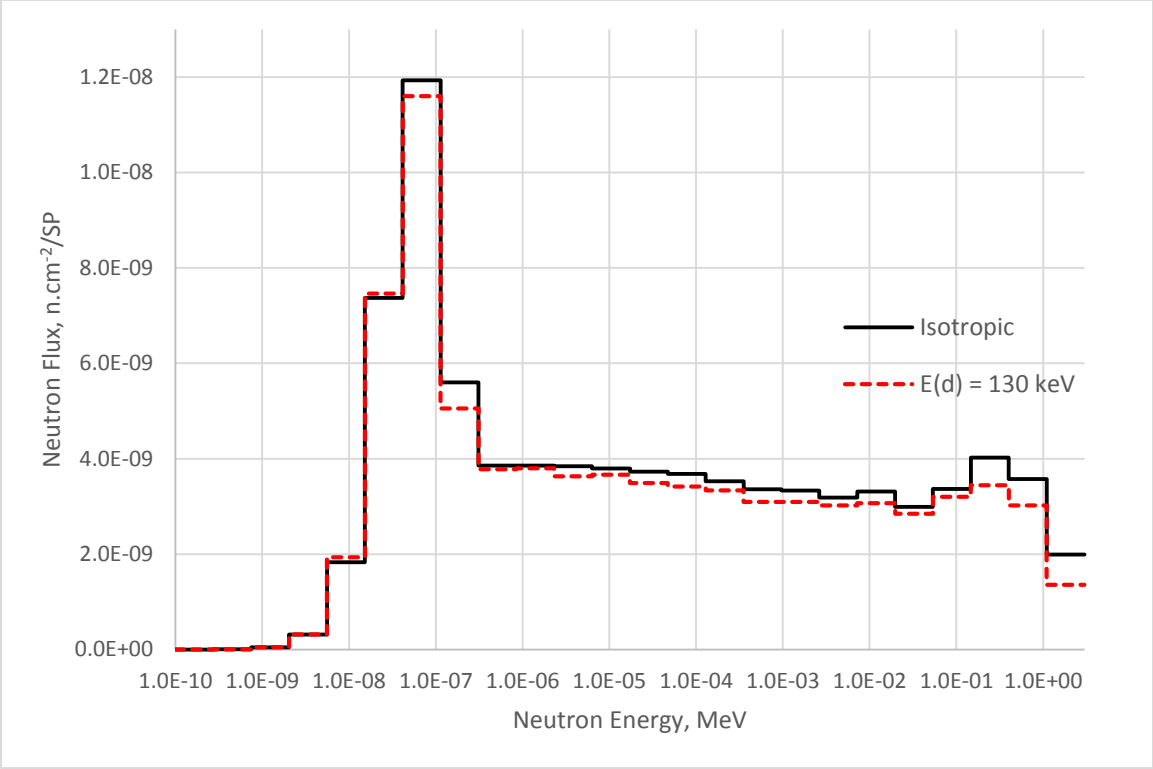

Figure 37: Tally C, Neutron Spectra

The calculated dose rate data for each modelled source, in Figure 38, is consistent with the flux values in Figure 36. The 110 kV source simulation resulted in possibly greater acquired dose rates than with the 130 kV source - both are within relative error of each other - but most likely higher than with the 90 kV source. This was not anticipated since the latter source model, in a non-scattering medium, produces a greater intensity of source neutrons from the rearward emission cone.

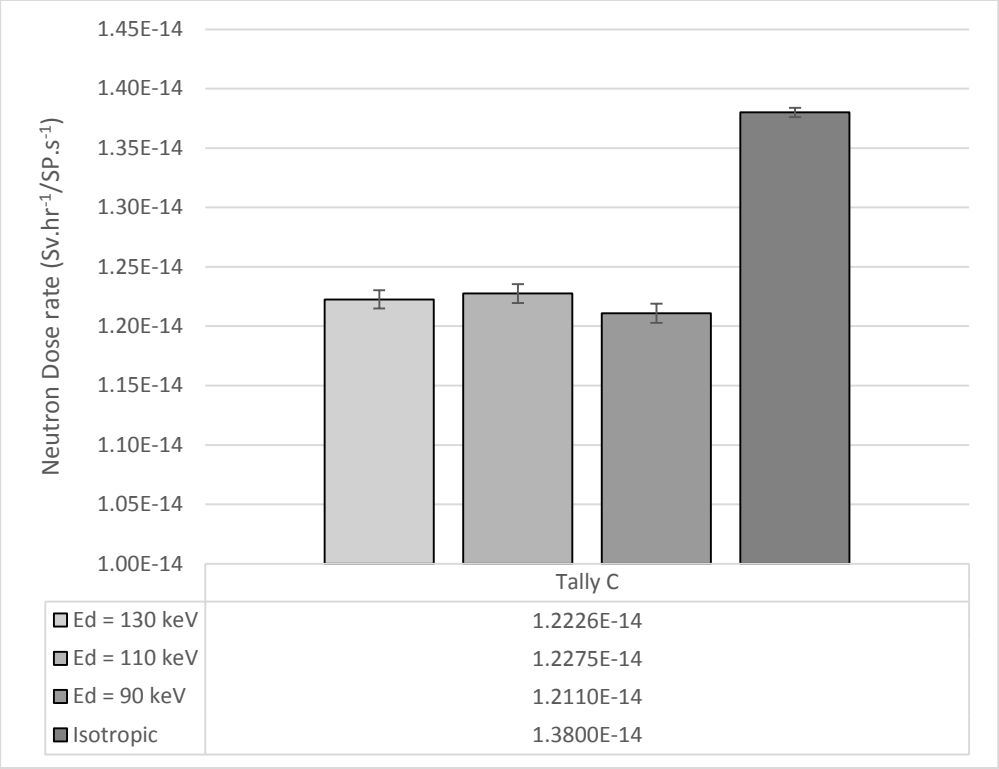

Figure 38: Tally C, ICRP-74 Ambient Neutron Dose Rate

Figure 39 shows that the largest dose rate is caused by the flux of higher-energy neutrons, which is consistent if applying the dose rate function to the flux spectra in Figure 37.

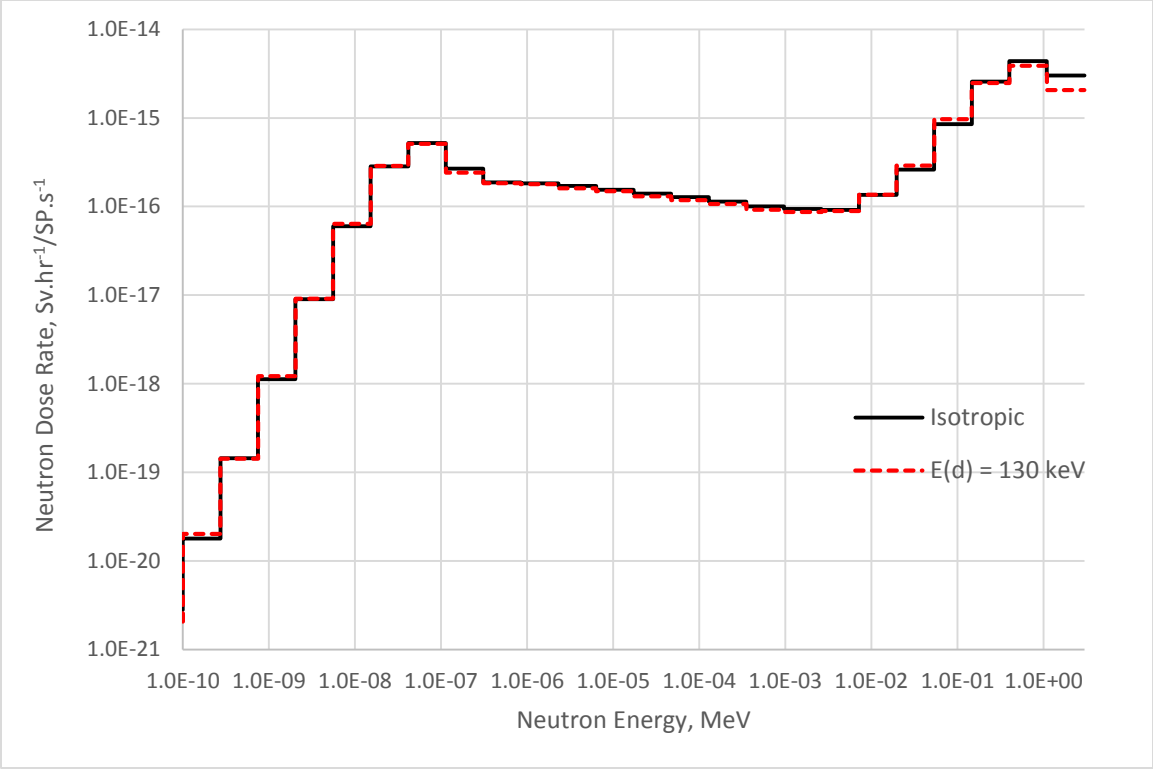

Figure 39: Tally C Neutron Dose Rate Distribution

3.1.4 Simulation Results: Location D

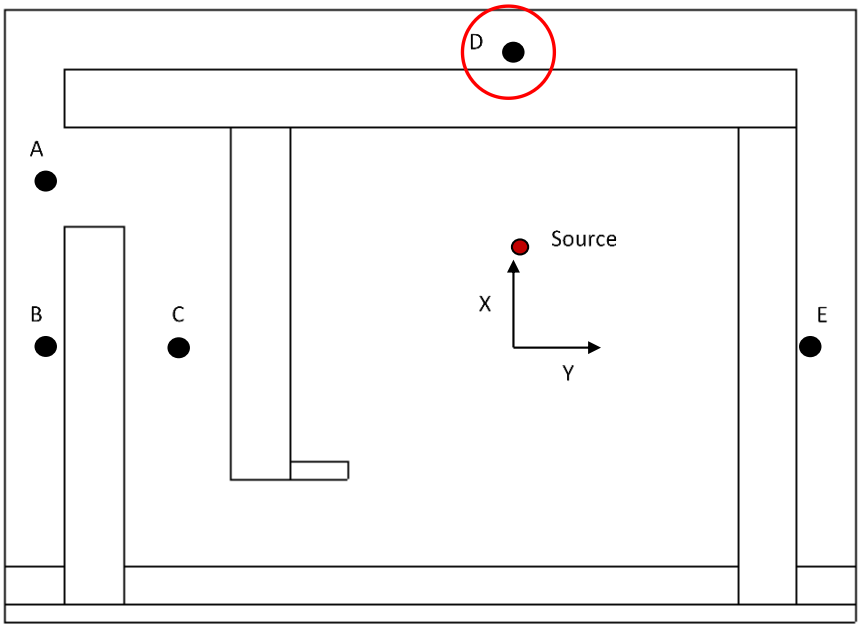

Figure 40: Tally D Location

The simulated flux at location D, Figure 41, show a greater difference between the isotropic and anisotropic source models in comparison to the previously discussed locations. A peculiarity is that the anisotropic sources transmit a greater neutron fluence than the isotropic disc source. This is not readily explainable since the accelerator sources, while generating neutrons of approximately 2.5 MeV at 90°, have a relatively low probability of producing source particles near that angle. It is suspected that as a consequence of modelling the isotropic source as a thin cylinder some particles are generated at a slightly greater distance from the tally point.

The anticipated relation between decreasing ion beam energy and flux at location D is readily discernable, even when accounting for the statistical error of the Monte Carlo simulation. The 90 kV source causes a larger flux than the 110 kV source, which in turn is larger than that from the 130 kV source.

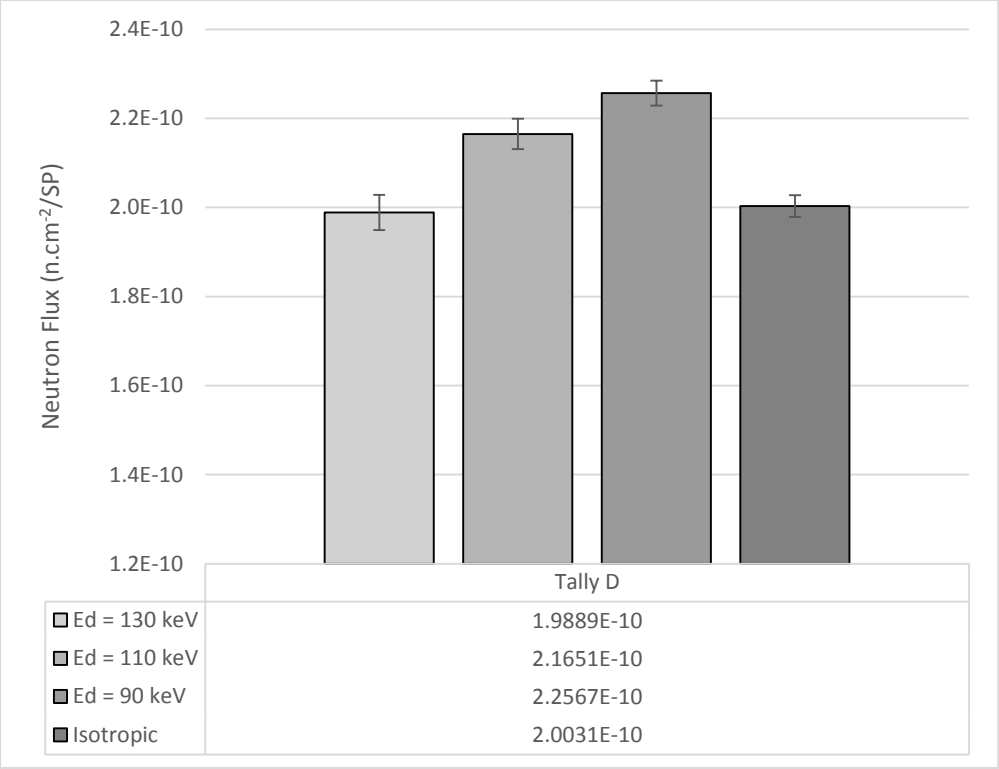

Figure 41: Tally D, Neutron Flux

The flux spectra generated shows that proportionally more neutrons greater than 19.7 keV are incident when simulating the 130 kV source, Figure 42, in contrast to the isotropic source. Although, both have nearly identical energy-integrated values. The largest peak occurs at the highest energy group, between 1.1 MeV and 3.0 MeV, indicating that the most significant portion of the incident flux underwent minimal slow-down processes within the wall material. A large peak between 0.0416 eV and 0.114 eV is still present but is not as critical from a dosimetry perspective, as seen in Figure 44.

The dose rates at location D display the same pattern as the flux. The simulation of the isotropic source resulted in a lower dose rate than the anisotropic sources due to fewer incident neutrons of high energy.

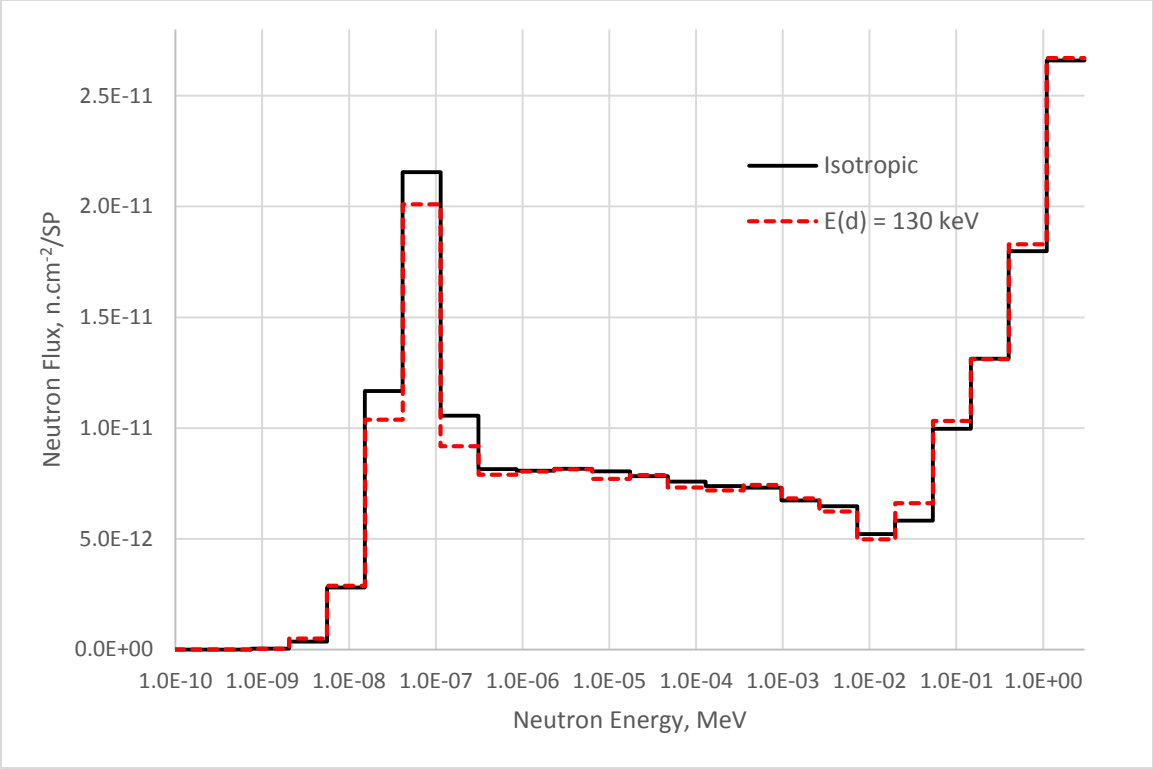

Figure 42: Tally D, Flux Spectra

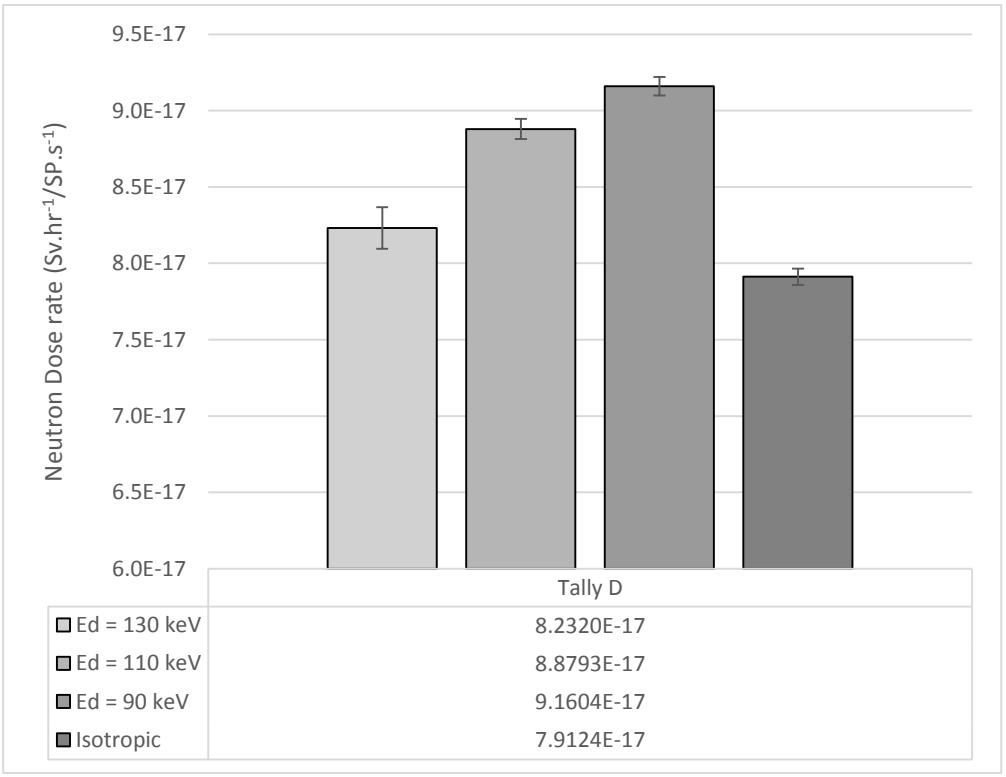

Figure 43: Tally D, ICRP-74 Ambient Neutron Dose Rate

In this location the isotropic source approximation loses validity. Although the actual explanation for the comparatively lower neutron flux is not known for certain it is apparent that such an assumption would result in underestimated dose rates, particularly in the current positioning and orientation of the neutron generator.

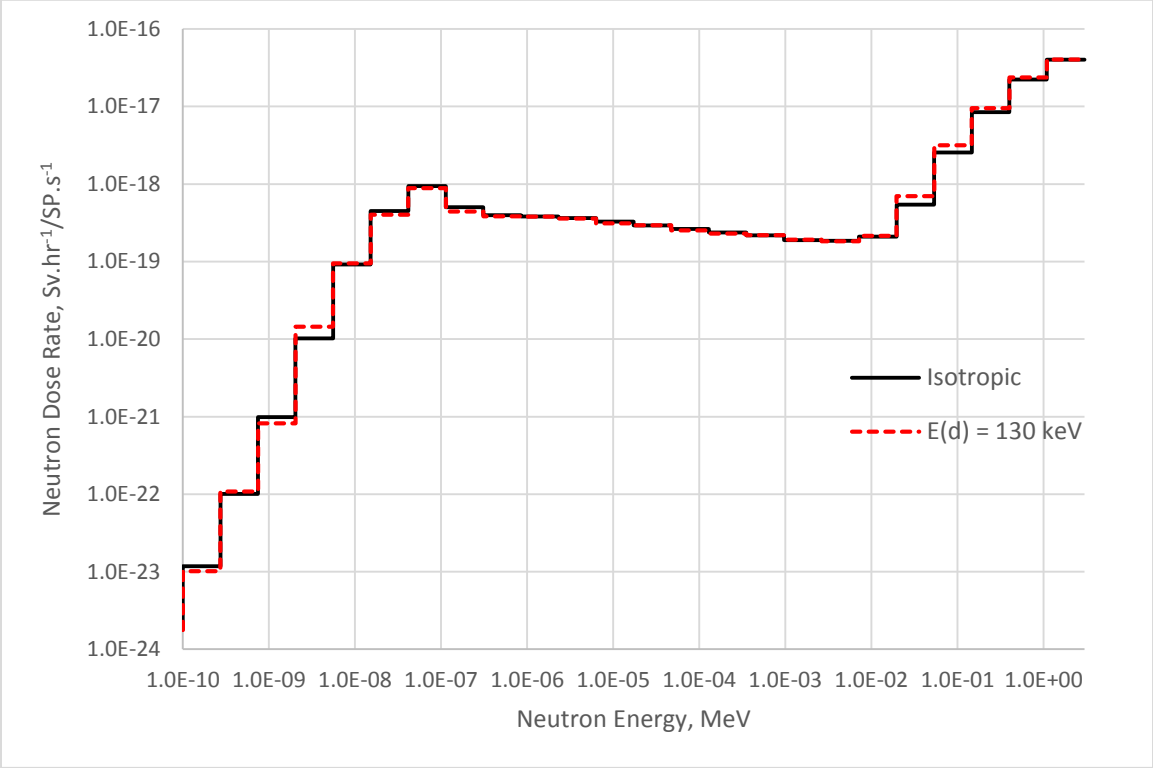

Figure 44: Tally D, Dose Rate Distribution

3.1.5 Simulation Results: Location E

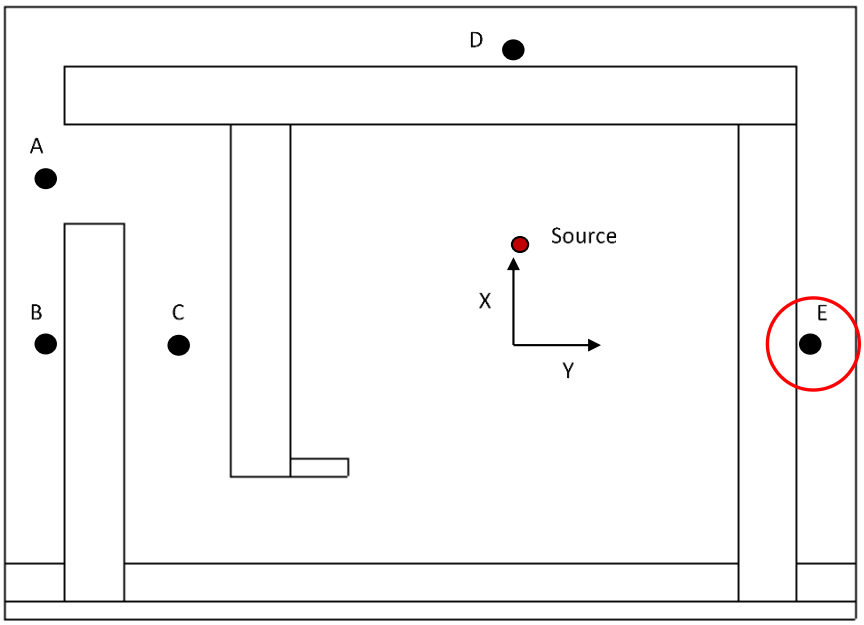

Figure 45: Tally E Location

Location E features the largest difference in flux between the anisotropic sources and the isotropic source, shown in Figure 46. This is to be expected since this location is in the general direction of strongest neutron intensity, the forward emission cone, in terms of both energy and distribution. Unexpectedly, the 90 kV source transmits the greatest neutron flux, followed by the 130 kV source, and finally the 110 kV source. The latter two are however within the same range when accounting for error, thus the flux is not significantly varied when comparing the simulation results of the anisotropic sources. The dose rate data in Figure 48 shows a similar trend when compared to the flux calculations, although the values are close enough to negate meaningful comparison.

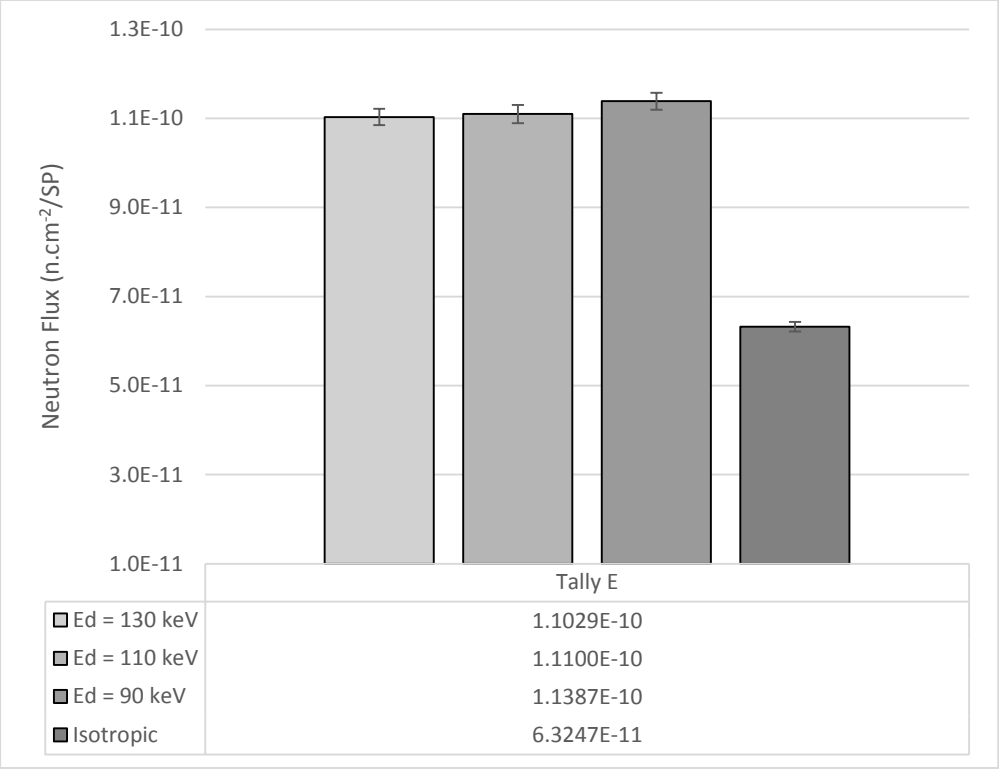

Figure 46: Tally E, Neutron Flux

The incident flux in each energy group is greater for the 130 kV source than the isotropic source, with the exception of neutrons between energies of 0.00557 eV and 0.0152 eV, observable in Figure 47. This is seen likewise with the dose rate distribution in Figure 49. The largest flux contribution is due to the highest energy group, 1.1 MeV to 3.0 MeV, indicating that a large portion of the neutron fluence does not interact significantly with the shielding materials. This was also seen to a lesser extent with the flux simulation results at location D. The large fraction of fast neutrons through the heavy concrete wall adjacent to the source might indicate that there are insufficient inelastic scattering interactions to slow them to intermediate energies. The predominant light nuclide present in the heavy concrete, namely oxygen, is incapable of inelastic scattering at the energy ranges concerned in the current facility. It is capable of scattering neutrons elastically but the angular distribution is peaked forward, resulting in low energy loss per collision. Hydrogen scatters fast neutrons isotropically, but its concentration is dependent on water content in the concrete and is not particularly high.

The majority of the dose rate incurred is by neutrons within the four highest energy groups. A prominent peak between 0.0416 eV and 0.114 eV is still present, which is common to all tally locations examined, but is noticeably lower when simulating an isotropic source.

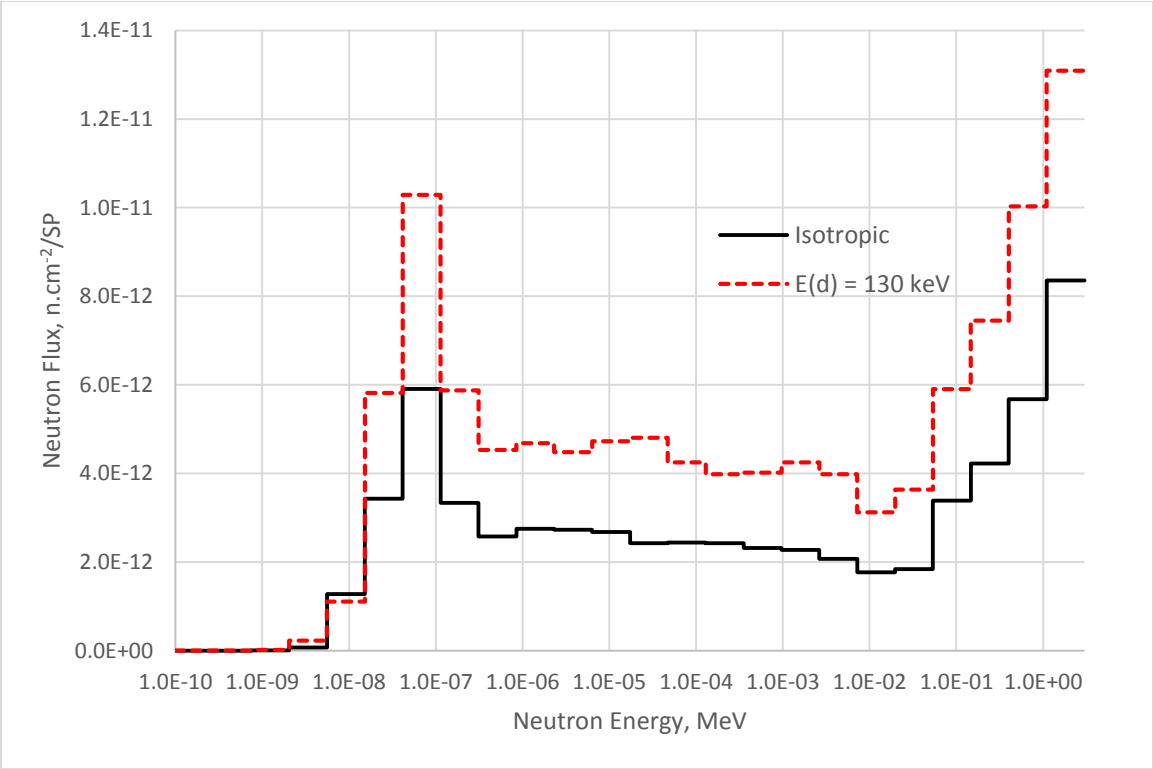

Figure 47: Tally E, Neutron Spectra

This sampled location is the least appropriate to implement an isotropic source approximation in a Monte Carlo simulation. Although the actual dose rate is lower than tally D, the angle of tally E, with respect to the vector defining the solid angle emission cones of the source, would cause it to receive a greater transmitted neutron fluence at an equivalent distance. In all likelihood, the neutron fluence and dose transported through the shielding wall would be greatest at a position in-line with the charged particle trajectory.

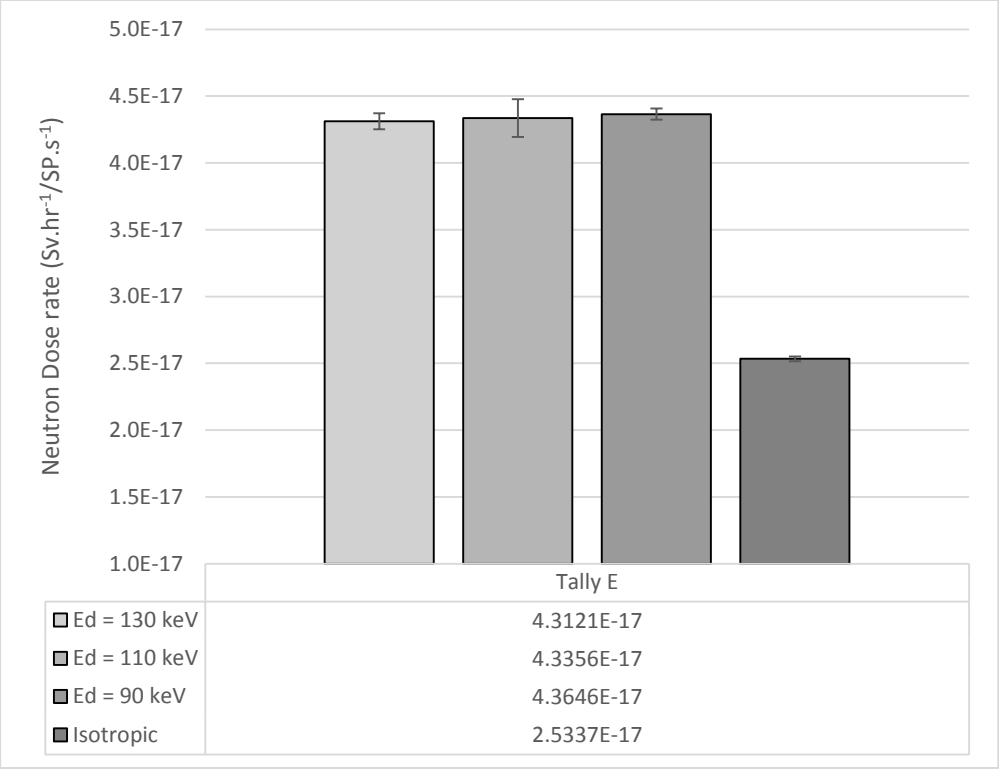

Figure 48: Tally E, ICRP-74 Ambient Neutron Dose Rate

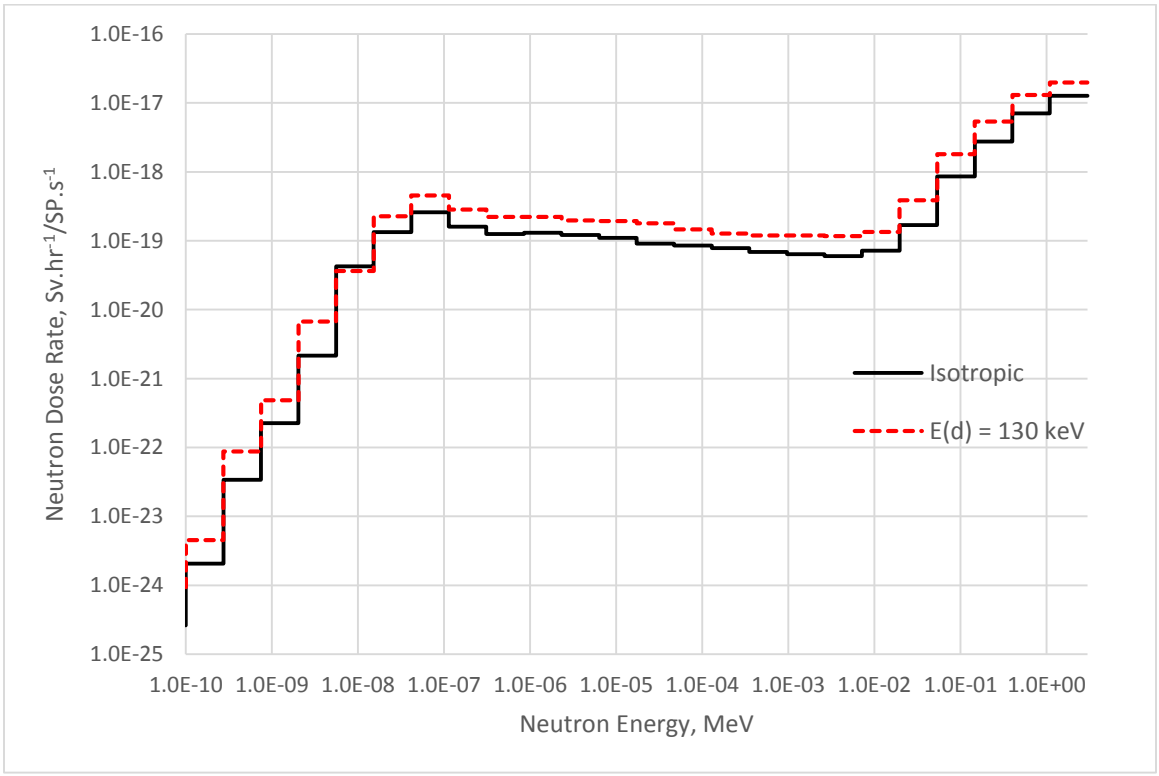

Figure 49: Tally E, Dose Rate Distribution

3.2. Experimental Results

3.2.1 Calculation of Source Intensity

The dose rate measured by the bubble dosimeters placed around the neutron generator, as shown in Figure 19, is summarized in Table 9 together with the calculated statistical errors.

Table 9: Bubble Dosimeter Readings

Bubble Detector	Sensitivity (bubbles/mrem)	No. bubbles	Dose (mrem)	Time (min)	Dose Rate (mrem/hr)
F	12 ± 0.12	280 ± 16.73	23.33 ± 1.41	11	127.25 ± 7.69
G	8 ± 0.08	70 ± 8.37	8.75 ± 1.05	11	47.72 ± 5.72
H	12 ± 0.12	23 ± 4.80	1.92 ± 0.40	11	10.47 ± 2.18

The simulated normalized dose rates, using the embedded NCRP-38 dose function card, is shown in Table 10. The purpose of experimentally determining the dose rates was to first to validate the simulation model and second permit calculation of the neutron intensity from the P-385 generator.

Table 10: Calculated Source Intensity

	Location F	Location G	Location H
Experimental Dose Rate (mrem/hr)	127.25	47.72	10.47
Simulated Dose Rate ($mrem.hr^{-1}/SP.s^{-1}$)	2.08E-05	3.62E-06	1.81E-06
Calculated Source Intensity (n/s)	(6.12E ± 0.37)E+06	(1.32 ± 0.16)E+07	(5.76 ± 1.20)E+06

When the source intensity was calculated using the simulated dose rates, data points F and H gave results that were very close in value. However, location G had a calculated intensity of more than a factor of two greater, which could not be reconciled even when accounting the error range. An intensity of approximately 5.0E+06 neutrons per second was obtained experimentally in one published reference for the P-385 generator in D-D configuration [30]. It was decided that the best course was to assume an average of the intensities calculated at locations F and H.

$$I_{E(d)=130\ keV} \cong 5.94 \times 10^6\ \frac{n}{s}$$

The intensity of the P-385 neutron generator when operating with 130 kV acceleration potential and 70 µA beam current was determined, therefore, to be approximately 5.94E+06 neutrons per second with an RMS error of 1.25E+06. The intensities of the generator when selecting lower voltages were calculated by assuming that the neutron yield is proportional to the H^2(d, n)He^3 integrated cross-section, for particular incident deuteron energies. The calculated source intensities are listed in Table 11.

$$I_{E(d)=i} \cong I_{E(d)=130\ keV} \cdot \frac{\sigma_{E(d)=i}}{\sigma_{E(d)=130\ keV}}$$

Table 11: Estimated Source Intensity

Source Model	(d, n) Cross Section (mb)	Intensity (n/s)
E_d = 130 keV	0.023372	5.938E+06
E_d = 110 keV	0.018785	4.773E+06
E_d = 90 keV	0.01395	3.544E+06

3.2.2 Total Flux and Dose Rates

The total dose rate, in µSv/h, was calculated by multiplying the simulated per-particle dose rates by the intensity. The total flux was completed similarly.

$$\dot{D}_i = \dot{d}_i \cdot I_{E(d)=i}$$

As can be seen in Figure 50 and Figure 51 the total dose rate and flux is greatest at all locations when simulating the 130 kV source. The variations in the per-source-particle values generated by MCNP do not have a significant effect overall. At location D, Figure 43, the 90 kV source had a noticeably greater dose rate per source-particle than the 130 kV source. However, the much greater neutron-producing cross-section associated with 130 keV incident deuterons results in a greater neutron yield and resulting fluence at any location.

Of the locations sampled in the neutron generation facility, tally C has the highest possible dose rate. This is to be predicted since, due to its positioning relative to the source, neutrons are not

required to penetrate any shielding walls to cause a large flux. The dose rate at location A is similar, but is further away and requires particles to undergo a greater number of scattering events in the maze. Tally B is proximate to tally A, but its positioning necessitates that the particles penetrate a wall. This results in the lowest dose rate in any space adjacent to the generator room. The simulation at location D recorded a greater mean value than location E due to the proximity of the generator. The latter location was not directly in the path of the most intense neutron flux and would have been greater had it been displaced in the +X direction.

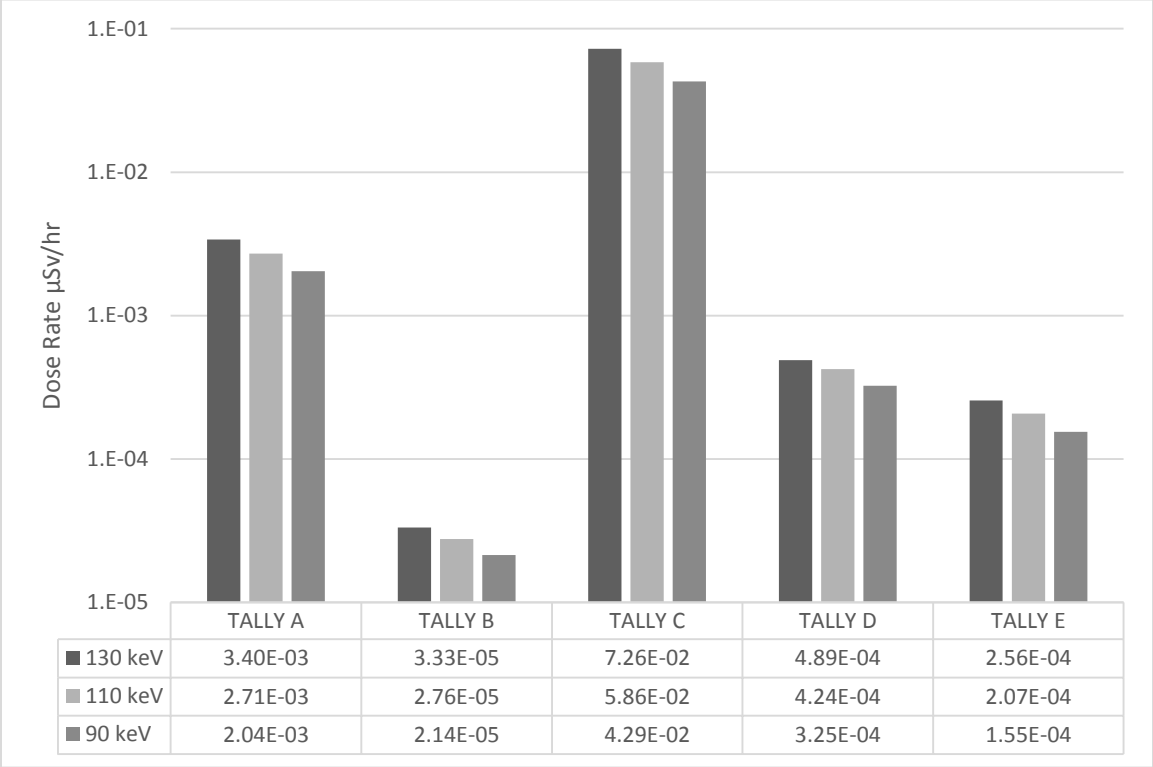

	TALLY A	TALLY B	TALLY C	TALLY D	TALLY E
130 keV	3.40E-03	3.33E-05	7.26E-02	4.89E-04	2.56E-04
110 keV	2.71E-03	2.76E-05	5.86E-02	4.24E-04	2.07E-04
90 keV	2.04E-03	2.14E-05	4.29E-02	3.25E-04	1.55E-04

Figure 50: Total Dose Rates

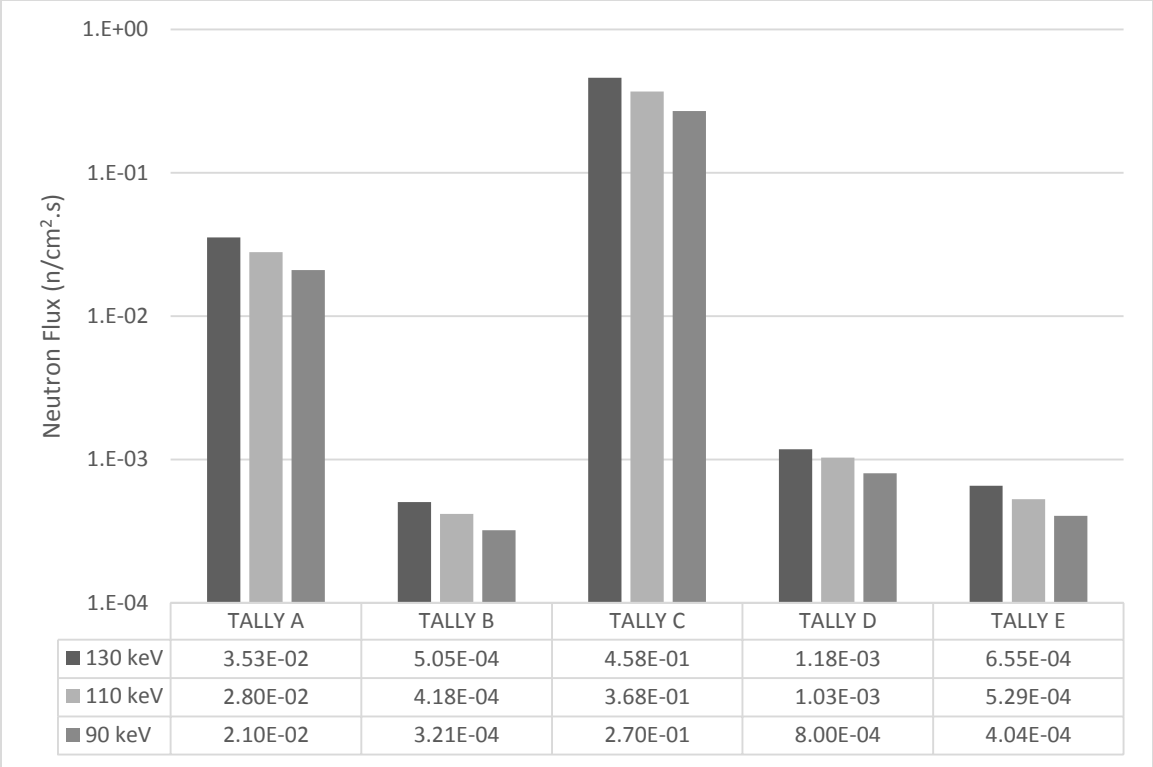

	TALLY A	TALLY B	TALLY C	TALLY D	TALLY E
130 keV	3.53E-02	5.05E-04	4.58E-01	1.18E-03	6.55E-04
110 keV	2.80E-02	4.18E-04	3.68E-01	1.03E-03	5.29E-04
90 keV	2.10E-02	3.21E-04	2.70E-01	8.00E-04	4.04E-04

Figure 51: Total Flux

3.3. Sensitivity Analysis

The neutron spectra at tally locations D and E indicate that a large portion of fast neutrons still manage to penetrate the heavy concrete wall, and contribute largely to the dose. It is prudent to examine the effects of variability in wall thickness from the nominal value of 100 cm that may be present. To this end two series' of Monte Carlo simulations were conducted by modeling a point source emitting 2.5 MeV neutrons isotropically, representing the average neutron emission energy of the generator, surrounded by a sphere of heavy concrete. The thickness of the hollow sphere of concrete was incrementally changed from 95 cm to 105 cm with its central radius constant from the source: 379 cm. The dose rates were calculated at a fixed distance of 529 cm, as seen in Figure 52.

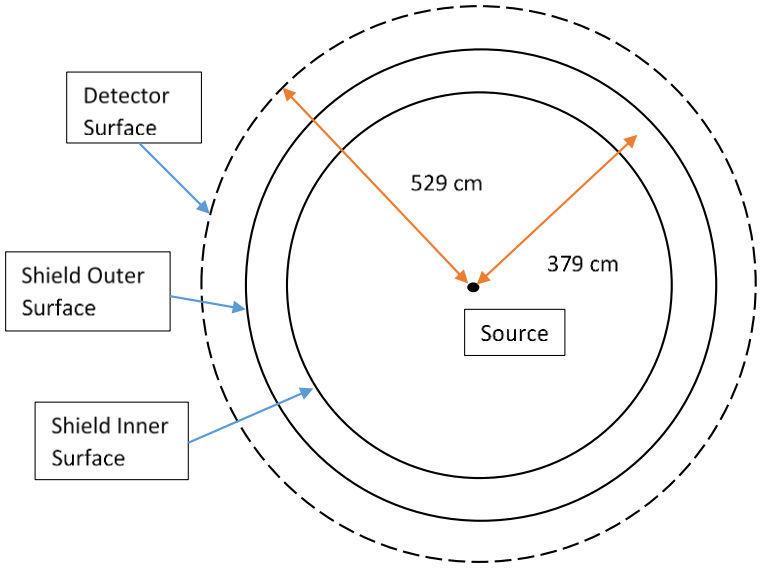

Figure 52: Geometry in Sensitivity Analysis

The dose rate results of this sensitivity analysis are shown in Figure 53, including errors, and are normalized to the value calculated at 100 cm. This was also compared to a simplified analysis using the calculated removal cross-section of the concrete.

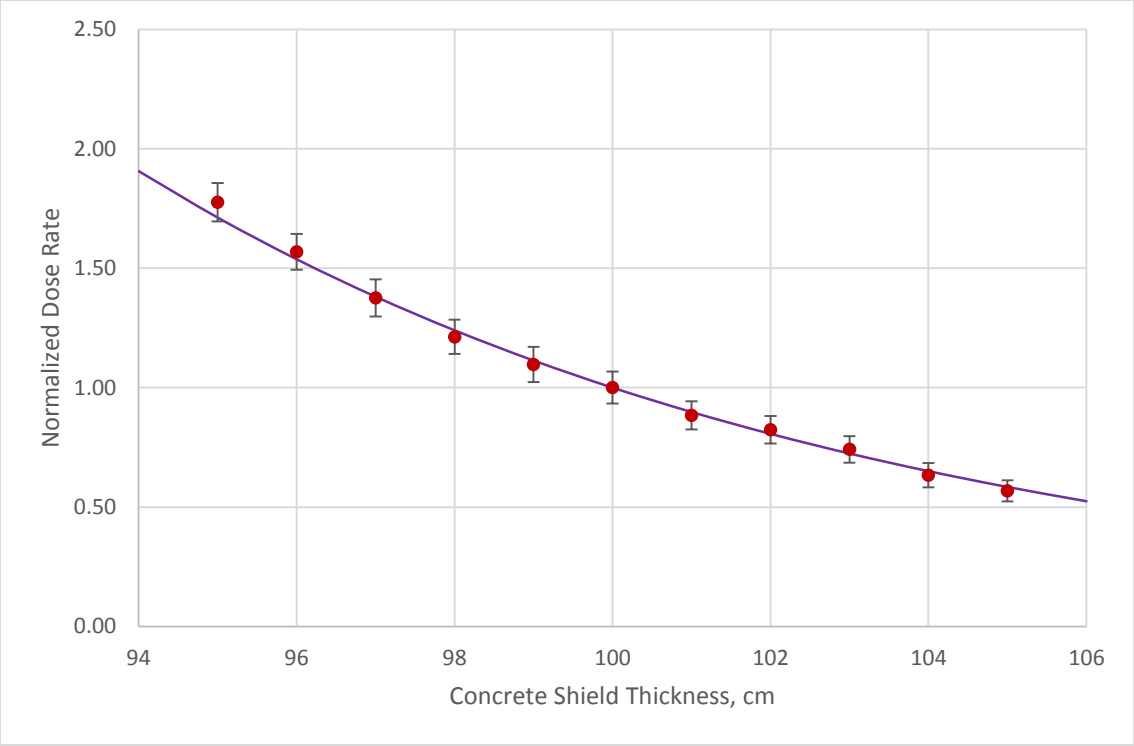

Figure 53: Shield Thickness Sensitivity Analysis

It is observable that the simulated results are nearly identical to the removal approximation. It was not anticipated whether this would be the case as it was unknown if the concentration of Hydrogen in the concrete was sufficient to utilize the neutron removal method. As the actual variation in wall thickness is not known, this data is only included for future reference should more accurate measurements of the facility be undertaken. The effect of shielding thickness on the previously presented tally results is of greater concern if the wall is particularly thin relative to the nominal value; due to the exponential nature of neutron removal. Since these calculations assume a neutron flux directionally normal to the shielding, locations that are not parallel or perpendicular to the generator target must also take into account the effective wall thickness at different angles.

Conclusion

The work to produce this thesis involved simulating neutron transport to calculate the fluence and dose rates at locations proximate to the room holding the facilities' P-385 D-D neutron generator. Four models of the generator were produced: one was an isotropically emitting disc to establish a benchmark; three were point sources creating particles with angular and energy distributions corresponding to three different deuteron projectile energies.

The results of the Monte Carlo simulations, which presents data normalized to the number of source particles, showed only minor variation within the modelled accelerator sources. When compared to the isotropic source approximation, the accelerator sources generally transmitted a lower neutron fluence to locations in directions describable as within the rearward emission cone of the source vector. If the tally location was within the forward emission cone the fluence and dose rate were noticeably lower when simulating an isotropic source. Although the P-385 is not capable of emissions that would exceed dose rate limitations in adjacent spaces, this problem may arise if a more intense generator is operated that uses deuterium-deuterium fusion reactions.

The total dose rate estimates calculated using the neutron creation cross sections, scaled to the experimentally derived neutron generator intensity, showed that they are proportional primarily to the acceleration potential applied. The minor variation in dose rates at the locations sampled, on a per-source-particle basis, was insufficient to alter this consistent trend.

Further work to improve accuracy would involve modeling the source using thick target neutron yields and distributions and accounting for the scattering effects caused by the generator components.

References

[1] H. Goldstein, Fundamental Aspects of Reactor Shielding, New York, New York: Addison-Wesley, 1959.

[2] J. Shultis and R. Faw, Radiation Shielding, La Grange Park: American Nuclear Society, 2000.

[3] N. Schaeffer, Ed., Reactor Shielding for Nuclear Engineers, Springfield, Virginia: U.S. Atomic Energy Commission Office of Informational Services, 1973.

[4] E. Amaldi, "The Production and Slowing Down of Neutrons," in *Neutrons and Related Gamma Ray Problems*, S. Flugge, Ed., Berlin, Springer-Verlag, 1959.

[5] J. Duderstadt, Nuclear Reactor Analysis, New York: Wiley, 1976.

[6] K. Wirtz and K. Beckhurts, Neutron Physics, Berlin: Springer-Verlag, 1964.

[7] J. R. Lamarsh, Nuclear Reactor Theory, Reading: Addison-Wesley, 1966.

[8] J. Cremer, Advances in Imaging and Electron Physics, Amsterdam: Elsevier, 2012.

[9] A. Foderaro, The Elements of Neutron Interaction Theory, Cambridge: Massachusetts Institute of Technology, 1971.

[10] E. P. Blizard, Ed., Reactor Handbook, vol. III b, New York, New York: John Wiley & Sons, 1962.

[11] IAEA, "Neutron Generators for Analytical Purposes," International Atomic Energy Agency, Vienna, 2012.

[12] W. Burcham, "Nuclear Reactions, Levels, and Spectra of Light Nuclei," in *Nuclear Reactions I*, S. Flugge, Ed., Berlin, Springer-Verlag, 1957.

[13] R. Blin-Stoyle and M. Grace, "Oriented Nuclei," in *Nuclear Reactions III*, S. Flugge, Ed., Berlin, Springer-Verlag, 1957.

[14] S. S. Nargolwalla and E. P. Przyblowicz, Activation Analysis with Neutron Generators, New York, New York: John Wiley & Sons, 1973.

[15] V. Valkovic, 14 MeV Neutrons: Physics and Applications, Boca Raton: CRC Press, 2106.

[16] D. Tilley, H. Weller and G. Hale, "Energy Levels of Light Nuclei A = 4*," *Nuclear Physics,* vol. 541, pp. 1-104, 1991.

[17] D. Tilley, C. Cheves, J. Godwin, G. Hale, H. Hofman, J. Kelley, C. Sheu and H. Weller, "Energy Levels of Light Nuclei A = 5, 6, 7," *Nuclear Physics,* vol. 708, pp. 3-163, 2002.

[18] NNDC, "Nudat 2.6," [Online]. Available: http://www.nndc.bnl.gov/nudat2/. [Accessed June 2016].

[19] C. A. Uttley, "Sources of Monoenergetic Neutrons," in *Neutron Sources: For Basic Physics and Applications*, S. Cierjacks, Ed., Oxford, Pergamon Press, 1983.

[20] P. Assimakopoulos, "Kinematics of Three-Body Reactions," *Computer Physics Communications,* vol. 35, pp. 385-400, 1975.

[21] H. Ing, R. Noulty and T. McLean, "Bubble Detectors - A Maturing Technology," *Radiation Measurements,* vol. 27, pp. 1-11, 1997.

[22] F. D'Errico, "Radiation Dosimetry and Spectrometry with Superheated Emulsions," *Nuclear Instruments and Methods in Physics,* vol. 184, pp. 229-254, 29 May 2001.

[23] C. Leroy and P. Rancoita, Principles of Radiation Interaction in Matter and Detection, Singapore: World Scientific, 2016.

[24] R. Sarkar, B. Chatterjee, B. Roy and S. Roy, "Radiation Detection by Using Superheated Droplets," *Radiatoin Physics and Chemistry,* vol. 75, pp. 2186-2194, 2006.

[25] Argonne National Laboratory, *A Summary of Shielding Constants for Concrete,* Argonne, Illinois, 1961.

[26] X-5 Monte Carlo Team, *MCNP - A General Monte Carlo N-Particle Transport Code, Version 5,* Los Alamos: Los Alamos National Security, 2008.

[27] Thermo Scientific, *P 385 Neutron Generator Operation Manual,* Thermo Fisher Scientific, 2010.

[28] G. Knoll, Radiation Detection and Measurement, New York: John Wiley & Sons, 2010.

[29] Bubble Technology Industries, *Bubble Detectors, Neutron Dosimeters,* Chalk River, Ontario: BTI, 2009.

[30] C. Wharton, E. Seabury, D. Chichester, A. Caffrey, J. Simpson and M. Lemchak, "X-ray Measurements of a Thermo Scientific P385 DD Neutron Generator," U.S. Department of Energy, Idaho, 2010.

APPENDICES

Tally Statistics

Table 12: 130 keV flux tally statistics

Tally	Mean Value	Error	V.o.V.	PDF Slope	Checks Passed
A	5.9486E-09	0.0124	0.0027	6.3	10
B	8.5085E-11	0.0305	0.0896	1.8	8
C	7.7184E-08	0.0099	0.0157	3.3	10
E	1.9889E-10	0.0199	0.0430	3.1	10
F	1.1029E-10	0.0166	0.0383	3.4	10

Table 13: 110 keV flux tally statistics

Tally	Mean Value	Error	V.o.V.	PDF Slope	Checks Passed
A	5.8644E-09	0.0124	0.0015	10.0	10
B	8.7526E-11	0.0343	0.1301	2.4	8
C	7.7047E-08	0.0059	0.0019	4.9	10
E	2.1651E-10	0.0158	0.0527	3.5	10
F	1.1100E-10	0.0185	0.0454	3.6	10

Table 14: 90 keV flux tally statistics

Tally	Mean Value	Error	V.o.V.	PDF Slope	Checks Passed
A	5.9145E-09	0.0130	0.0017	10.0	10
B	9.0449E-11	0.0535	0.1456	1.8	8
C	7.6089E-08	0.0043	0.0021	3.7	10
E	2.2567E-10	0.0123	0.0518	3.3	10
F	1.1387E-10	0.0167	0.0432	3.7	10

Table 15: Isotropic flux tally statistics

Tally	Mean Value	Error	V.o.V.	PDF Slope	Checks Passed
A	6.3195E-09	0.0071	0.0009	6.5	10
B	8.8063E-11	0.0391	0.0985	2.2	9
C	8.2765E-08	0.0078	0.0110	3	10
E	2.0031E-10	0.0123	0.0772	3.7	10
F	6.3247E-11	0.0170	0.0542	2.4	9

Table 16: 130 keV dose rate tally statistics

Tally	Mean Value	Error	V.o.V.	PDF Slope	Checks Passed
A	5.7216E-16	0.0222	0.0094	5.3	10
B	5.6121E-18	0.0226	0.0621	2.3	8
C	1.2226E-14	0.0063	0.0015	4.5	10
E	8.2320E-17	0.0166	0.0126	3.3	10
F	4.3121E-17	0.0138	0.0656	2.4	9

Table 17: 110 keV dose rate tally statistics

Tally	Mean Value	Error	V.o.V.	PDF Slope	Checks Passed
A	5.6775E-16	0.0226	0.0126	5.1	10
B	5.7876E-18	0.0362	0.1122	2.9	8
C	1.2275E-14	0.0065	0.0012	6.4	10
E	8.8793E-17	0.0074	0.0806	1.8	9
F	4.3356E-17	0.0326	0.0992	2.6	9

Table 18: 90 keV dose rate tally statistics

Tally	Mean Value	Error	V.o.V.	PDF Slope	Checks Passed
A	5.7523E-16	0.0246	0.0175	5.2	10
B	6.0419E-18	0.0465	0.1920	2.0	8
C	1.2110E-14	0.0067	0.0010	8.9	10
E	9.1604E-17	0.0066	0.0555	2.3	9
F	4.3646E-17	0.0096	0.0829	1.9	9

Table 19: isotropic dose rate tally statistics

Tally	Mean Value	Error	V.o.V.	PDF Slope	Checks Passed
A	6.5673E-16	0.0088	0.0029	8.3	10
B	6.0702E-18	0.0300	0.1016	2.9	8
C	1.3800E-14	0.0028	0.0002	7.3	10
E	7.9124E-17	0.0067	0.0588	2.1	9
F	2.5337E-17	0.0070	0.0554	2.2	9